HIGH-STRENGTH LOW-ALLOY (HSLA) STEELS FOR BATCH ANNEALING

THE DEVELOPMENT OF HIGH-STRENGTH LOW-ALLOY (HSLA) STEELS FOR BATCH ANNEALING PROCESSES

By JARED LEVY, B.Eng.

A Thesis Submitted to the School of Graduate Studies in Partial Fulfilment of the Requirements for the Degree of Master of Applied Science

McMaster University

McMaster University MASTER OF APPLIED SCIENCE (2023) Hamilton, Ontario
(Engineering)

TITLE: The Development of High-Strength Low-Alloy (HSLA) Steels for Batch Annealing Processes

AUTHOR: Jared Levy, B.Eng. (McMaster University)

SUPERVISORS: Dr. Hatem Zurob & Dr. Joseph McDermid

NUMBER OF PAGES: xvii, 122

ABSTRACT

Stronger and higher strength steels are continuously being demanded by industry. A stronger steel enables less material to be used to meet structural requirements, allowing for both cost and weight savings. Through collaboration with Stelco, CanmetMATERIALS, and McMaster University, this project focused on the development of a Grade 80 (550MPa YS and 600MPa UTS) steel with elongation at fracture of 16%. The design space for the creation of the steel was limited to high-strength low-alloy and low-carbon steels that are compatible with batch-annealing processes.

To achieve this goal, two main strengthening methods were explored. The first method employed the use of precipitation hardening through microalloying additions of Mo, Nb, Ti, and V to form various metal carbide precipitates. The second method was based upon dislocation strengthening using recovery annealing and Ti to delay recrystallization.

Multi-scale characterization was used to quantify the strengthening mechanisms and to explain how the microstructural changes, features, and evolution affected the properties of the steel. Uniaxial tensile testing was performed to determine key mechanical properties, namely the yield strength, tensile strength, and elongation at fracture. Optical microscopy, scanning electron microscopy, energy-dispersive x-ray spectroscopy, electron backscatter diffraction, transmission electron microscopy, and atom probe tomography were utilized extensively for microstructural analysis to further quantify the steels.

The precipitation hardened steel reached a yield strength of 605MPa with 15.4% elongation at fracture for a 50mm gauge length. This was achieved using a cold rolling reduction of 66% followed by a heat treatment at 670°C for 24 hours.

The recovery-annealed steel obtained even better properties. It achieved a yield strength of 610MPa with a 19.6% elongation at fracture for a 25.4mm gauge length. A cold rolling reduction of 60% was used followed by a heat treatment at 550°C for 36 hours.

The strengthening mechanism for this steel is novel, and involves the slowing of recrystallization without Zener pinning nor solute decoration of dislocations. This thesis will hopefully bring upon new research into this mechanism. Furthermore, the properties of this recovery-annealed steel shows great promise for use in industry due to its high strength, good elongation, and low materials cost. Consequently, this steel could be the subject of substantial research in the near future.

PREFACE

The development of a high-strength low-alloy steel compatible with batch-annealing processes is motivated principally by economic factors. HSLA steel, by its very nature, has relatively small alloying additions which help to keep costs down. Furthermore, its high strength enables less steel to be used overall, also reducing price. The other key aspect is that the steel be compatible with batch annealing as the industry partner has underutilized batch annealing furnaces in their factory that they want to use. Batch-annealing involves heat treatment of cold-rolled steel coils in a protective atmosphere and the process requires lengthy heating and cooling times.

The requirement of being compatible with batch-annealing created the largest obstacle in the development of the steel. Due to the fact the coils of steel are of a substantial size, their temperature cannot quickly be changed as the heat transfer through a bulk material is too slow. Therefore, many of the traditional ways of strengthening steel become unfeasible. For example, it is not possible to utilize accelerated cooling to create martensitic or bainitic structures.

As a result of this limitation, this steel will have a ferritic microstructure. Creating a high strength steel would therefore focus on strengthening the ferritic matrix. Under these constraints, two main strategies were employed. The first technique, which is the focus of Section 1, is to use precipitation strengthening to achieve the desired mechanical properties. By using small amounts of alloying additions and annealing temperatures below Ac1, the precipitates can be made quite fine and numerous, allowing for sufficient strengthening. The second technique, highlighted in Section 2, is to use recovery annealing to make use of dislocation strengthening through additions of titanium to slow recrystallization and maintain a recovered microstructure after heat treatment.

This work was done under the supervision of Dr. Hatem Zurob and Dr. Joseph McDermid. There was also substantial collaboration with Dr. Colin Scott and Dr. Christopher DiGiovanni from CanmetMATERIALS and Dr. Tom Zhou from Stelco. Casting, hot rolling and coiling of the steels, as well as mechanical testing of the precipitation hardened steel were carried out at CanmetMATERIALS; the remainder and majority of the work was performed at McMaster University.

ACKNOWLEDGEMENTS

First and foremost, I have to thank my primary supervisor Dr. Hatem Zurob for his continued and unwavering support. He was the single most important factor in the successful completion of my degree, and his contributions – academic, personal, and professional – cannot be understated. In fact, he is the reason I pursued a master's degree in the first place. He always answered my questions, listened to my challenges, proposed new ideas, and was always caring and understanding during my time here at McMaster. I could not have completed my degree without him, and I will forever remember the positive impact he made in my academic career, my professional career, and in my life.

To Dr. Zurob, I extend to you my sincerest gratitude. Thank you very much for everything.

Secondly, I need to acknowledge my co-supervisor, Dr. Joseph McDermid. His collaboration and input were also key in guiding me through my master's. Furthermore, his extensive knowledge of steel and the feedback he provided were extremely valuable to my research.

I also need to thank Colin Scott and Christopher DiGiovanni from CanmetMATERIALS and Tom Zhou from Stelco for their collaboration in this thesis. They let me test some of their steels, provided crucial input on steel chemistries, and even casted and hot rolled my steel. Their contributions undoubtedly streamlined my research, and the professional collaboration was greatly appreciated.

Additionally, I have to thank the support of the amazing technical and specialized staff at McMaster. Firstly, I thank the lab technicians Doug Culley, Xiaogang Li, and Ed

McCaffery. They helped me innumerable times in completing my laboratory work and always helped out with a smile. Likewise, I thank Jim Cleaver for his help with machining and cutting out all the tensile bars and other various pieces from my sheets of steel. As well, I need to thank the extensive amount of time the microscopists Jhoynner Martinez, Chris Butcher, Carmen Andrei, and Gabriel Arcuri in the Canadian Centre for Electron Microscopy spent for their help with sample preparation, SEM, EDS, EBSD, TEM, and APT microscopy.

I also express my appreciation to the entire department of Materials Science and Engineering at McMaster. The professors taught me all I know about materials science, and made the past five and a half years – both undergraduate and postgraduate – very productive and meaningful. Similarly, I want to acknowledge my fellow students for the help, friendship, and moral support they have provided during my university career.

Lastly, but certainly not least, I have to thank my family for their support and motivation they gave me during my master's. Thank you to my grandparents Sharon Levy-Cohen and Lawrence Cohen for welcoming me into your home and giving me a place to stay when needed in Hamilton. And of course, thank you to my parents Brian Levy and Rachel Levy for supporting me both financially and personally during my time at McMaster. To my whole family, I love you all.

TABLE OF CONTENTS

LIST OF FIGURES

LIST OF TABLES

ABBREVIATIONS AND SYMBOLS

Abbreviations

APT – Atom Probe Tomography/Tomograph
BCC – Body Centred Cubic
BF – Bright Field
CNC – Computer Numerical Control
EBSD – Electron Backscatter Diffraction
EDS – Energy Dispersive X-ray Spectroscopy
EELS – Electron Energy Loss Spectroscopy
FCC – Face Centred Cubic
FIB – Focused Ion Beam
HAADF – High Angle Annular Dark Field Imaging
HSLA – High-Strength Low-Alloy
IPF – Inverse Pole Figure
KAM – Kernal Average Misorientation
SEM – Scanning Electron Microscopy/Microscope
STEM – Scanning Transmission Electron Microscopy/Microscope
TEM – Transmission Electron Microscopy/Microscope
TTT – Time-Temperature-Transformation
UTS – Ultimate Tensile Strength
YS – Yield Strength
%El. – Percent Elongation at Fracture

Symbols

All symbols and constants labelled in the thesis as they appear; the most important symbols included are here for easy reference.

ε – Strain
σ – Stress
τ – Shear Stress
E – Elastic (Young's) Modulus
G – Bulk Modulus
k_y – Hall-Petch Constant

Section 1 – Literature Review

1.0 – Properties, Applications, and Economics of HSLA Steel

High-Strength Low-Alloy (HSLA) steels, interchangeably called microalloyed steels, are a class of steels with low amounts of carbon, moderate amounts of Si and Mn, and small additions of other transition metals – typically Ti, V, Mo, and Nb [1]. The inclusion of these alloying additions is what distinguishes microalloyed steels from traditional low-carbon steels. These microalloying additions contribute to the strength of the steel to a greater degree than what their small concentration would suggest [2]. The mechanisms of strengthening will be discussed in depth in section 1.1.

HSLA steels are attractive for their relatively high strength to price ratio as they have fairly high yield strengths while still being economical to produce due to the low amounts of costly alloying additions. HSLA steels are extensively used in automotive applications as stronger steels allow for less material to be used, which equates to weight savings. These weight savings translate into increased fuel economy, and thus these steels are and have been of interest to automobile manufacturers for decades [3]. Other applications include uses in the trucking and railroad industries as well as oil and gas pipelines [4].

Due to their usefulness, microalloyed steels are becoming more and more prominent, with increasing year-over-year production. Projected compound annual growth out until 2029 is forecasted at 5.6% [5]. This is in line with the continued demands for more fuel-efficient vehicles and the rise in electric vehicles. The market share of steel produced that is HSLA steel is between 10% and 12% [6], [7]. Consequently, microalloyed steels are very important and are therefore the subject of substantial research and development.

1.1 – Strengthening Mechanisms of HSLA Steel

Metals deform through the repeated movement of dislocations through the metal lattice due to an applied shear stress [8]. Slowing or stopping the movement of these dislocations is the key objective in strengthening of metallic materials as a material's strength is determined by how well it impedes dislocation motion. There are five primary strengthening mechanisms for microalloyed steels: intrinsic strength (σ_0), solid solution strengthening (σ_{SS}), precipitation strengthening (σ_{ppt}), grain boundary strengthening (σ_{GB}), and dislocation strengthening / work hardening (σ_{dis}) [2].

1.1.1 – Intrinsic Strength

All metals have an intrinsic strength due to the amount of energy required overcome friction within the lattice and move a dislocation. This shear stress is called the Peierls or Peierls-Nabarro Stress [9]. It is a function of the crystal structure, slip distance, and slip direction [9]. In HSLA steel operating at ambient temperatures, iron is in the form α-Fe which has a body-centred cubic (BCC) structure. The BCC crystal lattice has 48 slip systems, though many are not active at room temperatures in iron due to high Peierls stress. The dominate slip system in ferrite steels is the $\{110\}\langle 111\rangle$ system [10]. The Peierls stress is given as

$$\tau_{PN} = G\exp\left[\frac{-2\pi w}{b}\right] \quad (1.1)$$

with τ_{PN} being the Peierls-Nabarro Stress, G being shear modulus, b the slip distance, and w the slip width [9].

From this equation, it is shown that τ_{PN} is proportional to slip width and inversely to proportional to slip distance. Consequently, a materials intrinsic strength increases at colder temperatures due to the decreasing dislocation width [9]. However, at ambient temperatures, the values for intrinsic strength are quite small. Indeed, ultra-high purity iron has been experimentally shown to have a yield strength of only around 50MPa [11].

1.1.2 – Precipitation Strengthening

Precipitate strengthening is one of the most common ways of strengthening metals, with particular presence in aluminum alloys and microalloyed steels [12]. It is predicated upon the fact that precipitates impede dislocation motion as dislocations must either move through or move around the precipitates [12]. A higher number density of precipitates, achieved through increased volume fraction and reduced size of precipitates, leads to a smaller mean free path for the dislocations, thus increasing the strength of the metal. The strength and geometric arrangement of the precipitates also impacts the magnitude of precipitation strengthening [9].

1.1.2.1 – Non-Shearable Precipitates

In the first case of dislocation-precipitate interaction, the precipitate is sufficiently strong such that the dislocation moves around it; the precipitate is non-shearable. This method encompasses Orowan looping and cross-slip [13]. Orowan looping is the primary method of bypassing a precipitate as cross-slip only applies to screw dislocations [14]. The precipitate particles can also act as Frank-Reid sources leading to an increase in the dislocation density. The increase in dislocation (line) energy during Orowan looping requires a larger applied stress [9]. This increase in dislocation length is shown in the Figure 1.1.2.1.A.

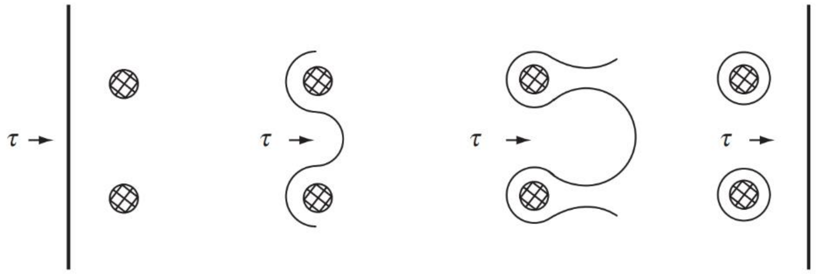

Figure 1.1.2.1.A: Schematic of Orowan Looping [9]

In an idealized model, with the dislocation perpendicular to a regularly ordered array of precipitates, the strengthening can be expressed as

$$\tau = \frac{Gb}{2r} = \frac{Gb}{L} \ (1.2)$$

with τ being the shear stress required to move the dislocation around the precipitates, G being the shear modulus of the matrix, b the burgers vector, r the radius of curvature of looping, and L the distance between precipitates [9].

This model overestimates the contribution of strengthening due to the fact it assumes the dislocation moves perpendicularly to the precipitates. Using a random array of precipitates, one arrives at the Ashby-Orowan model [12]:

$$\tau = 0.84\frac{1.2Gb}{2\pi L}\ln\left(\frac{x}{2b}\right) \ (1.3)$$

with x being the precipitate size relative to the plane in which the dislocation moves. This equation is then converted into one that accounts for the increase in yield strength [12]:

$$\sigma_{ppt} = 0.538\frac{Gb\sqrt{f}}{X}\ln\left(\frac{X}{2b}\right) \ (1.4)$$

with X being the true particle size and f the volume fraction. In microalloyed steels, this can be further refined to [15], [16]:

$$\sigma_{ppt} = 6982\frac{\sqrt{f}}{X}\ln(2\mathrm{X}) \equiv \sigma_{ppt} = 8.9\frac{\sqrt{f}}{X}\ln(1630X) \ (1.5\mathrm{a}, 1.5\mathrm{b})$$

with σ_{ppt} in MPa, which is now only a function of two variables – volume fraction and precipitate size given in nm. This equation shows how smaller particles result in stronger materials as they have a higher number density of precipitates, keeping volume fraction constant. Plotting these two variables shows the estimated strengthening of the material. Figure 1.1.2.1.B is a graph showing the increase in strength [12]. Note how the Orowan model overestimates the contribution of precipitate strengthening by about an order of magnitude.

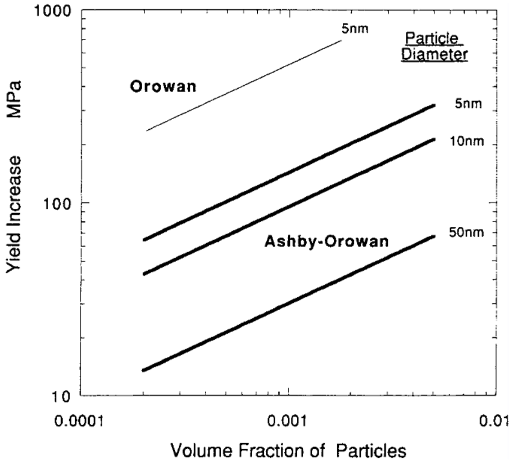

Figure 1.1.2.1.B: Orowan and Ashby-Orowan Strengthening [12]

The Ashby-Orowan model is experimentally shown to be much more accurate, aligning closely with experimental data as shown by the correlation in this data [16]:

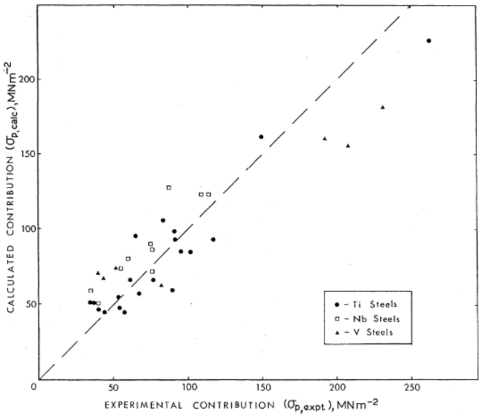

Figure 1.1.2.1.C: Experimental Confirmation of Ashby-Orowan Model [16]

1.1.2.2 – Shearable Precipitates

The second mechanism of dislocation-precipitate interaction involves the dislocation moving directly through the precipitate. If the precipitates are sufficiently weak, the dislocation will shear the precipitate in a process known as particle cutting [17]. This process is illustrated in Figure 1.1.2.2.A [12].

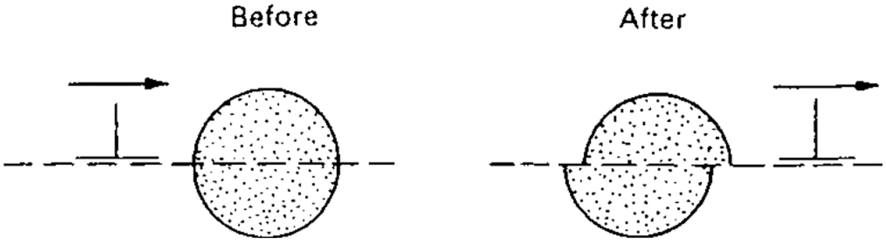

Figure 1.1.2.2.A: Shearing of a Precipitate [12]

In this case, extra energy is required due to the increase in the surface energy [18]. The shear stress required to shear the particle is thus given as [18]:

$$\tau = \frac{\pi r \gamma}{bL} \quad (1.6)$$

with r being the radius of the precipitate, γ the free surface energy, b the burgers vector and L the particle spacing [18]. From this equation, one can see that larger particles better resist shearing. This is opposite to how small particles better resist dislocation movement if they are non-shearable. As such, for each matrix and precipitate material, there is a size below which the particles will shear and above which they will not shear. This limits the maximum amount of strengthening possible by precipitates as making continuously smaller precipitates will simply cause them to shear. In Figure 1.1.2.2.B, the contribution to strengthening from precipitation is given as the red line, with the highest contribution at 9nm [12]. Stronger precipitates will have maximum contributions at smaller sizes, but their contribution is still not asymptotic at very small values due to the fact that they will shear.

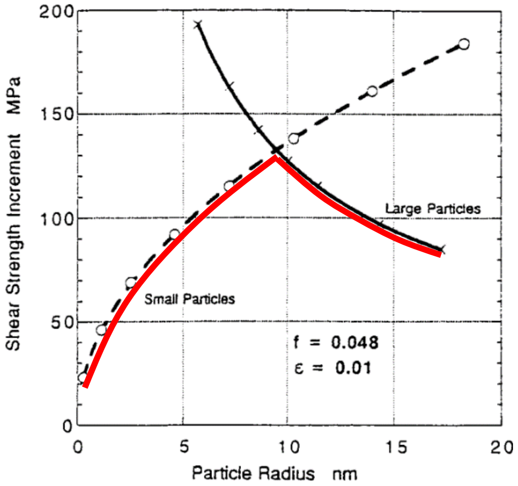

Figure 1.1.2.2.B: Contribution of Strengthening by Precipitate Size for an Idealized Metal [12]

1.1.2.3 – Precipitation Strengthening in Microalloyed Steel

In microalloyed steel, precipitation strengthening is extensively used. The most common precipitates that are employed are transition metal carbonitrides, specifically Ti, V, Nb, and Mo carbonitrides [9]. They are referred to as carbonitrides because the nonmetal component can either be carbon or nitrogen interchangeably. This forms precipitates of the form MX, where M is one of the metals specified above, and X is carbon or nitrogen. These precipitates have the same NaCl structure and frequently dissolve into each other [19]. Some notable examples are (Nb,Mo)(C,N) and (Nb,V,Ti)(C,N) [9], [20].

The different carbonitrides precipitate at different temperatures due to their differing solubility. Solutionizing is typically done in the austenite temperature range so that all the precipitates can be dissolved into solution and then form small precipitates during cooling. At lower temperatures, the precipitates that form are often smaller, so this could influence the choice of which alloying element is used.

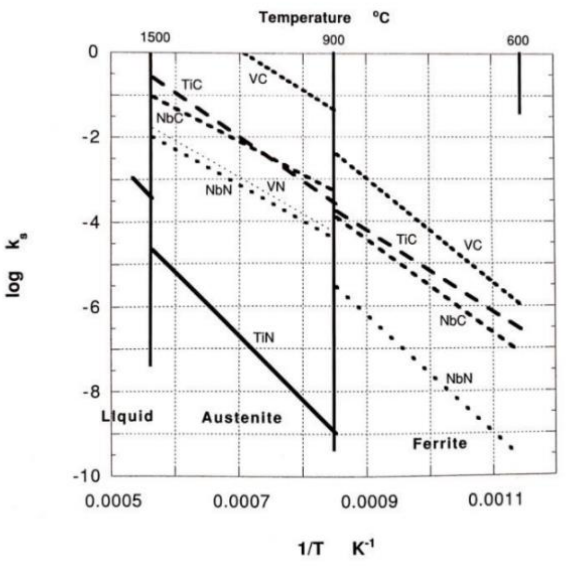

Figure 1.1.2.3.A: Stability of Various Precipitates in Steel [2]

The lower on Figure 1.1.2.3.A, the more stable (and thus first to precipitate during cooling) the precipitate is. Thus, TiN is the most stable precipitate in austenite and VC the least stable. Indeed, VC precipitates at much lower temperatures than Ti(C,N).

Another point of interest is that the nitrides are always more stable than their carbide counterparts. Proper control of the precipitation time and sequence allows for smaller precipitates to be formed. These are desired as they generally increase the strength of the steel as carbonitride precipitates are very hard ceramics and thus non-shearable down to very small sizes due to their strength.

1.1.3 – Solid Solution Strengthening

Solid solution strengthening is the phenomenon of matrix strengthening when solutes are dissolved into it [8]. This is due to the strain dissolved elements put on the lattice due to size mismatch. As the size of the dissolved element is different than that of the matrix, the lattice must bend and strain around it. This strengthens the material as it increases the stress needed for the dislocations to move.

The dissolved solute can either be interstitial or substitutional. Both substitutional and interstitial additions strengthen the alloy, though interstitial additions typically have a more pronounced effect.

The strength with which an element contributes to the increase in strength of an alloy is called its solid solution strengthening coefficient. The higher the value, the stronger the increase in strength. Some common values are included in Table 1.1.3.A [2]:

Table 1.1.3.A: Solid Solution Strengthening Coefficients

Element	Solid Solution Strengthening Coefficient (k, MPa)
C and N	5000
Si	81
Mn	31
Mo	11

The relationship between strengthening and concentration is given either by a linear or a square root relationship as at low concentrations both approximate the same results, albeit with a different k value [2], [21]. For microalloyed steels, as the concentration of alloying additions is very low, a linear relation is used

$$\sigma_{ss} = kc \quad (1.7)$$

with k being the strengthening coefficient given in Table 1.1.3.A, and c being concentration in percent [2].

Of importance to note is that the concentration is the dissolved concentration of the element in the primary phase, not necessarily the concentration of the element in the steel as a whole [21]. Should a new phase or intermetallic occur from the addition of an alloying element, that addition does not contribute to an increase in strength from solid solution strengthening.

1.1.4 – Grain Boundary Strengthening

The grains within a material also act as barriers to dislocation movement, as dislocations have a difficult time traversing the boundary. As such, smaller grains are desired to increase strength. This is a well-known phenomenon that is explained by the Hall-Petch equation

$$\sigma_{GB} = k_y d^{-1/2} \quad (1.8)$$

where k_y is the material's Hall-Petch coefficient and d is the average grain diameter, typically given in microns [8]. In ferritic steels (such as microalloyed steel), the k_y value is estimated to be between 550-600MPa·m$^{1/2}$ [18], [23]. This equation is valid down to grain sizes of around 0.02μm, as smaller grain sizes often exhibit reverse Hall-Petch phenomenon, where they lose strength as they get smaller [23].

The Hall-Petch equation shows that grain size is very important in the strength of the material, with significant contributions with grain sizes below about 10μm (at 10μm the contribution to yield strength is 170MPa).

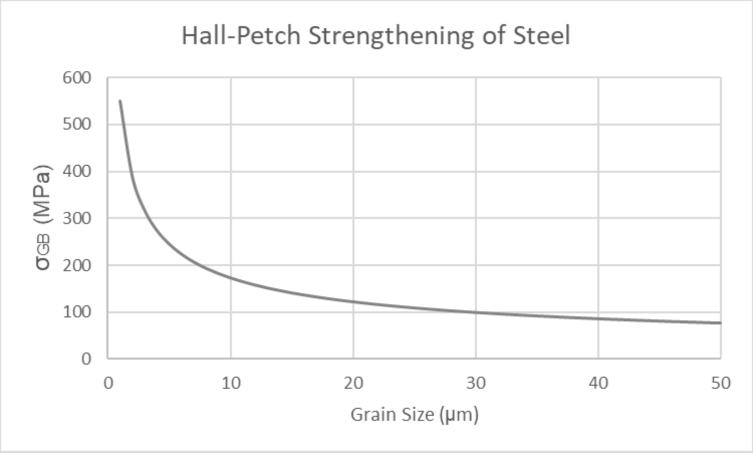

Figure 1.1.4.A: Grain Boundary Strengthening of Microalloyed Steel for Various Grain Sizes

1.1.4.1 – Grain Size Refinement

Grain size refinement is key to creating high strength steels through Hall-Petch strengthening. Fortunately, grain size can be reduced directly during processing of metals through cold rolling. Cold rolling is the process of rolling a sheet of metal at or near room temperature to reduce its thickness. As the number of grains remains constant, the reduction in thickness also translates into a reduction in the thickness of each grain. This strategy can be used to get fine grains down to the micron size [24].

After cold rolling, the grains will be elongated as they follow the flow rules – a reduction in one dimension causes an increase in the dimension of another [25]. By annealing the grains, they can recrystallize to create a more equiaxed structure. Depending on the annealing time and temperatures, the recrystallization process can affect the grain size

Similarly, hot rolling can also be used to refine grain size [26]. During hot rolling, the temperature of the process is increased. This temperature is often, but not necessarily, sufficiently high for recrystallization to occur. Essentially, this combines the rolling and annealing into one step.

Another technique for limiting grain size is through the addition of microalloying elements, specifically Nb, Ti, and V. These elements refine grain size through two methods: solute drag and Zener pinning. Both mechanisms work to slow the onset and the progression of grain growth.

1.1.4.2 – Solute Drag

Solute drag, also called impurity drag, is the resistance to grain boundary or dislocation motion when there is a dissolved element that has segregated [27]. Moving an area of concentrated solute like a grain boundary requires energy, which exerts a force on the grain boundary [27]. This required energy slows recrystallization, which allows the smaller grains formed during mechanical processing and rolling to remain.

Solute drag has been studied extensively, and the model by Cahn will be shown in this thesis [27]. According to Cahn, the force exerted by all the solute atoms on the boundary is

$$P_i = -N_v \int_{-\infty}^{+\infty} (C - C_0) \frac{dE}{dx} dx \quad (1.9)$$

where N_v is the number of atoms per unit volume, C is local concentration, C_0 is the bulk solute concentration, $E(x)$ is the interaction energy and $D(x)$ is the diffusion coefficient [27].

Solving this equation and simplifying results in

$$P_i = \frac{\alpha V C_0}{1 + \beta^2 V^2} \quad (1.10)$$

where V is velocity, and α & β are constants that are inversely proportional to diffusivity and are defined in equations 1.10a and 1.10b, respectively [27].

$$\alpha = 4N_v kT \int_{-\infty}^{+\infty} \frac{\sinh^2 \frac{E(x)}{2kT} dx}{D(x)} \quad (1.10a)$$

$$\frac{\alpha}{\beta^2} = \frac{N_v}{kT} \int_{-\infty}^{+\infty} \left(\frac{dE}{dx}\right)^2 D(x) dx \quad (1.10b)$$

Alternately, an interface mobility can be used [6].

$$M = \left(\frac{1}{M_i} + \alpha C_0\right)^{-1} \quad (1.11)$$

In equation 1.11, M is the mobility, M_i is the interface mobility, C_0 is the solute concentration, and α the parameter defined in equation 1.10a that includes both the cross-boundary solute diffusion constant as well as the binding energy between the solute and the boundary [6].

Equation 1.11 shows that more solute drag results in reduced mobility, which in turn results in slower recrystallization kinetics as well as better resisting grain growth during annealing or hot rolling [28]. As recrystallization is activated by temperature, using a lower annealing or hot rolling temperature results in smaller grains in the final microstructure.

1.1.4.3 – Zener Pinning

Grain growth can also be resisted and slowed by the addition of precipitates. These precipitates pin the grain boundaries and can potentially stop grain growth [29]. A high volume fraction of fine precipitates is the most effective at slowing grain growth. For the grain to advance past a precipitate which is located at the boundary, it is necessary to create new grain boundary area equal to the cross-sectional areas of the precipitate.

The limiting grain size that can be formed in the presence of precipitates depends on the precipitate size and volume fraction [30]

$$D = \frac{1}{K}\frac{r_{ppt}}{f} \quad (1.12)$$

with D being the mean grain size, r_{ppt} the radius of the precipitate, f the volume fraction of precipitates, and K the Zener coefficient, which depends on the shape of the precipitate [30]. The Zener coefficient is typically given a value between 1.00 and 5.00, with 1.33 for spherical precipitates and 3.01 for cubic precipitates, though this value depends on the angle of the cube relative to the grain boundary [29],[30],[31]. As seen in Figure 1.1.4.3.A, cubic precipitates are more effective at reducing grain size than spherical particles as their average K value is larger [30].

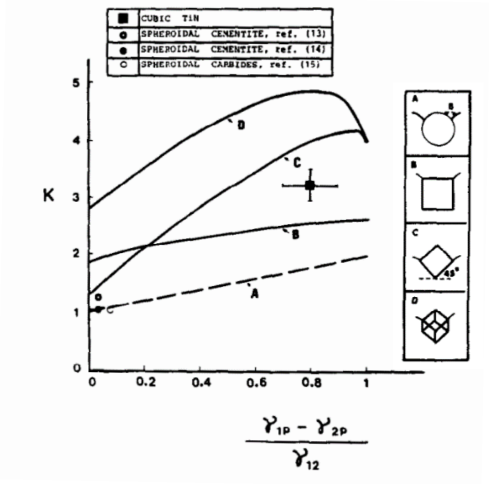

Figure 1.1.4.3.A: K Values for Various Precipitate Geometries and Orientations [30]

Examples of spherical precipitates include many carbides, such as VC. Cubic precipitates are much more limited, with the best studied example being TiN. Lamellar particles have been shown to be largely ineffective at Zener pinning [32].

Another aspect that matters is the coherency of the particles. A more coherent particle is often better at slowing grain growth than an incoherent particle [30]. Coherency refers to the continuation of the lattice across the precipitate-matrix boundary as they have the same crystal structure [33]. By allowing the lattice to continue across the boundary, there is a strain field generated as the lattice parameters of the matrix and precipitate are different. A loss in this coherency increases the interfacial energy of the precipitate which results in a greater energy penalty [32].

1.1.5 – Dislocation Strengthening

Dislocation strengthening, sometimes referred to as work hardening due to its primary mechanism of employment, is the process by which an increase in the number of dislocations in a metal increases its strength [8]. Specifically, each dislocation creates a stress field around it with the interaction of multiple stress fields being overwhelmingly repulsive in nature, which in turn slows overall dislocation movement [8].

To increase the number of dislocations, plastic deformation must be applied to the metal below its recrystallization temperature [25]. Common ways to achieve this include cold rolling, hot rolling, and metal forming. This deformation leads to an increase in dislocations as the lattice is distorted, and the low temperature makes recovery slower. The amount with which a metal hardens during plastic deformation is called the strain hardening rate. There are many equations to describe this rate, with one common one being the power law relation [25]

$$\sigma_{dis} = K\varepsilon^{n} \quad (1.13)$$

with σ_{dis} being true stress, ε true strain, and K and n curve-fitting parameters with $n < 1$. This relationship can be seen in the graph of true stress-strain curves, and shows that the contribution to strengthening through work hardening is significant and is a major factor in the properties of materials.

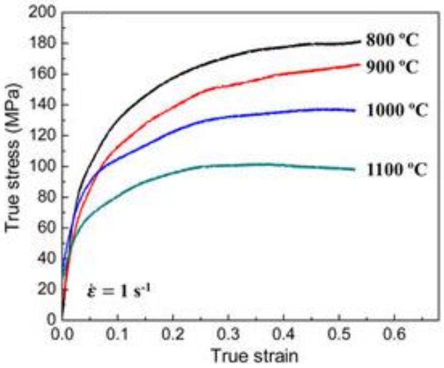

Figure 1.1.5.A: True Stress-Strain Curves for Various Tempers of a 0.151wt.%C HSLA Steel [34]

The contribution to total strength from work hardening can be quite substantial, and is one of the reasons why cold working is often performed. However, strain hardening can make a metal brittle so care must be used when using this method.

1.1.6 – Transformational Related Strengthening

The final method of strengthening steel involves phase transformations. While austenite can be used to improve the properties of steel, this typically only occurs in high carbon or stainless steels [35], [36]. As such, these strengthening mechanisms such as TRIP and TWIP are outside the realm of possibility for microalloyed steel. Nonetheless, martensitic steels, including dual-phase steel, are possible with microalloyed steel compositions.

Martensite is metastable phase that has a body-centred tetragonal crystal structure [8]. While brittle, it is very strong and so is often used to strengthen steel through the creation of martensitic, tempered martensitic, and dual-phase steels. Martensite is formed through the diffusionless transformation of austenite (FCC) to martensite (BCT; body centred tetragonal) upon quenching the steel [8]. Martensite must be formed by quenching or rapid cooling as it is a non-equilibrium phase, and so can only be created when timescales are too small to allow for the diffusion of the atoms to form an equilibrium phase such as ferrite or cementite. Increasing the carbon content can help slow the formation of ferrite such that martensite can be more easily created which allows for somewhat slower cooling times to be realized [8].

To determine if and how much martensite will be created, time-temperature-transformation (TTT) and continuous cooling transformation (CCT) diagrams are used.

A calculated TTT diagram of a model (0.04%C, 1.6%Mn, 0.6%Si, 0.25%Mo) microalloyed steel is shown in Figure 1.1.6.A, calculated using the McMaster Materials Virtual Laboratory Software.

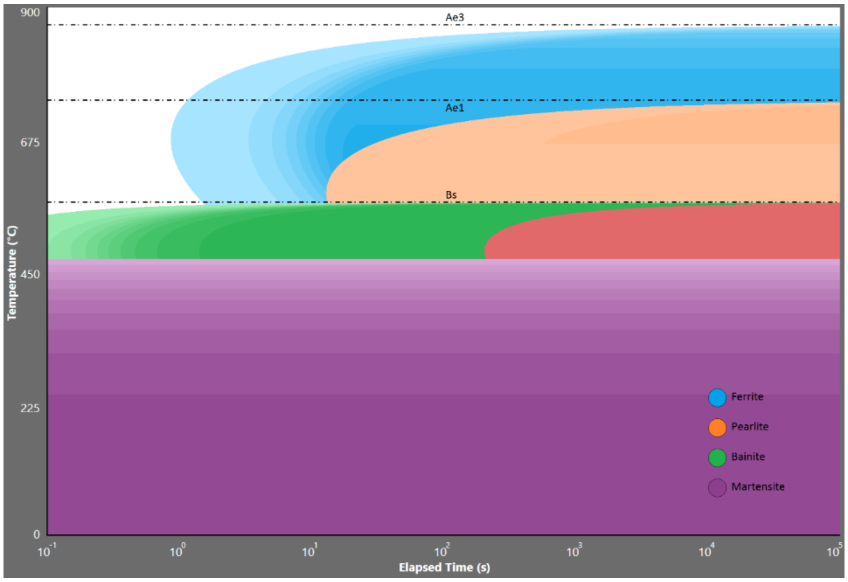

Figure 1.1.6.A: TTT Diagram for a Microalloyed Steel

1.1.7 – Recovery-Annealed Steels

A relatively new and interesting class of steel is called recovery-annealed or back annealed steels. In these steels, the grains are recovered, but not recrystallized. Recovery is a process that involves the annihilation and rearrangement of defects within the material, whereas recrystallization is the growth of new grains from old grains [37]. By reducing the number of dislocations through the recovery of the metal, the ductility is increased while still maintaining much of the strength as the grains have not yet recrystallized.

To create these microstructures, the first step is to cold work or cold roll the steel to induce plastic deformation and create the strained and smaller grains for strengthening. Afterwards, the metal is heated to a temperature sufficient to induce recovery, but not too high nor for too long a time as to not induce much recrystallization. This is achievable as recovery generally occurs before recrystallization. Nonetheless, care must be taken to avoid recrystallization as this would reduce much of the strength gained from cold working. Recrystallization typically starts around 400°C to 600°C in low carbon steels, though this varies significantly with composition and cold working. Nonetheless, this temperature is often lower than the annealing temperature, so some recrystallization is inevitable during the batch annealing process [38].

1.1.7.1 – Recrystallization Kinetics

The rate of recrystallization varies depending on the composition of the steel and stored energy. The recrystallized fraction is determined by the Johnson-Mehl-Avrami-Kolmogorov (JMAK) equation which is shown in equation 1.14 [39].

$$X = 1 - \exp(-kt^n) \quad (1.14)$$

The recrystallized fraction is given by X, k is a material dependant constant, t is time, and n is the Avrami constant and varies depending on the dimensionality of the grain growth [39].

The dimensionality of the grain growth depends on the material. For nearly pure metals, such as IF steel, the Avrami constant is around 1; for highly unordered materials such as an amorphous alloy, the Avrami constant is around 3 [39], [40].

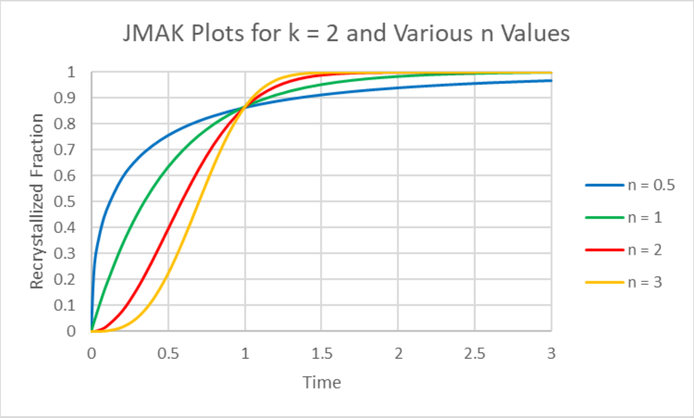

Figure 2.1.7.1.A: JMAK Plots for k = 2 and Various n Values

To approximate the recrystallized fraction, one simply needs to know the yield strength or microhardness of the fully unrecrystallized and recrystallized fractions and then a proportionality between the two can be estimated using [41]

$$X = \frac{Z_{CW} - Z}{Z_{CW} - Z_{Annealed}} \quad (1.15)$$

with X being the recrystallized fraction, Z the property of the sample in question, Z_{CW} being the property of the cold worked sample, and $Z_{Annealed}$ the property of the fully annealed or fully recrystallized sample. To slow recrystallization, one approach is through the addition of certain microalloying elements, namely Ti, Nb, and V [41]. These additions slow recrystallization through Zener pinning from precipitates or through solute drag due to segregation of these elements [41]. With these alloying additions, the recrystallization time can be pushed to over 10^6 seconds as shown in Figure 1.1.7.1.B [41].

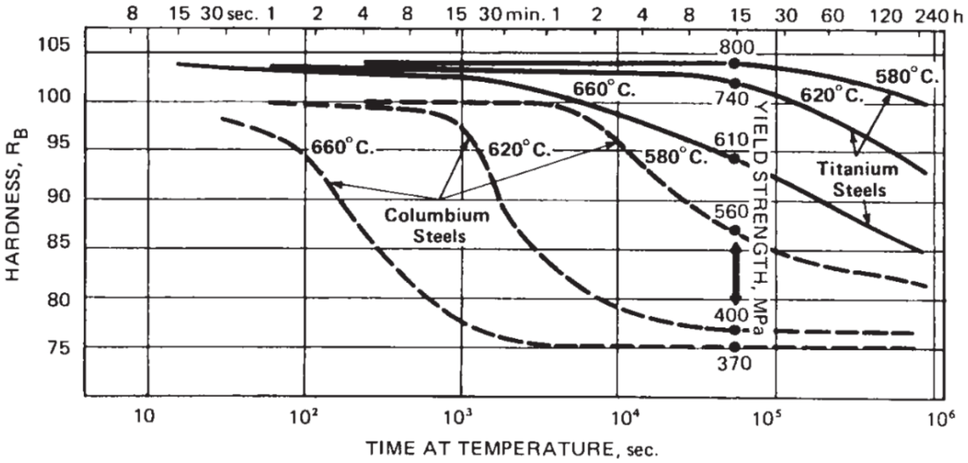

Figure 1.1.7.1.B: Hardness (as a Proxy for Recrystallized Fraction) vs. Time for Various Steel Chemistries [41]

Having longer recrystallization times ensures that recrystallization does not occur during the period of recovery. Furthermore, it gives a larger processing window to anneal the steels. Both of these are crucial in the creation of recovery-annealed steels.

1.2 – Batch Annealing Principals

Batch annealing is a process by which a metal is rolled into large coils and then those rolls are heated in a large furnace. The coils are roughly two meters wide, one meter tall and weigh roughly twenty tons [42]. Three, four, or five of these coils are stacked on top of each other and then a bell-shaped furnace is lowered over them [42]. The atmosphere inside the bell is purged and replaced with an inert or a hydrogen-enriched atmosphere and then heated. A diagram is included in Figure 1.2.A [43].

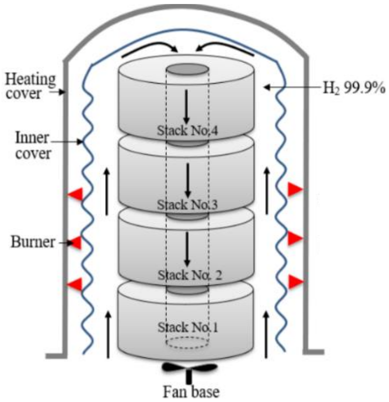

Figure 1.2.A: Illustration of a Batch Annealing Furnace [43]

Batch annealing contrasts with continuous annealing whereby a thin strip of steel is heated as it moves through a furnace. The major difference between the two from a metallurgical perspective is that strip is quite thin, and so can be heated and cooled very quickly. Batch annealing, due to the large size of the coils, and specifically the slower heat transfer through those coils, does not allow for rapid changes of temperature. However, batch annealing does permit for much longer annealing times to be realized, which can be desirable for the production of certain grades of steel.

1.2.1 – Batch Annealing Cycle

A batch annealing cycle is characterized by three main stages: heating, soaking, and cooling [43]. In the heating phase the coils are heated slowly until they reach the target temperature. The soaking phase consists of a hold at a continuous temperature to anneal the steel. Lastly, the coils are slowly cooled. This whole process takes around 24 to 48 hours, depending on soak time [43]. The heating and cooling rates are limited by the slow heat transfer through the large coils and large furnace and are roughly +100°C/hour and -50°C/hour, respectively [44]. An additional pre-soak may be added to try and homogenize the temperature of the coils.

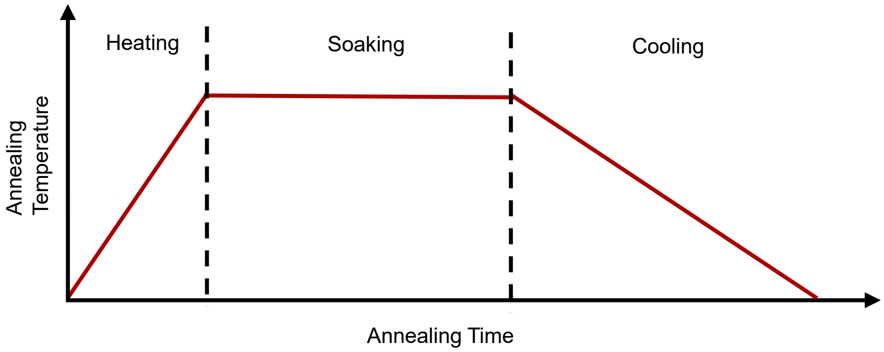

Figure 1.2.1.A: An Idealized Heat Treatment for a Batch Annealing Process Based off Maximum Heating and Cooling Rates [44]

1.2.2 – Heat Transfer During Batch Annealing

Due to the large size and mass of the coils, they do not heat quickly nor evenly. Consequently, their temperature profile during heating is not uniform. However, it can be modeled using equations of heat transfer or experimentally measured by placing probes at various locations within a coil. As the coils are heated in a gaseous atmosphere with a fan, they are subject to forced convection. The equation for forced convection is given in equation 1.16 [45].

$$q'' = h\left(T_s - T_{fluid}\right) \quad (1.16)$$

The heat flux is q'', the convection heat transfer coefficient is h – typically between 25-250 W/m^2K for forced convection of a gas, T_s the temperature of the surface and T_{fluid} the temperature of the fluid (in this case the furnace atmosphere) [45].

The temperature profile within the coils can be given by a lengthy differential equation solved in cylindrical coordinates but, the key concept is that there are hot and cold spots. The hot point occurs at the outer edge of the coil, and the cold point 3/5 the way towards the centre of the coil [43].

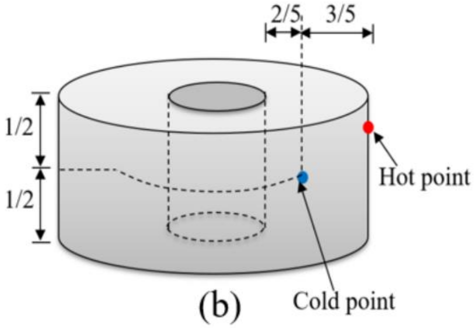

Figure 1.2.2.A: Hot and Cold Points Within a Coil [43]

The rates at which these different points heat up is significant, with the hot point potentially being hundreds of degrees hotter than the cold point during the heating phase.

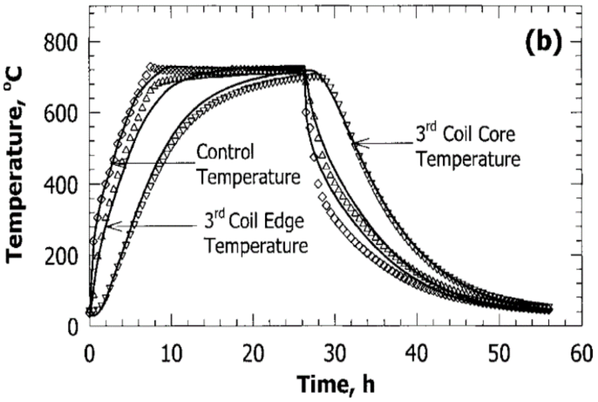

Figure 1.2.2.B: Experimentally Measured (Shapes) and Theoretical (Lines) Temperature Profile of Hot and Cold Points Within a Coil [42]

As such, a metal must have the desired properties both when the hot point and the cold point heat treatments are done. If not, the properties will vary too much depending on their location within the coil.

1.2.3 – Challenges of Batch Annealing

The primary challenge within batch annealing is achieving uniform properties within the coil. The potential for variation in properties arises due to the varying heating rates within the coil as a consequence of their large size. As seen in Figure 1.2.2.B, the effective heat treatments between the hot point and cold point may be substantial. Metals, including microalloyed steels, are very sensitive to the effects of heat treatment; that is their properties can vary substantially stemming from only a relatively small difference in heat treatment and processing conditions. If the metal is too sensitive, its properties will be different depending on where in the coil it was. As such, for any metal to be feasibly annealed with a batch annealing furnace, it must have an adequately large processing window such that the variation of temperatures within the coil does not bring the properties outside of specifications.

1.2.4 - Strengthening Mechanisms Compatible with Batch Annealing

Most strengthening mechanism can be used with batch annealing quite well. However, not all methods are compatible.

Intrinsic strength will contribute to the strength as this property that is invariant with the material. Solid solution strengthening is also compatible as the strength comes from dissolved elements, which stay dissolved during batch annealing. Precipitate strengthening works exceptionally well with batch annealing. This is because the longer times of the heat treatment give more time for precipitation reactions to occur, and thus one can produce substantial precipitation. However, the precipitates may coarsen during the long time which could cause overaging and reduce the strength. Furthermore, many precipitates that are already present (TiN in steel for example) have such high temperature requirements for solubility that they remain unaffected during the relatively more moderate temperatures of batch annealing [2]. Lastly, dislocation strengthening is also feasible as with lower temperatures and specially designed steels, one can retain some strength in the material after batch annealing.

The major exception to compatibility is transformational related strengthening, specifically martensitic transformations. This is because martensite requires rapid cooling. The very slow cooling that occurs during batch annealing makes the creation of martensite quite difficult as seen shown in TTT and CCT diagrams. Similarly, finely tuning the percentage of pearlite and bainite and ferrite is also a challenge. These are not small considerations as martensite is often hundred of megapascals stronger than ferrite for a given steel composition [46].

From a practical standpoint, this consideration means that all the strength of the steel must come from the other strengthening mechanisms. As intrinsic strength is a fixed property, one must generate almost all of the strength through the use of precipitation, solid solution strengthening, and dislocation strengthening. This factors into alloy design which will be elaborated upon in sections 2.0.1 and 3.0.1.

Section 2 – Precipitation Hardened HSLA Steel

2.0 – Alloy and Process Design

The composition and processing parameters were chosen to create a steel with the desired mechanical properties, with a large part of the strengthening coming from precipitation strengthening and a heat treatment that ensures adequate ductility in the steel without a loss of too much strength. This precipitation hardened HSLA steel will be referred to as V10 throughout the thesis.

2.0.1 – Alloy Design

The chemistry of the steel was designed by CanmetMATERIALS. The chemistry was chosen to create a relatively large volume fraction of fine precipitates in order to strengthen the steel. Furthermore, many different carbonitride forming metals were used as they form different precipitates at different temperatures. The chemistry is shown in Table 2.0.1.A:

Table 2.0.1.A: Chemistry of the V10 Steel

Fe	C	Mn + Si	Mo	Al	Nb + V + Ti	S	N
Bal	0.050	2.00 – 2.50	0.16	0.050	0.20 – 0.30	0.001	0.005

Different elements are added for different purposes. Carbon is an essential element to add to steel. It allows for the creation of carbides and carbonitrides. The carbon reacts with many of the microalloying additions to form carbides and carbonitrides. These carbonitrides enable a large increase in strength for a relatively small compositional change; in fact, these additions specifically are what define many of the properties of microalloyed steel. Note that carbon also significantly increases strength through solid solution strengthening in simple carbon steels, but in V10 the carbon is sequestered in the form of carbides and carbonitrides, so this was not a major consideration.

Another element almost always added to steel is manganese, and V10 is no exception. In this steel it serves two main functions. Firstly, the manganese contributes to solid solution strengthening as seen in section 1.1.3. Secondly, manganese decreases the brittleness of the steel [2]. In this regard, manganese is special in that it increases the strength of the steel without a loss of ductility. Lastly, it decreases the austenite to ferrite transition temperature which generally results in finer grains in the resulting ferrite microstructure [2].

Silicon in steel has functions similar to manganese. Principally, silicon is added to increase the strength of the steel through solid solution strengthening. Silicon is roughly 2.6 times more efficacious than manganese, so relatively small additions have a noticeable effect on the properties of steel [2]. Furthermore, like manganese, silicon additions do not negatively affect the ductility of the steel at these concentration as they encourage more uniform elongation of the ferrite grains [47].

Molybdenum, vanadium, niobium, and titanium are all traditional microalloying additions. They react with the carbon and nitrogen in the steel to form their respective carbonitrides. In turn, this increases the strength through precipitation strengthening. As their carbonitrides have different solubility, they will precipitate at different times. With TiN being the most stable, it will precipitate first and sequester much of the nitrogen, which can be advantageous as nitrogen can embrittle steel [2]. Vanadium was of key interest as it stays in solution longer (at lower temperatures) than the other elements, as shown in Figure 2.3.1.1.B. Specifically, VC is the least stable precipitate and is able to precipitate at temperatures reached during batch annealing. Molybdenum is also of interest as it forms interphase precipitates with the other microalloying elements present, which increases strength and help in the formation of finer precipitates [48].

2.0.2 – Process Design

The process design includes two parts: mechanical processing (rolling) of the steel and the heat treatment of the steel. The mechanical processing was performed in line with standards operated at CanmetMATERIALS. This will be expanded upon in section 2.1, experimental methods. The heat treatment was carried out in the range of temperatures from 650°C to 700°C to find the optimal properties. The duration, heating rate, and cooling rate of these trials is limited by the batch annealing process.

2.1 – Experimental Methods

This section on experimental methods outlines all of the procedures that took place, including casting, rolling, heat treatments, tensile testing, and sample preparation for optical and electron microscopy. Some minor details of the coiling process were omitted at the request of CanmetMATERIALS to maintain their intellectual property.

2.1.1 – Casting

The steel was melted in a vacuum induction furnace. It was cast into two 50kg ingots. These were of identical composition, save for the addition of extra Nb added to the second cast. The second cast with the higher Nb content is the V10 steel that is studied in this report.

2.1.2 – Hot Rolling

The ingot was first heated to 1260°C before being hot rolled on CanmetMATERIALS's pilot mill to a 95% reduction according to Table 2.1.2.A.

Table 2.1.2.A: Hot Rolling Schedule for the V10 Steel

	Pass 1	**Pass 2**	**Pass 3**	**Pass 4**	**Pass 5**	**Pass 6**	**Pass 7**	**Total**
Entry (mm)	130	105	75	40.5	21	12	6.5	
Exit (mm)	105	75	40.5	21	12	6.5	3.5	
True Strain	0.25	0.39	0.71	0.76	0.65	0.71	0.71	3.46
Temp (C)	1219	1217	1204	1195	1177	1162	1162	
Reduction%	19	29	46	48	43	46	46	95

The strip was then rapidly cooled from 1162°C to 650°C. Still at 650°C, they were coiled at a rate of 83-90m/min. Coiling time and temperature are purposefully not included due to intellectual property reasons.

2.1.3 – Cold Rolling

The coils were then cold rolled on the same pilot mill to a final thickness of 1.2mm, for a 66% cold working reduction.

2.1.4 – Cutting of Tensile Test Bars

The tensile samples were cut from the sheet metal using a waterjet cutter. They were cut such that the transverse direction is parallel with the direction of the force applied during tensile testing.

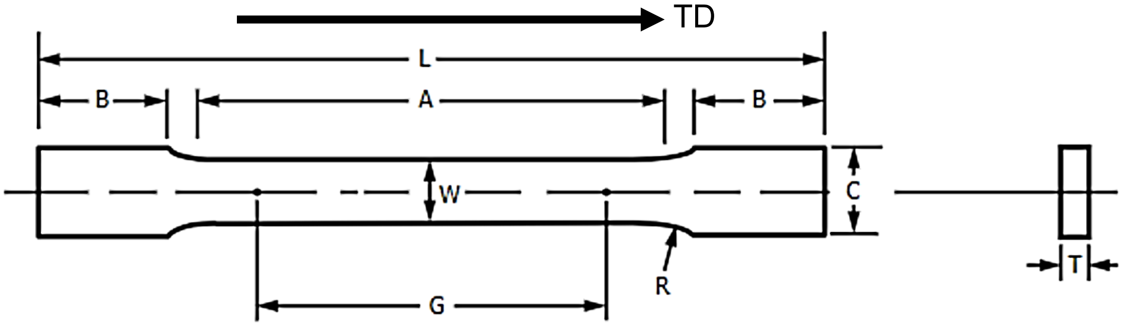

Figure 2.1.4.A: Diagram of Tensile Test Bar Geometry

Table 2.1.4.A: Dimensions for Tensile Test Bar in mm

G	W	T	R	L	A	B	C
50.0	12.5	2.00	12.5	200	57 (min)	50 (min)	~20

2.1.5 – Heat Treatments

The heat treatments were performed in two separate locations, but their procedures are nearly identical. The first was at CanmetMATERIALS’s batch annealing furnace. They were heated in the batch annealing furnace under an argon atmosphere. The second was at McMaster in a tube furnace, also under an argon atmosphere. The thermal cycle for the samples heated at CanmetMATERIALS is shown in Figure 2.1.5.A. Note that the “Soak #2” temperature changes with the sample being tested.

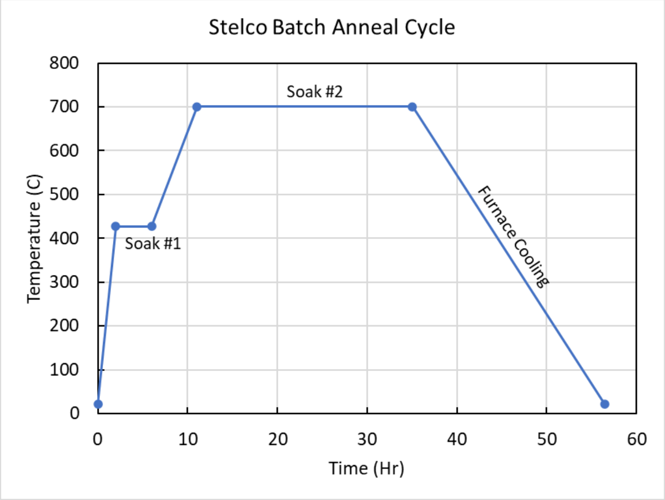

Figure 2.1.5.A: Thermal Cycle for Samples Heated at CanmetMATERIALS

The sample heated at McMaster was to emulate the cold point, so the heating cycle was slightly different: heat at +30°C/h from room temperature to target temperature, hold for 12 hours at target temperature, and cool at -30°C/hour back to room temperature. This contrasts with the heat treatments done at CanmetMATERIALS for the hot point as the heating rate is +60°C/h and the soak time is roughly 24 hours.

2.1.6 – Optical Microscopy Sample Preparation

The samples for optical microscopy were prepared following standard metallography procedures. The samples were cut from the grip section of the tensile tests. They were then either cold mounted in epoxy or hot mounted in Bakelite. After mounting, they were sanded on a Struers Tegramin-25 auto polisher using silicon carbide sandpaper in grits ranging from 320 to 4000. After the sanding they were rinsed off and cleaned before starting the final polishing. The polishing was done using the same auto polisher. Microfibre polishing pads with a diamond abrasive were used, with three rounds of polishing using sizes of 6μm, 3 μm, and 1μm. Finally, the were washed with water and then ethanol. After cleaning, they were etched using a solution of 2% nital (nitric acid) applied for approximately 3 seconds to reveal the microstructure. The images were taken on a Nikon microscope at magnifications ranging from 200x to 1000x.

2.1.7 – SEM Sample Preparation

The samples for the SEM were prepared following the same steps as in the optical microscopy with the following additional steps. The first additional step is after polishing at 1μm using diamond polish, a final polishing step using an aluminum oxide suspension of 0.05μm was used for a final polish. After this step the surface was wiped with a wet cotton-ball and then cleaned with ethanol. The samples were then etched using the same procedure used for optical microscopy.

Additional steps must be taken to make the sample compatible with electron microscopy. Two lines of nickel paint were added to the surface and sides of the sample to create a path through which electricity can flow to dissipate charging effects within the electron microscope. After painting these lines, they were dried in an oven at 50°C for half an hour. Lastly, they were coated in a 10nm thick layer of carbon to further increase the sample's conductivity and reduce charging in the SEM.

The JEOL 7000 was used for the purpose of imaging. Images were taken at 5000x and 20000x magnification. An accelerating voltage of 20kV and a working distance of 10mm was used to capture the images.

2.1.7.1 – EBSD Sample Preparation

EBSD sample preparation is exactly the same as that of standard SEM sample preparation, but with a second polishing with the 0.05μm alumina suspension.

The JEOL 7000 was also used for EBSD. To perform EBSD, the sample in the microscope must be tilted at a 70° angle and a working distance of 15mm was used.

2.1.8 – TEM Sample Preparation

For this application of TEM, thin foils were prepared. A sample of the material was glued onto a metal disc for easier holding, before being ground down on a sanding wheel to roughly 500μm. From there, they were attached to a special holder and hand sanded using 400 grit SiC paper down to roughly 200μm. The final sanding was done using 600 grit sandpaper to achieve a final thickness of 150μm. Lastly, 3mm discs were punched out of the metal.

These 3mm discs were then electropolished using a solution glacial acetic acid with 5% perchloric acid at a voltage of 20V and at room temperature.

For TEM imaging, the Talos 120C was used, and for EDS the Talos 200X was used. The same samples were used in both microscopes.

2.2 – Results

This section includes the results of all experiments performed, including tensile testing, SEM, EBSD, TEM, and EDS. These sections aim to cover mechanical properties and microstructural characterization.

2.2.1 – Mechanical Properties

Uniaxial tensile testing was used to determine the mechanical properties of the steel. Specifically, a uniaxial tensile test with an attached extensometer to create stress-strain curves. The crosshead speed was 5mm/min and the gauge length was 50mm. From these curves, the yield strength was determined using the 0.2% offset method and the tensile strength from the maximum force supported. An upper and lower yield strength are also included due to the shape of the tensile curves. The ductility is measured as percent elongation at fracture. The results of the tensile tests are included on the following page. Please note that the ± values refer to a 90% confidence interval and are calculated using a t-test with a t-value of 6.314. 90% was chosen rather than 95% as only duplicates were performed, so the 95% confidence interval would be too large to be meaningful due to the large t-value associated with only having two data points. With a third test, these values could be reduced substantially. Also, due to the more random nature of elongation at fracture, care should be used when interpreting their confidence intervals.

Table 2.2.1.A: Mechanical Properties of the V10 Steel for Different Heat Treatments

	YS 0.2% (MPa)	UTS (MPa)	% El. (50mm Gauge)	YS Upper (MPa)	YS Lower (MPa)
650°C 1	727	780	10.2	747	711
650°C 2	710	774	12.1	734	704
650°C AVG	718 ± 54	777 ± 19	11.2 ± 6.0	740 ± 32	708 ± 22
670°C 1	602	671	15.4	648	594
670°C 2	608	679	15.4	654	607
670°C AVG	605 ± 19	675 ± 25	15.4 ± 0.0	651 ± 19	600 ± 41
680°C 1	517	607	17.0	565	510
680°C 2	505	598	16.4	559	499
680°C AVG	511 ± 38	602 ± 28	16.7 ± 1.9	562 ± 19	504 ± 35
700°C 1	450	541	23.1	486	441
700°C 2	463	551	21.4	490	457
700°C AVG	456 ± 41	546 ± 32	22.2 ± 5.4	488 ± 13	449 ± 51

These mechanical results show there is a very strong relationship between the annealing temperature and the properties. Assuming a linear relationship within the range of temperatures being studied, we can derive relations for describing the variation of strength and elongation at different temperatures.

From Figure 2.2.1.A, for every 1°C increase in annealing temperature, a decrease to the yield strength of 5.4MPa is expected.

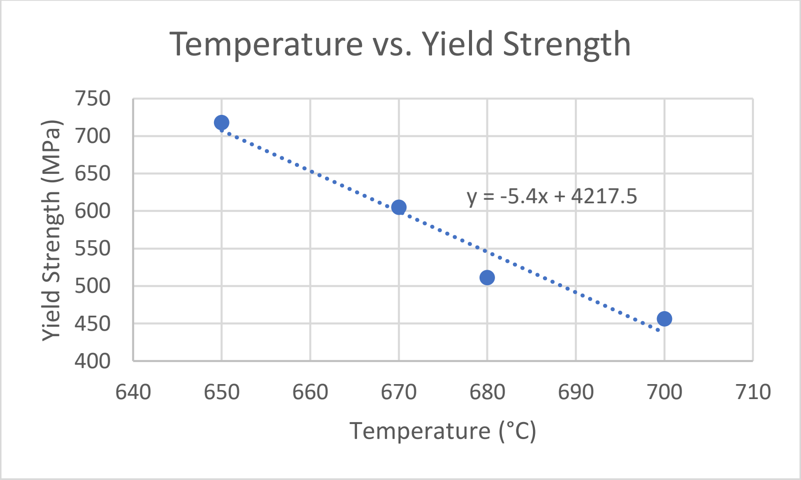

Figure 2.2.1.A: Effect of Temperature on Yield Strength

Likewise, for every 1°C increase in annealing temperature, an increase to the elongation at fracture of 0.22% is expected.

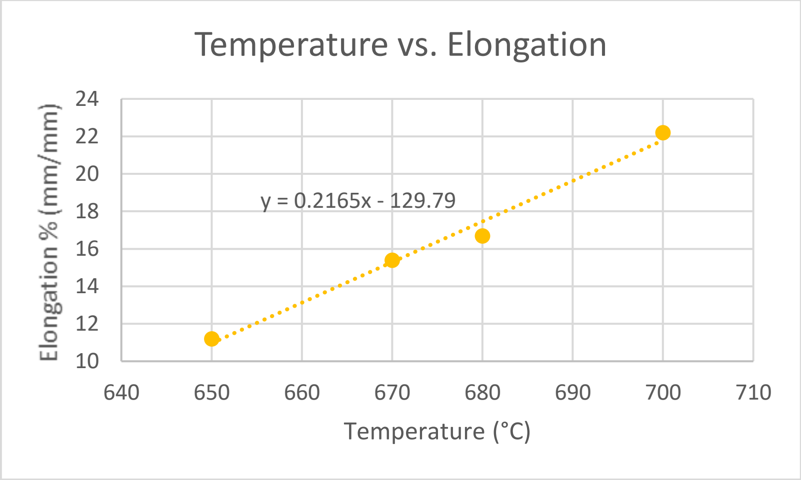

Figure 2.2.1.B: Effect of Temperature on Elongation at Fracture for 50mm Gauge

The values for yield strength, tensile strength, and elongation were derived from the stress-strain curves shown in Figure 2.2.1.C:

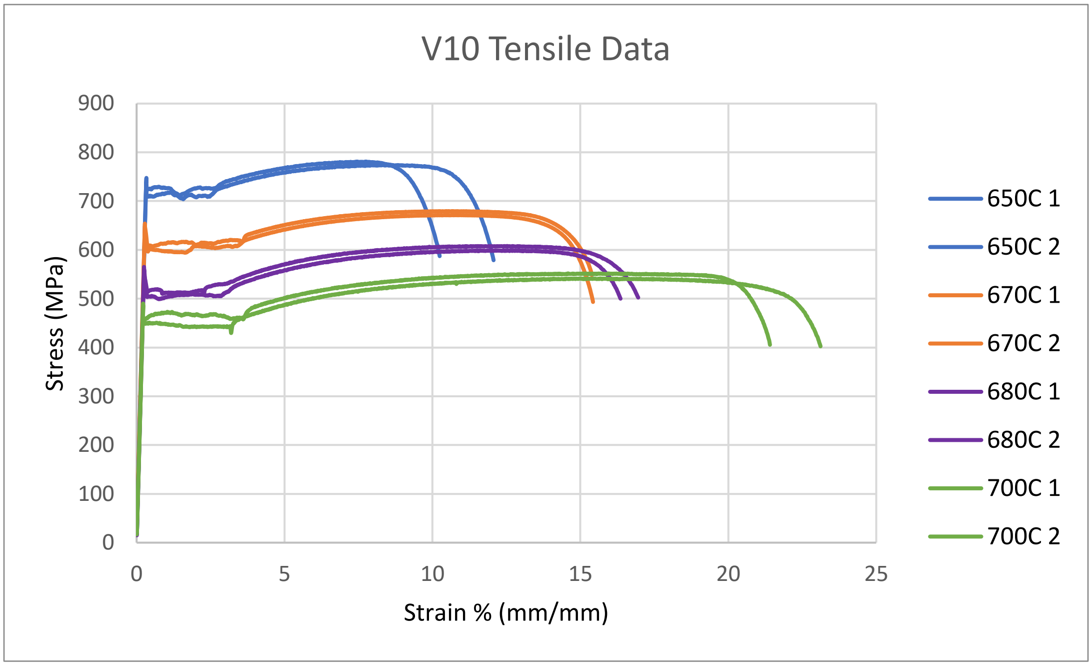

Figure 2.2.1.C: Stress-Strain Curves for Various Annealing Temperatures

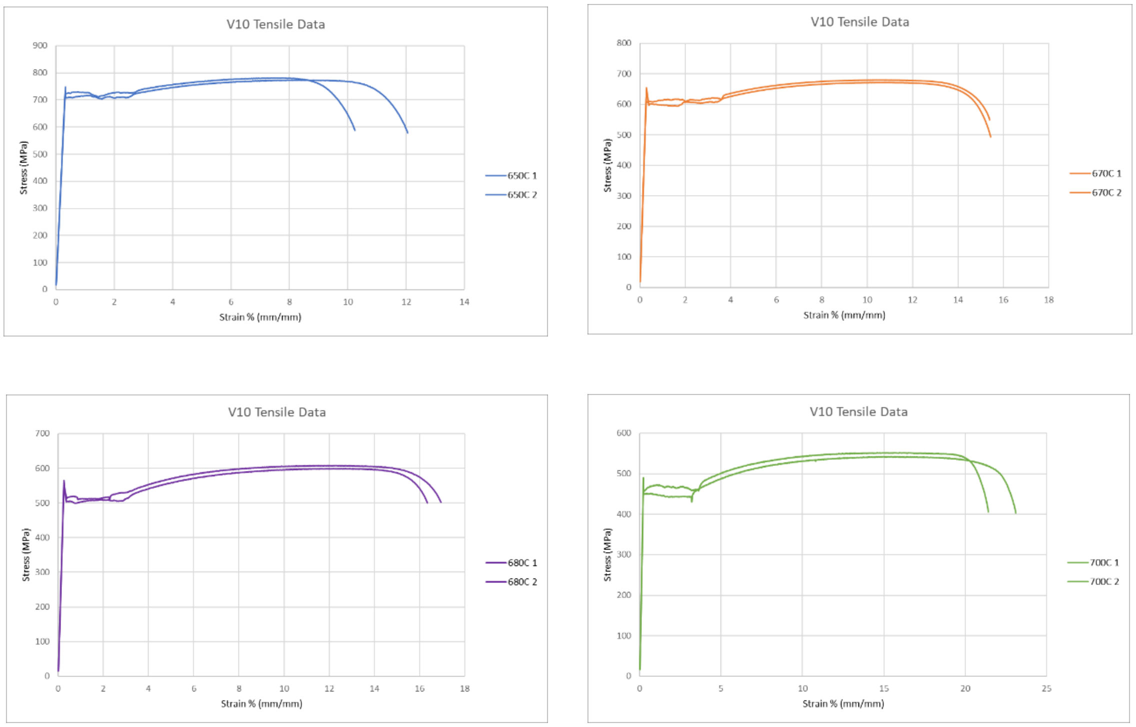

Figure 2.2.1.D: Stress-Strain Curves for Annealing at a) (Blue) 650°C, b) (Orange) 670°C, c) (Purple) 680°C, and d) (Green) 700°C

2.2.1.1 – Cold Point Mechanical Properties

The values given in the previous section (2.2.1) are the properties that would be achieved ideally, which in this case would be the hot point properties. To ensure the viability of the steel, the cold point properties must also be examined to ensure that they are also acceptable.

The cold point for a heat treatment at 700°C was simulated by heating the sample at 30°C/hour to 695°C, holding for 12 hours, then cooling at 30°C/hour back to room temperature. This estimation comes from the experimentally measured cold point profiles [42].

The sample was mechanically tested using uniaxial tensile testing as the other samples. The results from this test, in the form of a stress-strain curve, are given in Figure 2.2.1.1.A.

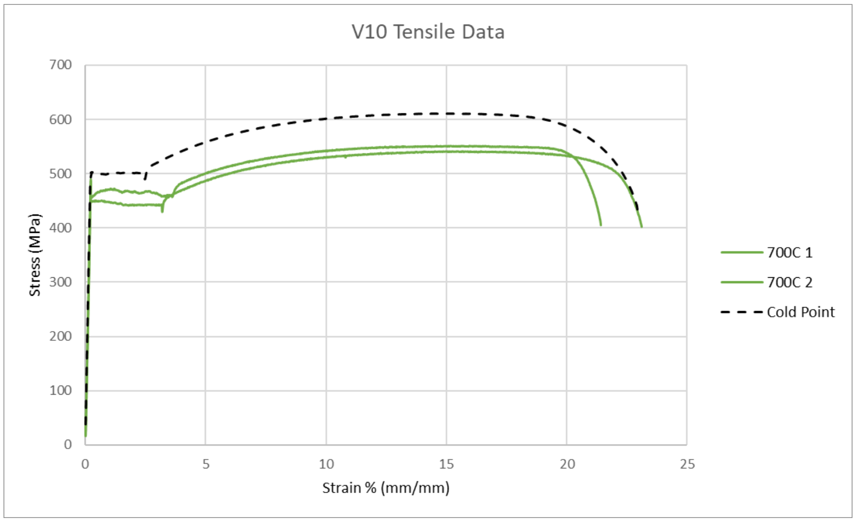

Figure 2.2.1.1.A: Stress-Strain Curves for Hot and Cold Point Properties for an Annealing at 700°C

Using the 0.2% offset method, the yield strength is 501MPa, with a tensile strength of 610MPa and an elongation at fracture of 22.9%. This is comparable to, and in fact slightly better than the hot point properties.

2.2.2 – Microstructural Characterization

The microstructure of the steel was verified using optical microscopy, SEM, TEM, EBSD, and EDS for various heat treatments.

2.2.2.1 – Optical Microscopy

Optical micrographs were taken at mid-thickness for the samples at the heat treatments at 650°C, 680°C, 700°C, 700°C cold point (CP), and as rolled. Representative photos at different magnifications are shown for each heat treatment.

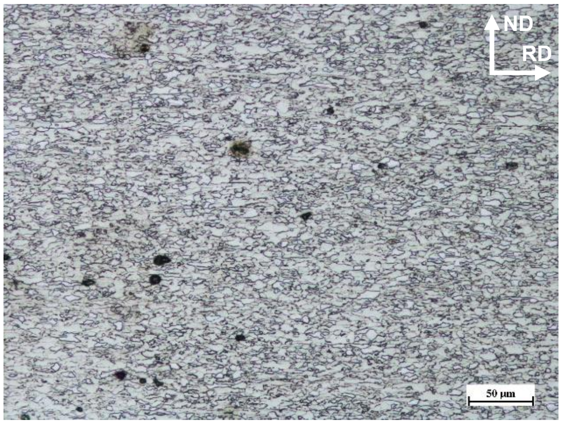

Figure 2.2.2.1.A: 650°C Heat Treatment at 200x Magnification

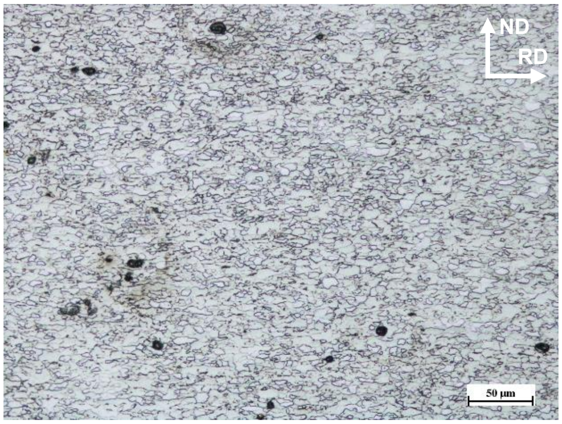

Figure 2.2.2.1.B: 680°C Heat Treatment at 200x Magnification

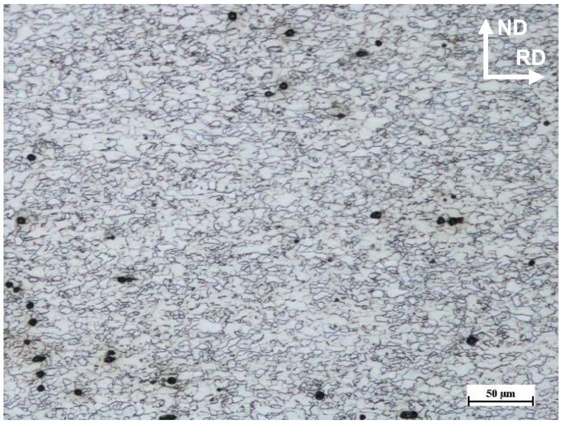

Figure 2.2.2.1.C: 700°C Heat Treatment at 200x Magnification

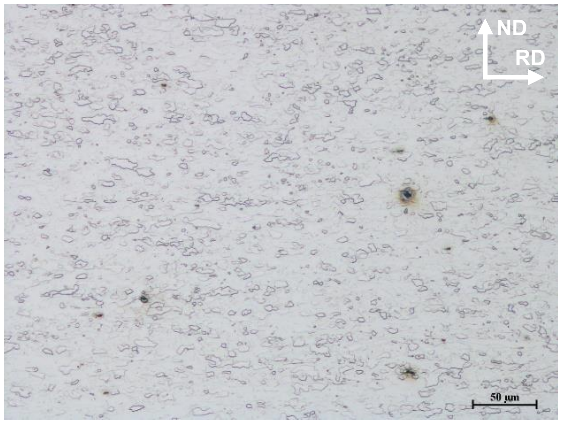

Figure 2.2.2.1.D: 700°C CP Heat Treatment at 200x Magnification

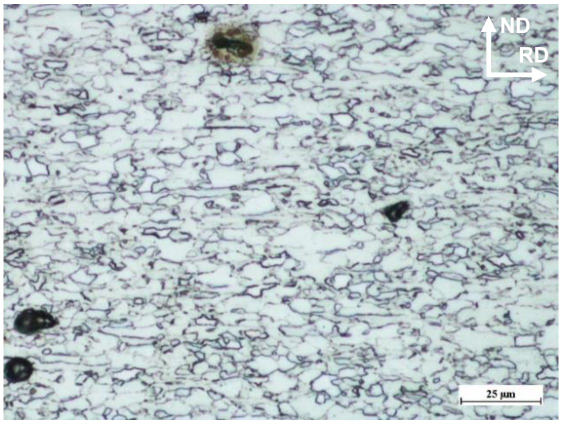

Figure 2.2.2.1.E: 650°C Heat Treatment at 500x Magnification

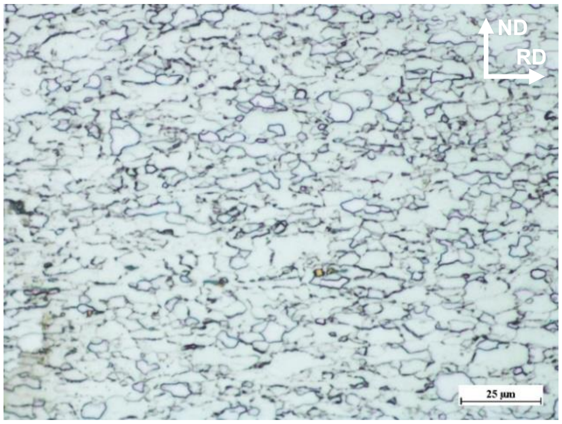

Figure 2.2.2.1.F: 680°C Heat Treatment at 500x Magnification

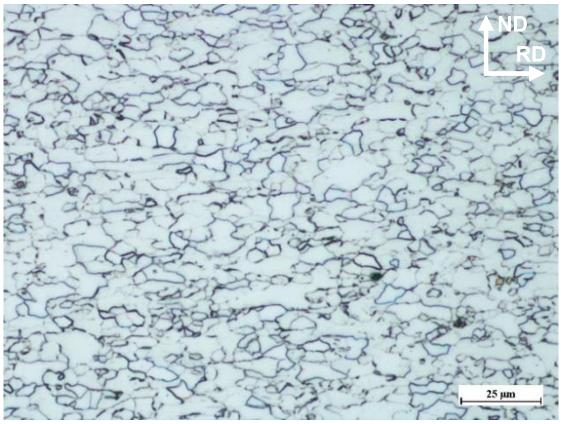

Figure 2.2.2.1.G: 700°C Heat Treatment at 500x Magnification

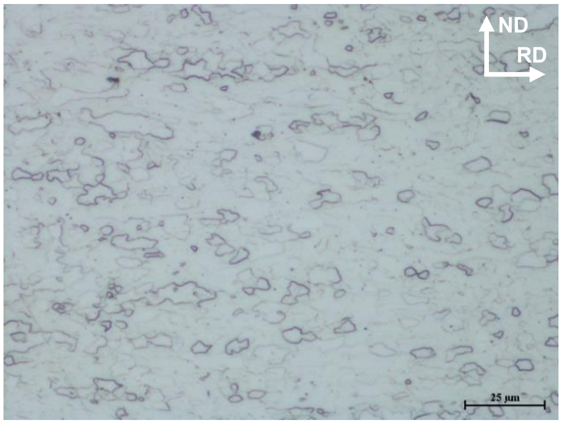

Figure 2.2.2.1.H: 700°C CP Heat Treatment at 500x Magnification

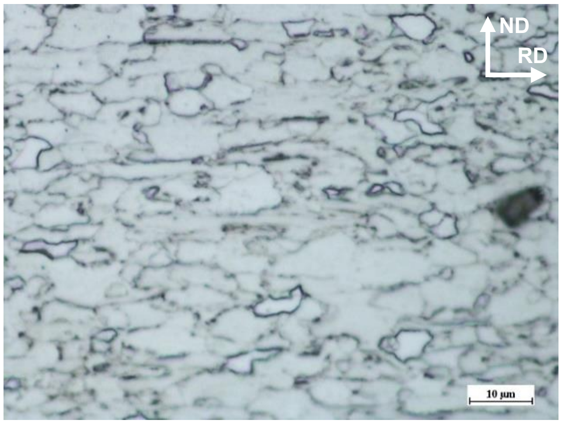

Figure 2.2.2.1.I: 650°C Heat Treatment at 1000x Magnification

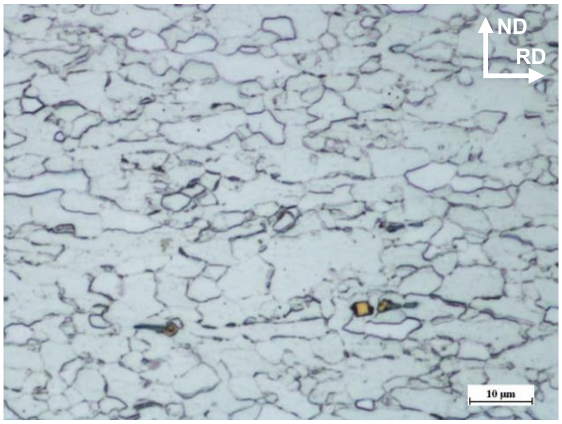

Figure 2.2.2.1.J: 680°C Heat Treatment at 1000x Magnification

One can see a square shaped gold particle in Figure 2.2.2.1.J. This is a TiN precipitate. They can become quite large – visible to optical microscopes – if sufficient Ti and N are present in the steel.

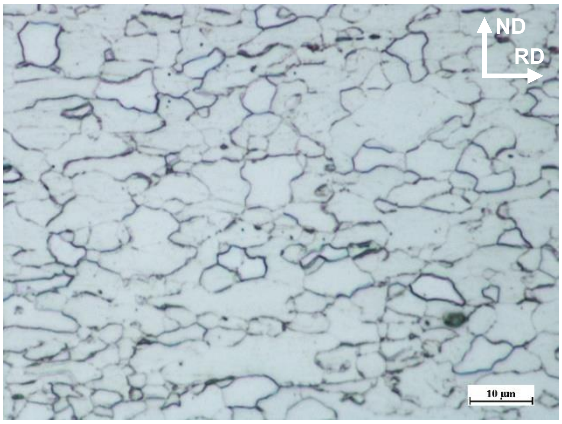

Figure 2.2.2.1.K: 700°C Heat Treatment at 1000x Magnification

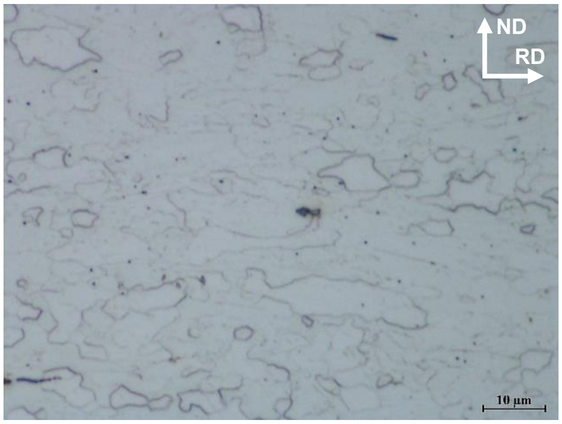

Figure 2.2.2.1.L: 700°C CP Heat Treatment at 1000x Magnification

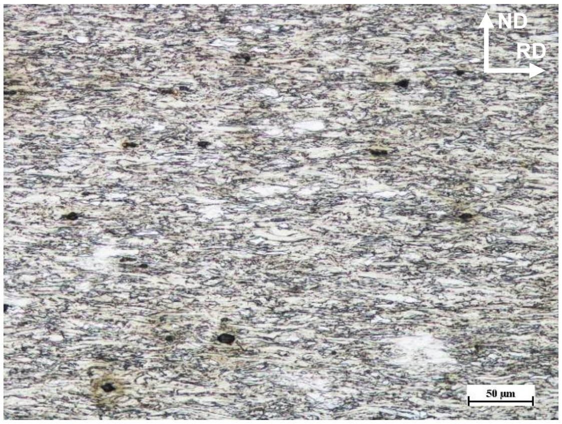

Figure 2.2.2.1.M: As Rolled State at 200x Magnification

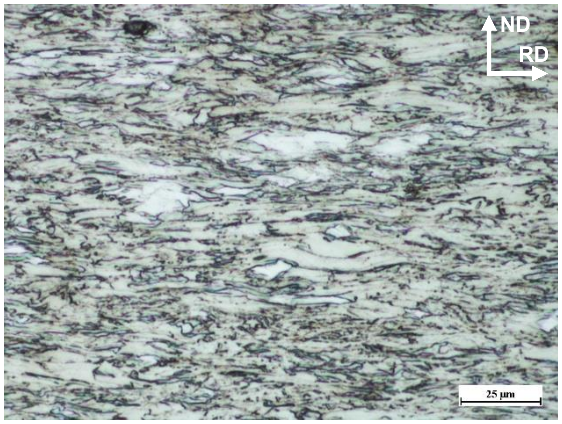

Figure 2.2.2.1.N: As Rolled State at 500x Magnification

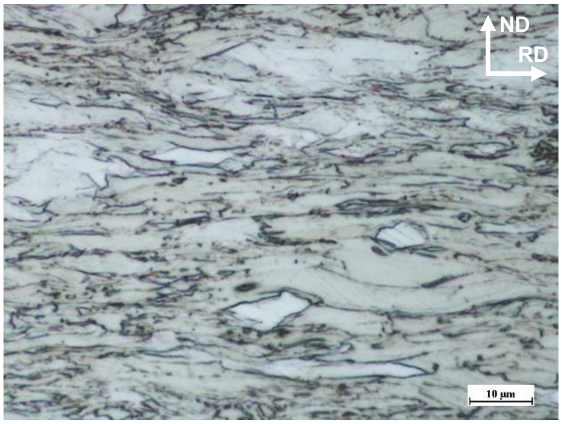

Figure 2.2.2.1.O: As Rolled State at 1000x Magnification

The as rolled state can be very clearly seen through the elongation of the grains along the rolling direction.

An important phenomenon to note is how the different annealing temperatures affect the grain shapes and sizes. At 650°C, the grains are recovered and there is still some elongation of the grains. By 700°C, the grains are almost completely recrystallized. This will be shown more analytically using EBSD in section 2.2.2.4. Another point of note is that the grain size does not change significantly at different temperatures. ImageJ is used to show this analytically. Lastly, the cold point microstructure is not fully recrystallized despite the hot point microstructure being fully recrystallized. This can be seen by some elongated grains and smaller grains in the cold point microstructure.

The grain sizes were measured using ImageJ for the various heat treatments. An example, the 650°C heat treatment, of the outlines of the measured grains is shown in Figure 2.2.2.1.P. Grain sizes smaller than 10μm^2 and larger than 500μm^2 were excluded. The parameters remained the same for the analysis of all heat treatments.

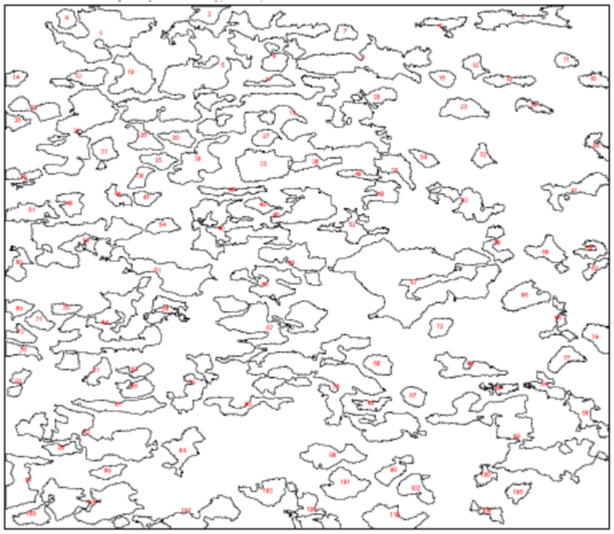

Figure 2.2.2.1.P: Grain Outlines as Found on ImageJ

For the heat treatment at 650°C, the average grain size is 41μm^2. For 680°C, the average grain size is 48μm^2. For 700, the average grain size 49μm^2. For 700°C cold point, the contrast between the grain boundaries and the grains was not high enough to make use of ImageJ, but was measured manually and is also around 50μm^2. These numbers show that grain size is roughly the same over the different heat treatments, and these findings are corroborated with the EBSD maps (section 2.2.2.4) of the grain size.

2.2.2.2 – SEM Characterization

An SEM was used to get higher magnification images of the steel to look at grains closer up and to see any finer structures, though the primary objective was to perform EBSD (section 2.2.2.4). At 5000x magnification, the grains and grain boundaries become very clear, with some fine dots being visible too.

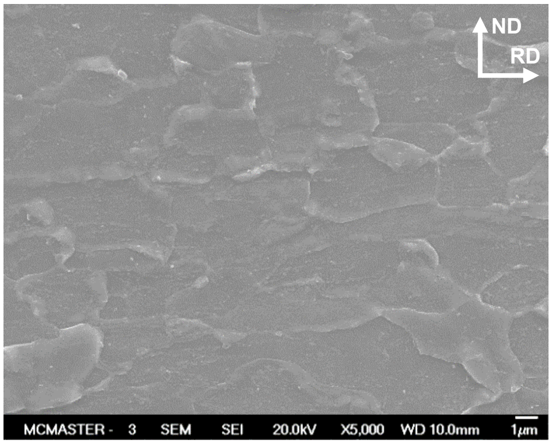

Figure 2.2.2.2.A: 650°C at 5000x in SEM

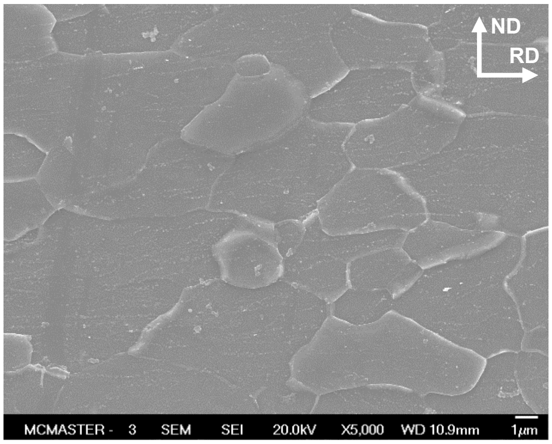

Figure 2.2.2.2.B: 680°C at 5000x in SEM

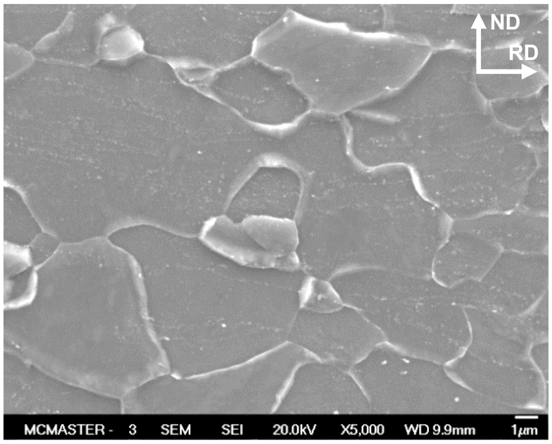

Figure 2.2.2.2.C: 700°C at 5000x in SEM

At 20,000x, small dots can be clearly seen. As they continue in straight lines across grain boundaries, they are assumed to be or subgrain boundary precipitates, possibly from the hot rolled state.

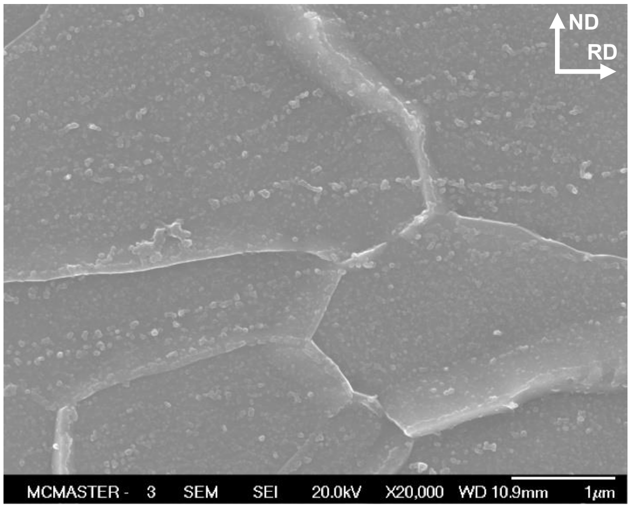

Figure 2.2.2.2.D: 680°C at 20,000x in SEM

2.2.2.3 – TEM Characterization

The TEM was used extensively to measure and observe the carbonitride precipitates, as well as their composition through the use of TEM EDS. Thin foils were used rather than extraction replicas.

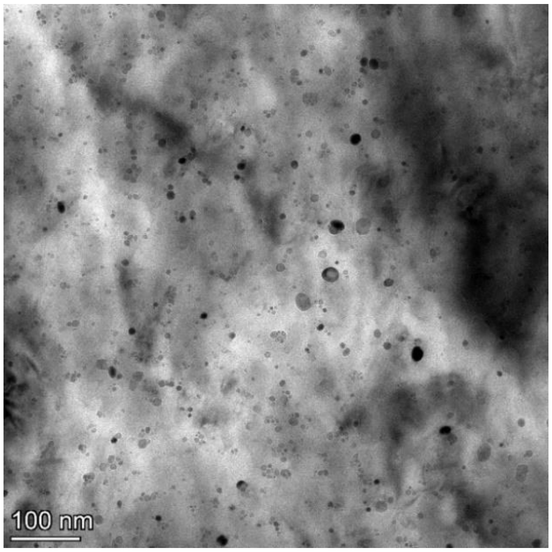

Figure 2.2.2.3.A: 650°C at 73,000x in TEM

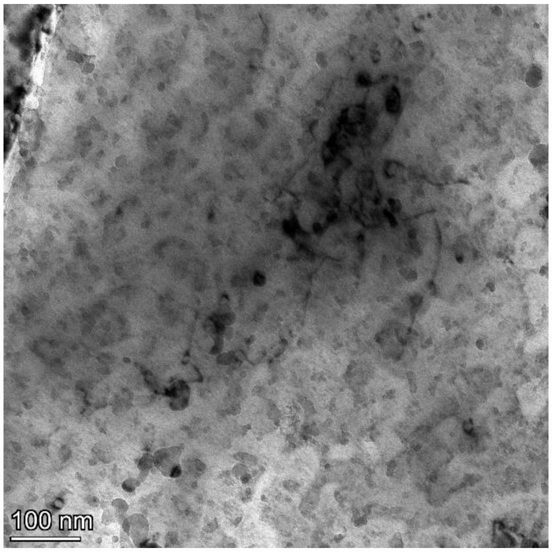

Figure 2.2.2.3.B: 700°C at 73,000x in TEM

Very high magnification images were also taken. Note the dark and spherical precipitates. Some representative images are shown below; more images in Appendix A.

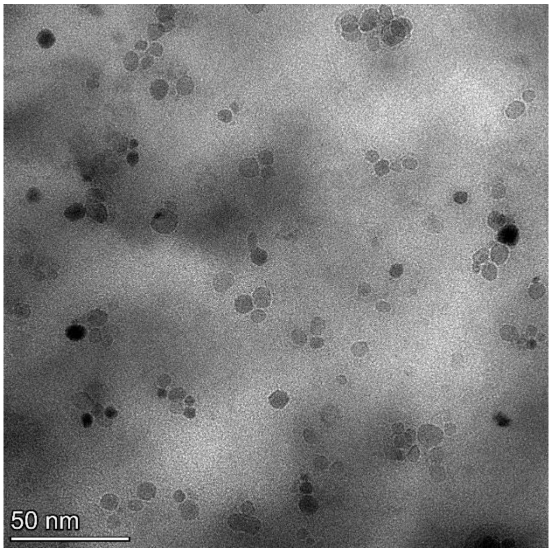

Figure 2.2.2.3.C: 650°C at 240kx in TEM

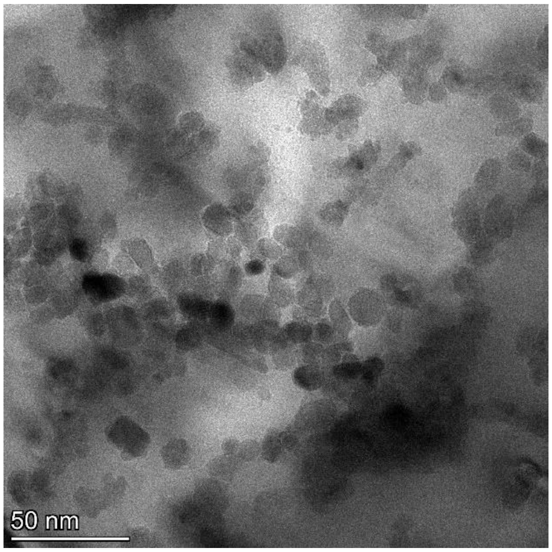

Figure 2.2.2.3.D: 700°C at 240kx in TEM

Using ImageJ, the average precipitate size for the 650°C steel was found to be 91nm^2, which, assuming spherical precipitates, is a diameter of 11nm. A histogram of precipitate size distribution is included.

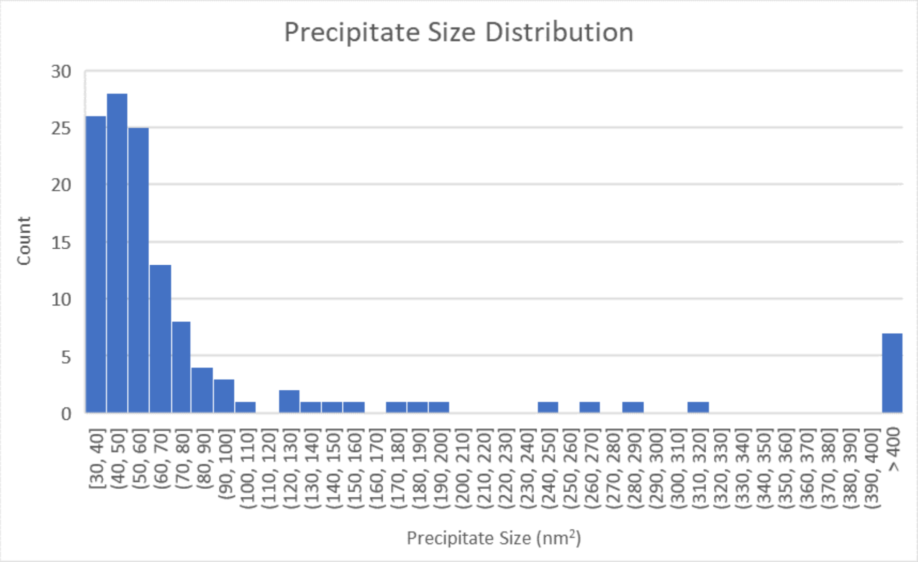

Figure 2.2.2.3.E: Histogram of Precipitate Size Distribution

Due to the spherical nature of the precipitates, as well thermodynamics calculations performed on ThermoCalc (in section 2.3.1), the precipitates are assumed to carbonitrides of the microalloying elements (V, Ti, Nb, Mo). To confirm this, TEM EDS was used to verify an increase in the concentration of the microalloying elements at the site of the precipitates. Precipitates of various sizes (5-50nm) were checked with EDS. Figure 2.2.2.3.F is a precipitate near the average precipitate size as a representative example, with more EDS maps in Appendix B.

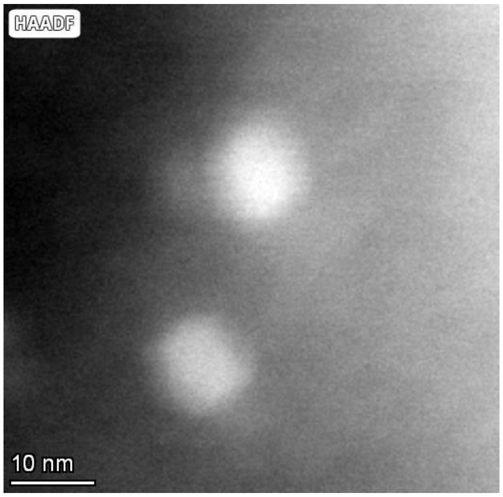

Figure 2.2.2.3.F: Precipitates Examined in EDS, 380kx Magnification

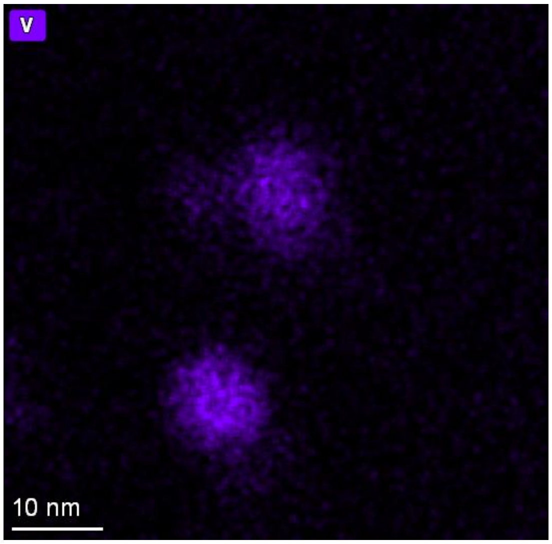

Figure 2.2.2.3.G: Vanadium EDS Map

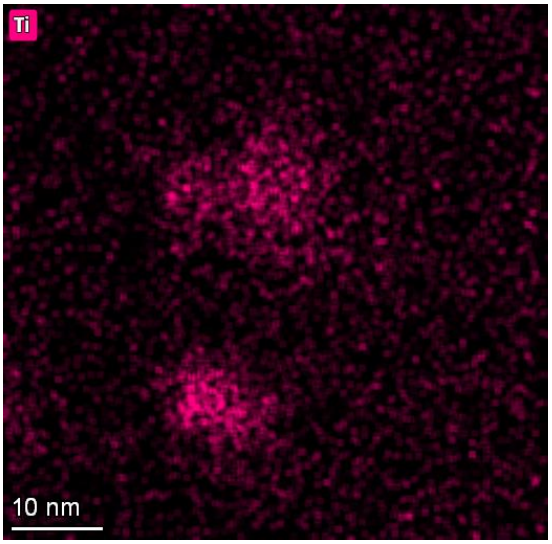

Figure 2.2.2.3.H: Titanium EDS Map

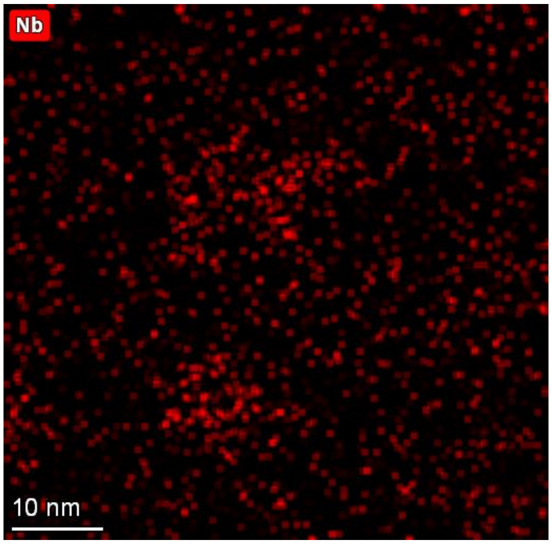

Figure 2.2.2.3.I: Niobium EDS Map

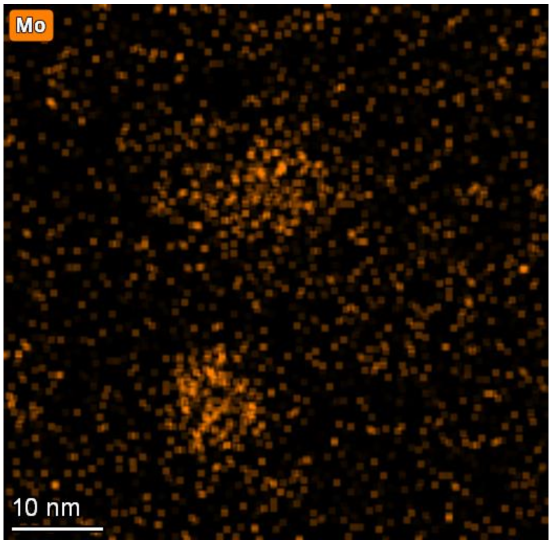

Figure 2.2.2.3.J: Molybdenum EDS Map

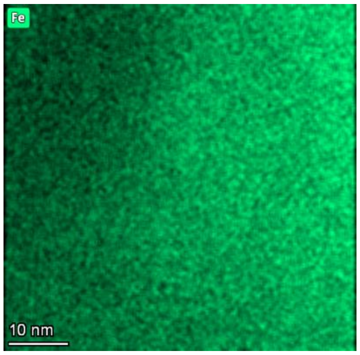

Figure 2.2.2.3.K: Iron EDS Map

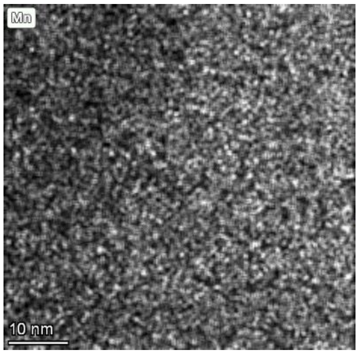

Figure 2.2.2.3.L: Manganese EDS Map

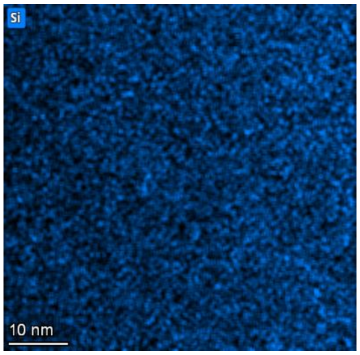

Figure 2.2.2.3.M: Silicon EDS Map

These maps show that there is a high concentration of V and Ti in the precipitates, a moderate amount of Nb and Mo, and no presence of Fe, Mn, or Si. This proves that the precipitates are in fact (V, Ti, Nb, Mo) carbonitride precipitates.

2.2.2.4 – SEM EBSD Characterization

To determine if some of the strength of the V10 steel is coming from dislocation strengthening, EBSD was performed to look for deformation in the grains. Misorientation can be used to determine the presence of geometrically necessary dislocations in the steel because dislocations are formed during cold rolling, and so exist in the steel from before the heat treatment. As such, the recovered and partially recrystallized crystals would still have some dislocations. However, the fully recrystallized state will not have dislocations as the dislocations annihilate during the recrystallization process.

Deformation is shown through misorientation maps. Specifically, kernel average misorientation (KAM) was used. In these maps, a higher value (shown as a green colouration) represents greater levels of deformation.

EBSD was performed on the 650°C, 680°C, and 700°C heat treatments. An area of 150μm×150μm was examined on each using step size of 0.15μm.

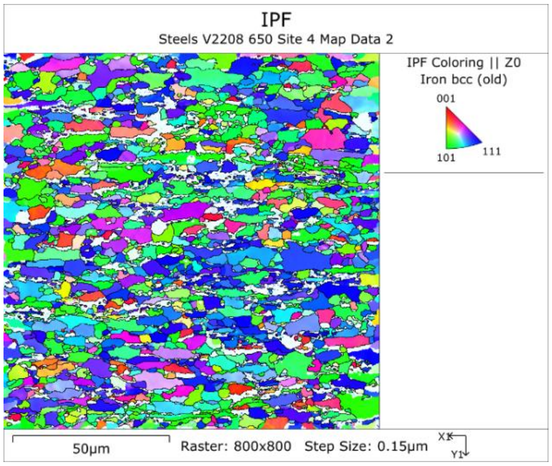

Figure 2.2.2.4.A: IPF EDS Map for 650°C

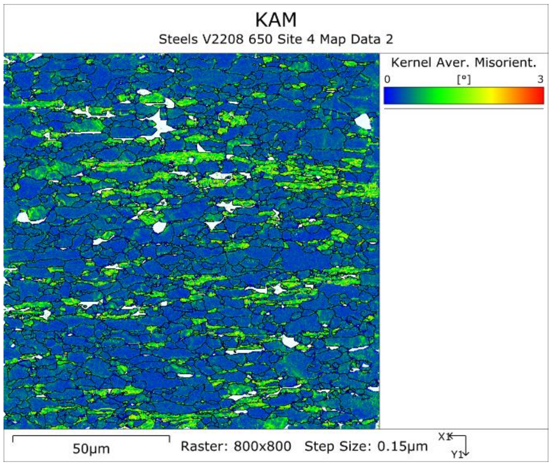

Figure 2.2.2.4.B: Misorientation Map for 650°C

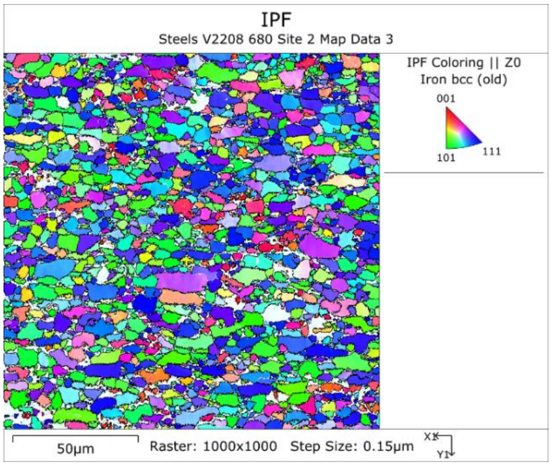

Figure 2.2.2.4.C: IPF EDS Map for 680°C

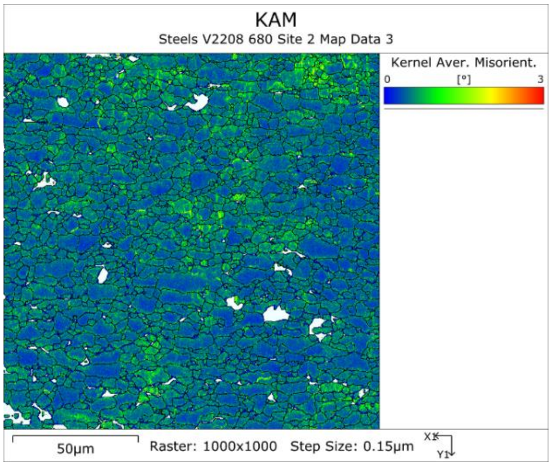

Figure 2.2.2.4.D: Misorientation Map for 680°C

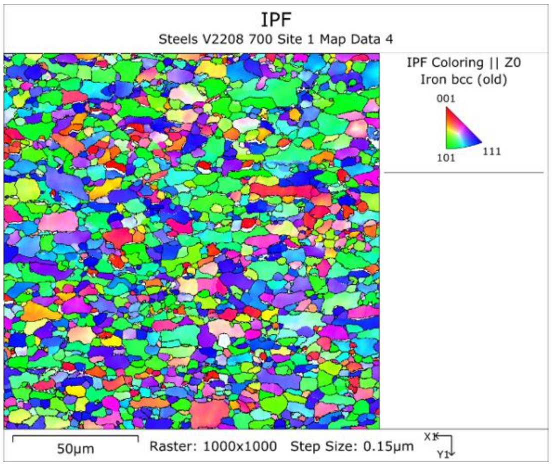

Figure 2.2.2.4.E: IPF EDS Map for 700°C

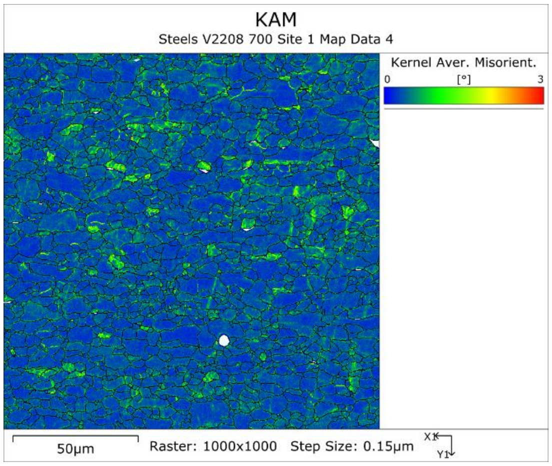

Figure 2.2.2.4.F: Misorientation Map for 700°C

From these maps, one can observe that there is less deformation at the higher heat treatments, especially at 700°C, as there is less green in the image. This is consistent with the idea of recrystallization occurring at higher temperatures and explains some of the additional strength of the 650°C sample as compared to that of the 700°C sample.

2.3 – Discussion

This section aims to explain the sources of strengthening as well as insights into the science of the steel through the use of thermodynamics simulations, microstructural characteristics, and empirical equations on the strengthening of metals. As well, this discussion explains the benefits of batch annealing over traditional annealing methods in regards to precipitation strengthened microalloyed steel.

2.3.1 – ThermoCalc Simulations

ThermoCalc 2022a was used to perform thermodynamics simulations. The *TCFE12: Steels/Fe-Alloys v12.0* package was used for the thermodynamics simulations. The composition of the steel was inputted into ThermoCalc as shown in Table 2.0.1.A, excluding sulfur as it is present only in a trace amount. The phases of graphite and Fe_2SiTi were also excluded from the simulation.

Fe_2SiTi was excluded from the simulation after performing experiments showing that it does not form, even under ideal conditions with steels containing higher amounts of Ti and Si. This experiment is included in Appendix C.

The volume fractions of the phases were modeled using a one axis equilibrium plot graphing volume fraction as a function of temperature.

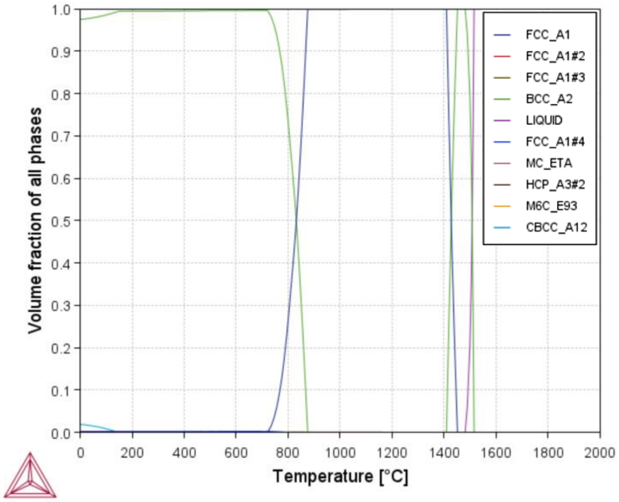

Figure 2.3.1.1.A: Volume Fraction of Phases

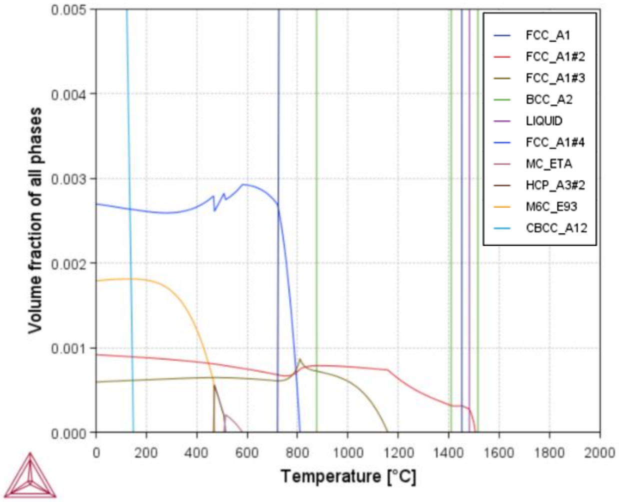

Figure 2.3.1.1.B: Volume Fraction of Phases Zoomed In

More importantly for the determination of the physical properties of the steel, the volume fractions of the precipitates were also calculated.

The phases present at room temperature are FCC_A1#2, FCC_A1#3, FCC_A1#4, and M6C_E93. Note that the CBCC_A12 phase is not present in the steel due to its low formation temperature as the kinetics for it to form at such low temperatures are simply not possible as the movement and diffusion of atoms in steel at such low temperatures is negligible. From the *TCS Steel and Fe-alloys Database*, the precipitates that are present are all carbonitrides [19]. Specifically, the FCC_A1 series precipitates are cubic carbonitrides such as Ti(C,N), Vi(C,N), Nb(C,N), etc. As shown using TEM EDS, these metals coprecipitate and thus these carbonitrides coexist. The HCP_A3#2 phase has a range of compositions, but it is primarily AlN [19]. The M6C_E93 phase is $Fe_2(Mo,Si)_2C$, but may not be present in the steel due to the temperature of formation being below 500°C. As such, this phase was excluded from the precipitate strengthening calculations.

At a temperature of 500°C (below which the diffusion is too slow to form more precipitates), the volume fractions of the precipitates are 0.0042 for the combined FCC_A1 series (as they are mixed-metal carbonitrides they are counted together) and 0.0003 for HCP_A3#2. This is a total precipitate volume fraction of 0.0045.

2.3.2 – Sources of Strength

The strength of this steel comes from the intrinsic strength of iron, the solid solution strengthening from the Mn and Si, the precipitate strengthening from the microalloy components, grain boundary strengthening, and the dislocation strengthening from the cold rolling.

The contribution to strengthening from the intrinsic strength of pure iron is given as 50MPa [11]. The contribution to strengthening from solid solution strengthening comes from the dissolved Mn and Si, which is given by their weight percentage in the steel as they are not involved in the creation of precipitates, so their weight percentage in the alloy is the same as their dissolved weight percentage in the steel. The solid solution strengthening coefficients for Mn and Si are 31 and 81, respectively. With 1.85% Mn and 0.50% Si, this results in a contribution to strengthening of 1.85×31 + 0.50×81 = 98MPa.

The precipitate strengthening is calculated using equation 1.5a with values of 0.0045 for volume fraction and an average particle diameter of 11nm (as found in section 2.2.2.3), which results in an increase of strength of 132MPa.

Lastly, there is grain boundary strengthening. Using a k_y of 550MPa*m$^{1/2}$ and an average grain length of 7μm (as found in section 2.2.2.1) results in an additional 208MPa.

Summing these values gives an estimated yield strength of 488MPa. This closely matches the value of yield strength measured empirically for the steel annealed at 700°C of 456MPa, which shows the validity of using these equations for predicting the yield strength.

2.3.2.1 – Recovery and Recrystallization

As seen in the KAM maps, there is some misorientation within the grains, especially at lower annealing temperatures. This corresponds to a microstructure that is still partially recovered and not completely recrystallized, and has some dislocations present. These dislocations strengthen the steel through dislocation strengthening, as can be seen by the steels annealed at lower temperatures having a higher yield strength. While some of this strength comes from finer precipitates, some comes from the dislocations within the recovered microstructure. The properties and kinetics of recovery annealed steels will be explored in greater depth in section 3.3.2.

2.3.3 – Grain Growth

A very interesting result in this steel is how the grain size only increased slightly with annealing temperature as shown in the optical micrographs and calculated using ImageJ. This is presumed to be from the high volume-fraction of precipitates contributing substantially to Zener pinning, which impedes grain growth. As shown in section 2.2.2.3, the precipitates do coarsen somewhat at higher temperatures, which would explain the small increase in grain size.

2.3.4 – Precipitate Growth

At higher temperature heat treatments, the precipitates in the steel also grow due to increased diffusion kinetics at higher temperatures. The precipitate growth can be determined for different times and temperatures. An example for a niobium microalloyed steel (Nb = 0.079%, C = 0.011%) is included in Figure 2.3.4.A, showing that at the temperatures and annealing times used for the V10 steel, precipitate growth can go to completion or near thereto [49]. Furthermore, the lower temperatures encourage finer precipitates to grow, which is an advantage of batch annealing over traditional annealing techniques [49].

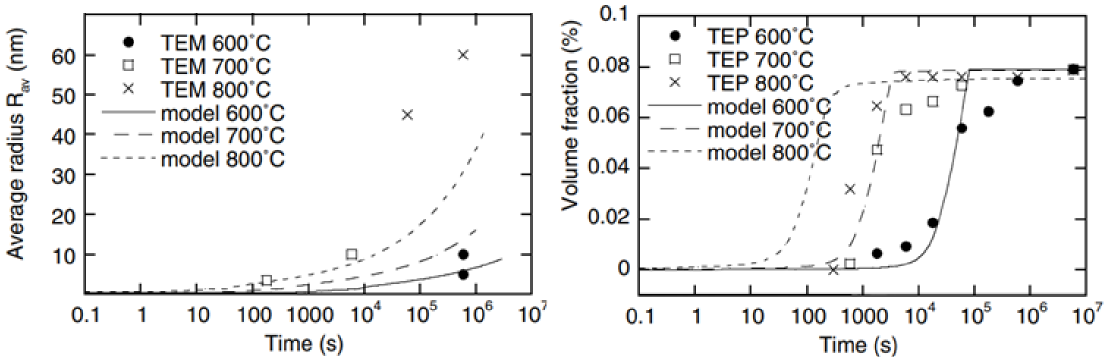

Figure 2.3.4.A: Evolution of Niobium Carbide Precipitates in a Ferritic Steel [49]

Figure 2.3.4.A also matches the observations seen in the TEM, with the sample annealed at 700°C having larger precipitates that the sample annealed at 650°C. The size of the precipitates is crucial as larger (and thus fewer numbers of) precipitates not only reduce the extent of precipitation strengthening, but also allow grain growth due to less Zener pinning, which means that larger precipitates weaken the steel by two mechanisms.

2.3.5 – Agreement With Literature

Overall, the V10 steel behaves as expected given the literature on ferrous metals and HSLA steels specifically in regard to its mechanical properties, microstructure, and behaviour. A stress-strain curve for HSLA 350/450 steel, Figure 2.3.5.A, is shown and the curve is very similar to the ones for the V10 steel with the upper yield point, some amount of ludering, and then work hardening before failure shortly after necking [50].

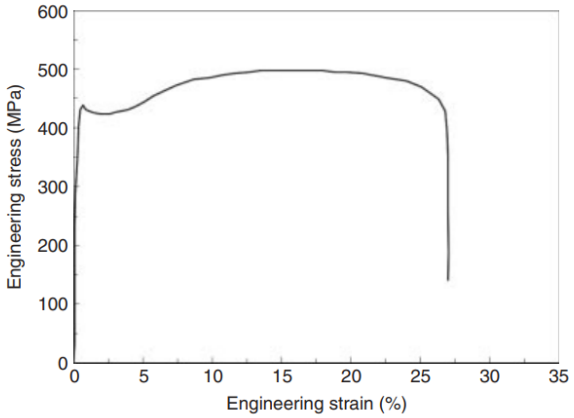

Figure 2.3.5.A: Stress-Strain Curve for HSLA 350/450 Steel [50]

The key difference and novelty between the V10 steel and preexisting HSLA steels is that the V10 steel achieves a higher yield strength than many commercially available grades, as can be seen by the much lower yield point on the stress strain curve in Figure 2.3.5.A [50].

Likewise, the microstructure of the V10 steel matches closely with the literature. An example micrograph from another HSLA steel is shown on the following page, and clear similarities can be seen [50].

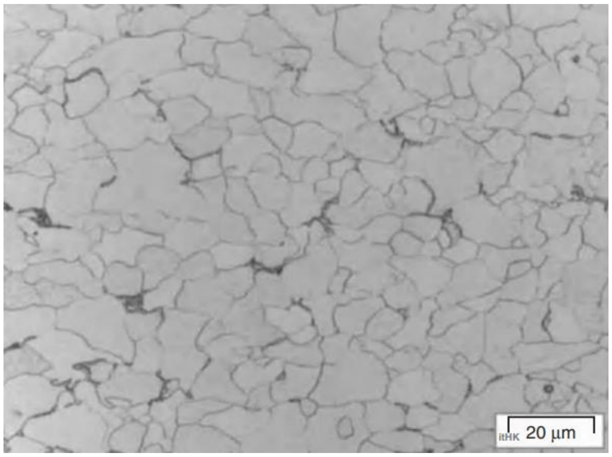

Figure 2.3.5.B: Microstructure of an Example HSLA Steel [50]

2.3.6 – Comparison with Targets

The mechanical property targets for the automotive steel were achieved, albeit marginally and not statistically significantly. The ± represents a 90% confidence interval.

Table 2.3.6.A: Comparison of V10 Steel with Target Specifications

Property	**Target**	**V10 680°C**
Yield Strength (MPa)	500<	511 ± 38
Tensile Strength (MPa)	560<	602 ± 28
Elongation at Fracture (%)	16<	16.7 ± 1.9

Given the natural variability in manufacturing and processing and, these properties are too close to the targets to be confident that the steel would consistently meet specifications. However, for other applications that are slightly less demanding, such as Grade 70 steel, the V10 steel would be a viable option.

Section 3 – Recovery-Annealed HSLA Steel

3.0 – Alloy and Process Design

The composition and processing parameters were chosen to create a Grade 80 steel with good ductility. A large part of the strengthening comes from dislocation strengthening by means of a recovered microstructure. This was achieved through a recovery-annealing heat treatment which maintains much of the strength of the cold worked material while substantially increasing its ductility; this mechanism is explained in greater detail in section 3.3.2. This recovery-annealed HSLA steel will be referred to as V20 throughout the rest of the thesis.

3.0.1 – Alloy Design

The chemistry of the steel was chosen specifically to make a recovered microstructure. This was done by relatively large additions of titanium, as Ti slows the recrystallization kinetics in steel [41]. Furthermore, manganese and silicon were added primarily for their contribution to solid solution strengthening.

Two nearly identical chemistries were made, with the only nonnegligible difference being the titanium content. This is to observe the effect of Ti concentration on recrystallization. The target Ti concentrations are 0.2wt.% and 0.4wt.%. While the measured values of Ti vary slightly from the target, the two chemistries will be called V20 0.2%Ti (actual 0.19%Ti) and V20 0.4%Ti (actual 0.35%Ti), respectively. The chemistries are shown in Table 3.0.1.A:

Table 3.0.1.A: Chemistry of the V20 0.2%Ti Steel

Fe	C	Mn + Si	Ti	Al	S	O	N
Bal	0.025	2.60 – 2.70	<0.20%	0.020	0.002	0.003	0.002

Table 3.0.1.B: Chemistry of the V20 0.4%Ti Steel

Fe	C	Mn + Si	Si	Ti	Al	S	O	N
Bal	0.025	2.60 – 2.70	0.93	<0.40%	0.019	0.002	0.003	0.003

The different alloying additions were chosen for various reasons. Firstly, the large titanium additions are to slow the recrystallization in the steel [41]. Nb is also known to have this effect, but Ti is more economical [41]. This allows for a recovered microstructure to occur after processing, which, due to the large amount of residual dislocations, is quite strong [41].

Carbon is included as it is crucial to practically all steels. However, this steel is designed to be strengthened primarily by dislocation strengthening and not precipitates. As such, the level of carbon is quite low. Keeping the concentration of carbon low is done for two reasons. Firstly, carbon reduces the weldability of steel, which is a secondary design requirement of the steel [51]. Secondly, carbon preferentially combines with titanium to form TiC precipitates, which would lower the concentration of Ti within the matrix, reducing the effect Ti has on slowing recrystallization.

As previously mentioned, both silicon and manganese are added to the V20 steel to strengthen it through solid solution strengthening [2]. Manganese and silicon are somewhat unique in that their inclusion at these concentrations does not significantly affect or worsen the ductility of the steel; in fact, Mn often decreases the brittleness of the steel [2]. The limiting factor for the concentration of silicon was actually the difficulty it causes in casting due to its reaction with oxygen. The furnaces of the industry partner for which this research is being conducted have a casting limit of 1.0wt.% Si, and so the concentration of silicon in the steel was kept slightly below this threshold. Note that many steels, especially electrical steels, have much higher Si concentrations of up to 3.5%, though these high percentages can affect the ferrite concentration [52].

The small amount of aluminum in the steel is to help kill the steel and maintain a low oxygen concentration [53]. As oxygen can embrittle steel, the addition of Al was purposeful.

All other elements in the steel (namely S, O, and N) are impurities that are almost inevitable to be present in small concentrations. A particularly detrimental impurity is nitrogen as it forms titanium nitride with the titanium present in the steel. TiN forms at very high temperatures and even exists while the steel is molten, which can result in cubes of TiN in the steel which may be detrimental to the mechanical properties if the TiN precipitates are of a sufficiently large size.

3.0.2 – Process Design

The process design for the V20 steels includes both the mechanical processing and the annealing. Mechanical processing was done in following a standard procedure proposed by CanmetMATERIALS and is similar to the mechanical processing of the V10 steel. This was purposefully chosen as we know this procedure works well for microalloyed steels. Specifically, the high finishing temperature and low coiling temperature help keep more Ti in solution. The full steps of the mechanical processing (hot rolling, coiling, and cold rolling) will be discussed in the next section, section 3.1.

The heat treatment for the V20 steel was performed at a wide range of temperatures, from 525°C to 700°C. These temperatures were chosen because recrystallization was expected to occur between these temperatures based off data from other microalloyed steels, including V10. Therefore, by choosing a temperature slightly lower than the recrystallization temperature, a recovered microstructure could be achieved.

3.1 – Experimental Methods

This section on experimental methods outlines all of the procedures that were employed, including hot rolling, cold rolling, heat treatments, tensile testing, and sample preparation for both optical and electron microscopy. The processing steps for both the 0.2%Ti steel and the 0.4%Ti steel were identical and often occurred simultaneously.

3.1.1 – Hot Rolling

The ingots were first heated to 1260°C for three hours before being hot rolled on CanmetMATERIALS's pilot mill to a 97% reduction over a series of 9 passes. The starting thickness was 130mm, and the final thickness 3.7mm. After rolling, the temperature of the sheets was 900°C and the sheets were then cooled quickly to 680°C. Lastly, they were coiled at 80meters/min at 650°C and kept at 650°C for 2 hours.

3.1.2 – Cold Rolling

The sheets were cold rolled at McMaster on a separate mill. They were first sectioned to be able to fit into the smaller mill, before being cold rolled. The thickness was reduced by 60%, from 3.7mm to a 1.48mm over a series of many passes. Each pass reduced the thickness by 0.15875mm (1/160").

3.1.3 – Cutting of Tensile Test Bars

There were two types of tensile samples that were manufactured, subsize and full-size. Unless otherwise stated, the results of the tensile tests use the subsize bars.

The subsize tensile samples were cut from the sheet metal using a CNC machine. They were cut such that the rolling direction is parallel with the direction of the force applied during tensile testing; that is, the rolling direction is along the length of the specimen.

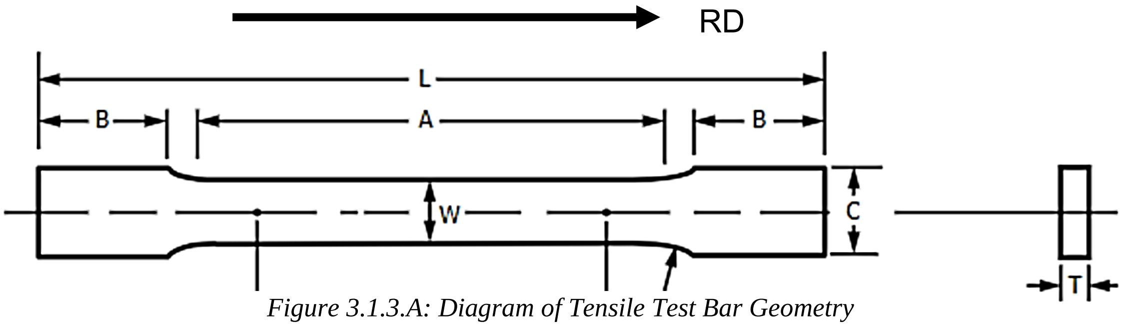

Figure 3.1.3.A: Diagram of Tensile Test Bar Geometry

Table 3.1.3.A: Dimensions for Subsize Tensile Test Bar in mm

G	W	T	R	L	A	B	C
25.4	6.35	1.48	2	50.8	30 (min)	15 (min)	10

The full-size tensile samples were also cut from the sheet metal using a CNC machine. Two of the samples were cut such that their rolling direction is parallel with the direction of the force applied during tensile testing; that is, the rolling direction is along the length of the specimen. Two more were cut with the rolling direction transverse to the direction of applied force. This was done to quantify any anisotropy present in the sample. Furthermore, larger samples were tested to ensure that the mechanical properties are maintained at different scales. The results of these tests are in section 3.2.1.

Table 3.1.3.B: Dimensions for Full-Size Tensile Test Bar in mm

G	W	T	R	L	A	B	C
50	12.7	1.25	12.5	200	65 (min)	50 (min)	20

3.1.4 – Heat Treatments

The heat treatments were performed in a tube furnace under an inert argon atmosphere. The heating rate, soak time, and cooling rate were chosen to emulate the characteristics of a batch annealing furnace. The heat treatment was as follows: heat at +60°C/h from room temperature to the target temperature, hold for 24 or 36 hours at the target temperature, and cool at -30°C/hour back to room temperature. Unless otherwise stated, the soak time is 24 hours.

3.1.5 –Microscopy Sample Preparation

The samples for optical microscopy were prepared as written in section 2.1.6. The samples for the SEM were prepared as written in section 2.1.7. The JOEL 7000 was used for both SEM and SEM EBSD. EBSD sample preparation follows the procedure detailed in section 2.1.7.1. For TEM and EELS, thin foils were prepared. Their preparation follows the same procedure as in section 2.1.8, but with a different electropolishing bath. The electropolishing was performed in a solution of glacial acetic acid with 5% perchloric acid using a voltage of 22V and at a temperature of 15°C.

3.1.6 – APT Sample Preparation

APT liftouts were created from a sample prepared for the SEM using a gallium FIB. These tips were then checked in the TEM to ensure that the targeted features are included. These were then inserted into the Cameca LEAP 5000 XS Atom Probe Tomograph for APT imaging.

3.2 – Results

This section includes the results of all experiments performed, including tensile testing, SEM, EBSD, TEM, EDS, and APT. These sections aim to cover mechanical properties and microstructural characterization.

3.2.1 – Mechanical Properties

Uniaxial tensile testing was used to determine the mechanical properties of the steel. The crosshead speed was 2mm/min and the extensometer gauge length was 25.4mm for the subsize bars and 50mm for the larger bars. From these curves, the yield strength was determined using the 0.2% offset method and the tensile strength from the maximum force applied. The ductility is measured using percent elongation at fracture. Unless otherwise specified, the mechanical properties are from the subsize tensile tests. The results are on the following two pages.

Please note that the ± values refer to a 90% confidence interval and are calculated using a t-test with a t-value of 6.314. 90% was chosen rather than 95% as only duplicates were performed, so the 95% confidence interval would be too large to be meaningful due to the large t-value associated with only having two data points. With a third test, these values could be reduced substantially. Also, due to the more random nature of elongation at fracture, care should be used when interpreting their confidence intervals. Lastly, for the samples which were only tested once, no statistical analysis was performed as a minimum of two data points are required.

Table 3.2.1.A: Mechanical Properties of the V20 0.2%Ti Steel for Different Heat Treatments

	YS 0.2% (MPa)	**UTS (MPa)**	**% El. (25.4mm Gauge)**
525°C 36h 1	671	723	16.3
525°C 36h 2	661	714	15.8
525°C 36h AVG	666 ± 32	718 ± 28	16 ± 1.6
550°C 36h 1	610	686	19.7
550°C 36h 2	603	673	19.2
550°C 36h AVG	606 ± 22	680 ± 41	19.4 ± 1.6
550°C 24h 1	643	707	15.7
550°C 24h 2	635	699	18.6
550°C 24h AVG	639 ± 25	703 ± 25	17.1 ± 9.2
575°C 24h 1	461	598	25.2
575°C 24h 2	480	609	25.2
575°C 24h AVG	470 ± 60	603 ± 35	25.2 ± 0.0
600°C 24h	364	535	34.8
650°C 24h	370	520	33.8
700°C 24h	346	509	33.7
Hot Rolled	364	531	43.2
Cold Rolled	862	887	1.8

Table 3.2.1.B: Mechanical Properties of the V20 0.4%Ti Steel for Different Heat Treatments

	YS 0.2% (MPa)	UTS (MPa)	% El. (25.4mm Gauge)
525°C 36h	708	766	14.0
550°C 36h	646	706	16.7
550°C 24h 1	656	711	16.4
550°C 24h 2	659	716	15.0
550°C 24h AVG	658 ± 9	713 ± 16	15.7 ± 4.4
575°C 24h 1	593	666	17.7
575°C 24h 2	611	682	20.7
575°C 24h AVG	602 ± 57	674 ± 51	19.2 ± 9.5
600°C 24h	485	612	25.0
650°C 24h	377	540	32.6
700°C 24h	362	517	31.0
Hot Rolled	380	550	35.8

The mechanical tests performed show a strong correlation between annealing temperature and the mechanical properties below the temperature at which the steel is fully recrystalized. Above this temperature, properties remain fairly constant. The recrystallization temperature is the temperature at which all or almost all of the deformed structure has been replaced with recrystallized grains, and is shown by the temperature above which ductility does not change meaningfully. For the 0.2%Ti steel, the recrystallization temperature is around 600°C; for the 0.4%Ti steel the recrystallization temperature is around 650°C. These temperatures are confirmed using EBSD and misorientation maps in section 3.2.2.4.

One data point that stands out is the cold rolled properties. The strength is high, but the ductility is extremely poor, with an elongation at fracture of less than 2%. This shows the need for annealing and proves that annealing at temperatures below the recrystallization temperature does still significantly affect ductility.

Excluding that outlying data point, and assuming a linear relationship between strength or ductility and annealing temperature (up to the recrystallization temperature), we can estimate the yield strength and ductility at different temperatures within the studied temperatures, and can extrapolate properties for temperatures outside this range.

From Figure 3.2.1.A, for every 1°C increase in annealing temperature, a decrease to the yield strength of 5.7MPa is expected for heat treatments with a soak time of 24 hours for temperatures between 550°C and 600°C. These are temperatures at which recrystallization begins to occur for this steel.

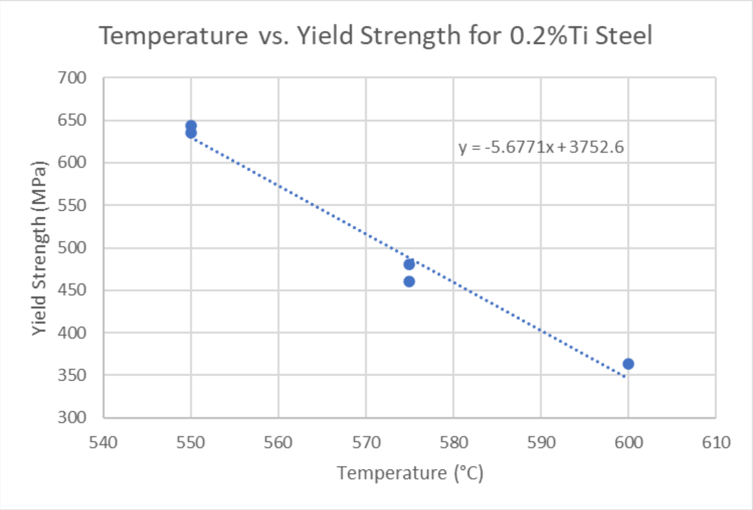

Figure 3.2.1.A: Effect of Temperature on Yield Strength for 0.2%Ti Steel for 24h Heat Treatments

At the same time, Fig. 3.2.1B shows that for every 1°C increase in annealing temperature, an increase to the elongation at fracture of 0.35% is expected for heat treatments with a soak time of 24 hours temperatures between 550°C and 600°C.

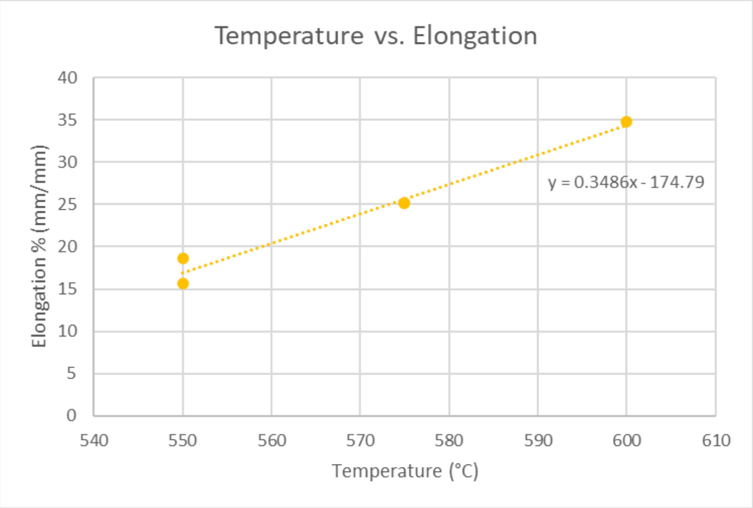

Figure 3.2.1.B: Effect of Temperature on % El. at Fracture for 0.2%Ti Steel for 24h Heat Treatments

The same approach can be used to determine properties of the heat treatments with soak times of 36 hours. This graph shows that the properties change less quickly below 550°C as the slope of the line is much shallower, at only -2.4MPa/°C. This is to be expected as kinetics occur faster at higher temperatures, and the amount of recrystallization increases exponentially as the recrystallization temperature is reached.

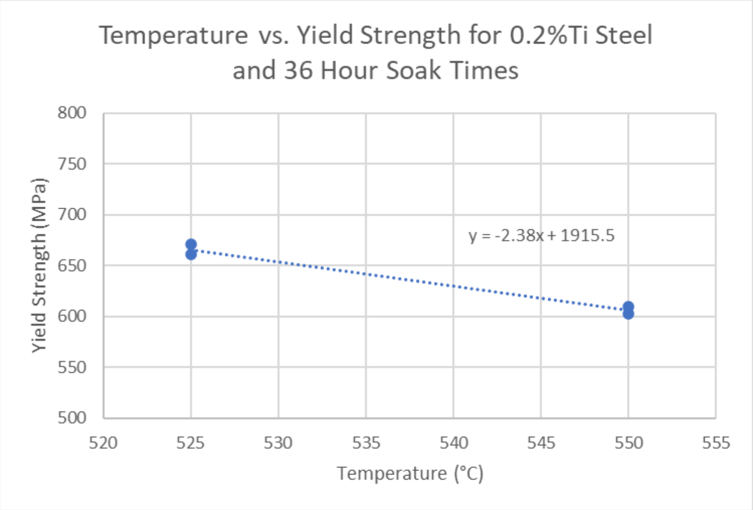

Figure 3.2.1.C: Effect of Temperature on Yield Strength for 0.2%Ti Steel for 36h Heat Treatments

Similarly, the increase in ductility due to increasing annealing temperature at temperatures below 550°C is also reduced. Nonetheless, the trend is still apparent for every 1°C increase in annealing temperature, an increase to the elongation at fracture of 0.14% is expected for heat treatments with a soak time of 36 hours at temperatures between 525°C and 550°C.

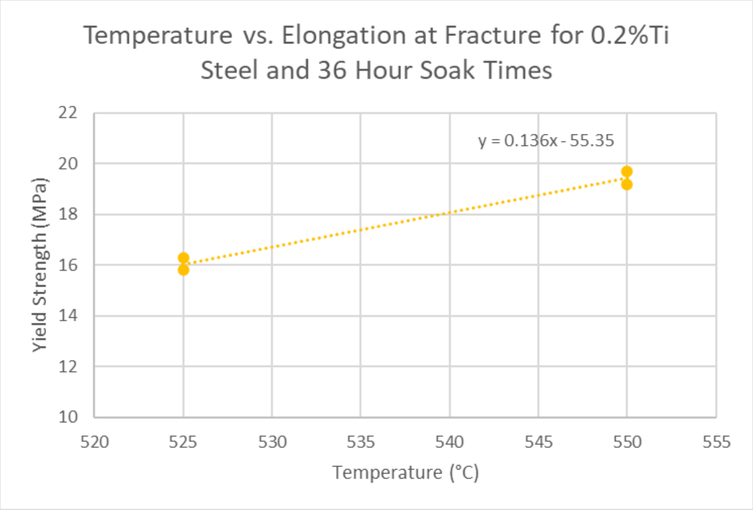

Figure 3.2.1.D: Effect of Temperature on %El. at Fracture for 0.2%Ti Steel for 36h Heat Treatments

The same process is done for the 0.4%Ti Steel. For the 24 hour soak time and for temperatures between 550°C and 650°C (the recrystallization temperature), every 1°C increase in temperature results in a decrease of yield strength by 2.9MPa and results in an increase of ductility of 0.17% elongation at fracture. For the 36 hour soak time and for temperatures between 525°C and 550°C, every 1°C increase in temperature results in a decrease of yield strength by 2.5MPa and results in an increase of ductility of 0.10% elongation at fracture.

Testing involved 17 different heat treatment and chemistry combinations and dozens of individual tests. A stress-strain curve from each heat treatment is shown in Figure 3.2.1.E. Unless otherwise specified, the soak time is assumed to be 24 hours.

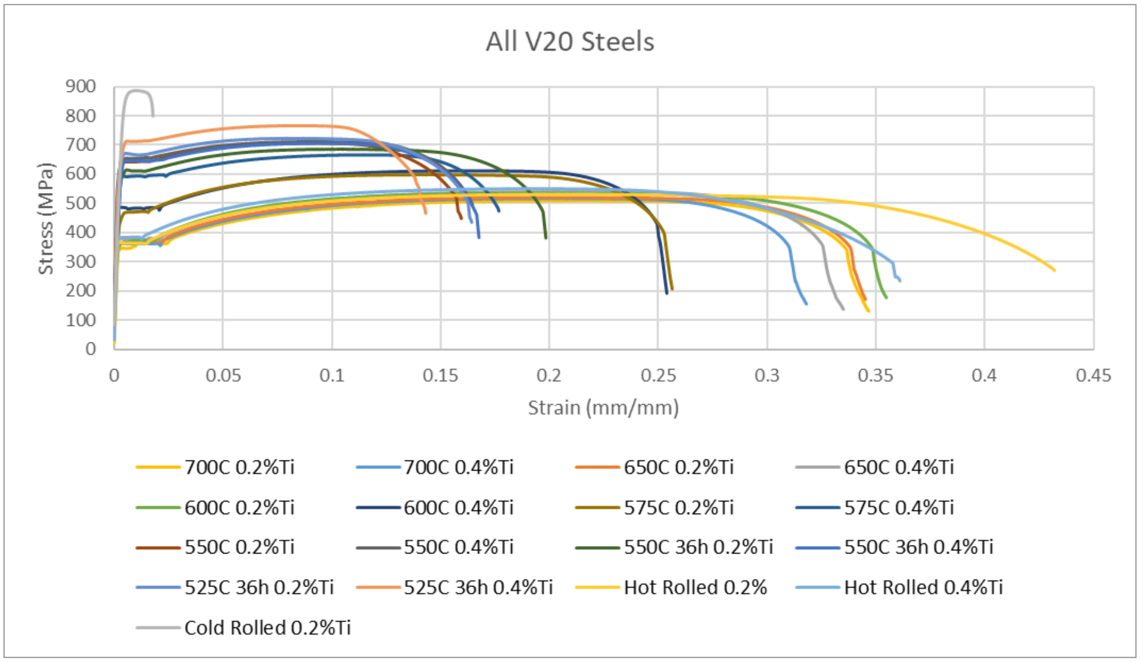

Figure 3.2.1.E: Stress-Strain Curves for All Tested V20 Heat Treatments and Chemistries

The steels with the best properties (closest to target) are selected and shown in Figure 3.2.1.F. These steels are all the heat treatments from 525°C to 600°C for both 0.2%Ti and 0.4% Ti steels.

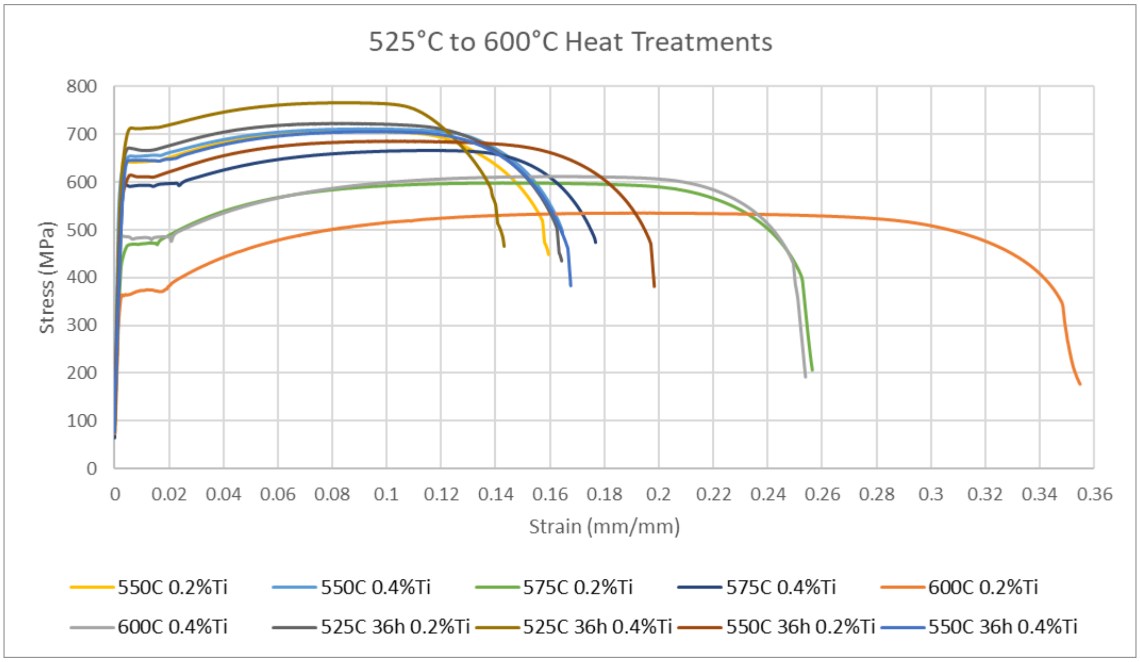

Figure 3.2.1.F: Stress-Strain Curves for V20 Heat Treatments Between 525°C and 600°C

The heat treatments between 525°C and 575°C for the 0.2%Ti steel are also highlighted, as this temperature range shows the best mechanical properties and the 0.2%Ti chemistry is easier to cast and is cheaper to manufacture, so it is of greater commercial interest.

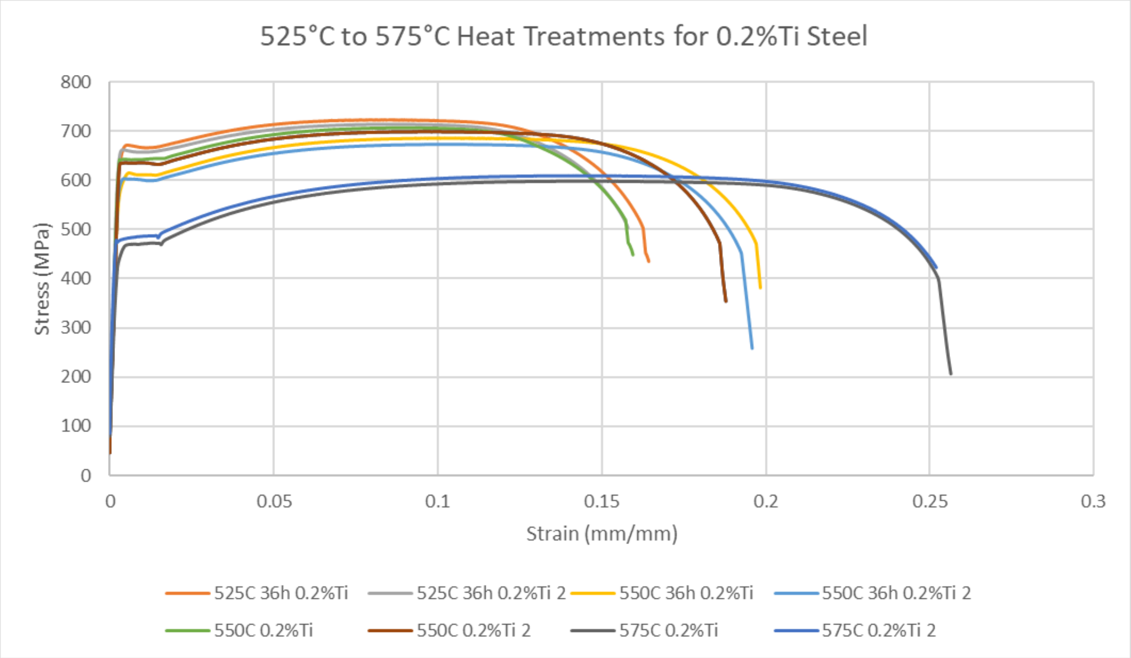

Figure 3.2.1.G: Stress-Strain Curves for 0.2%Ti V20 Heat Treatments Between 525°C and 575°C

Of all the heat treatments, the most successful were the heat treatments with a 36 hour soak time, and especially the one performed at 550°C. The results of those specific tests are shown in Figure 3.2.1.H.

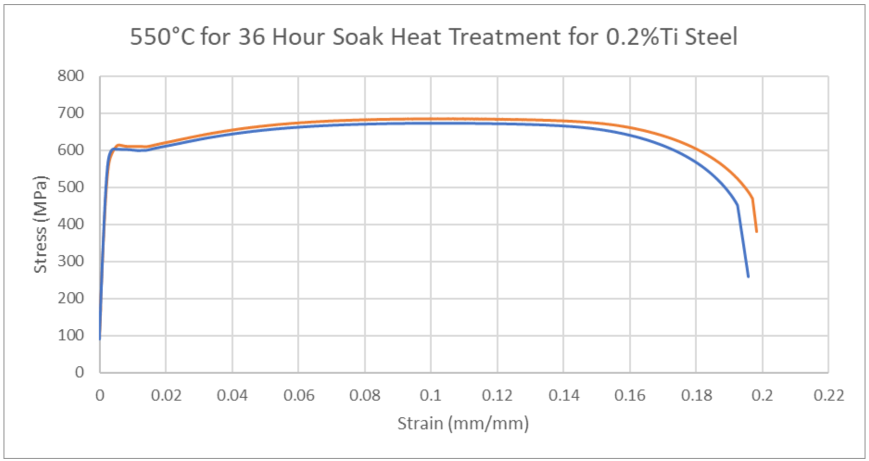

Figure 3.2.1.H: Stress-Strain Curves for 0.2%Ti V20 Steel With a 36 Hour Soak at 550°C

3.2.1.1 – Large Tensile Tests

In addition to the extensive testing of subsize tensile bars, tensile tests on large bars were also conducted. Larger tensile tests typically show reduced elongation at fracture, which is the case in these tests too. One of these bars was machined parallel to the rolling to direction and one transverse to the rolling direction. This was performed for the 0.2%Ti steel heat with a 36 hour soak time at 550°C. The results show some isotropy, which is to be expected as samples cut transversely to the rolling direction are less ductile.

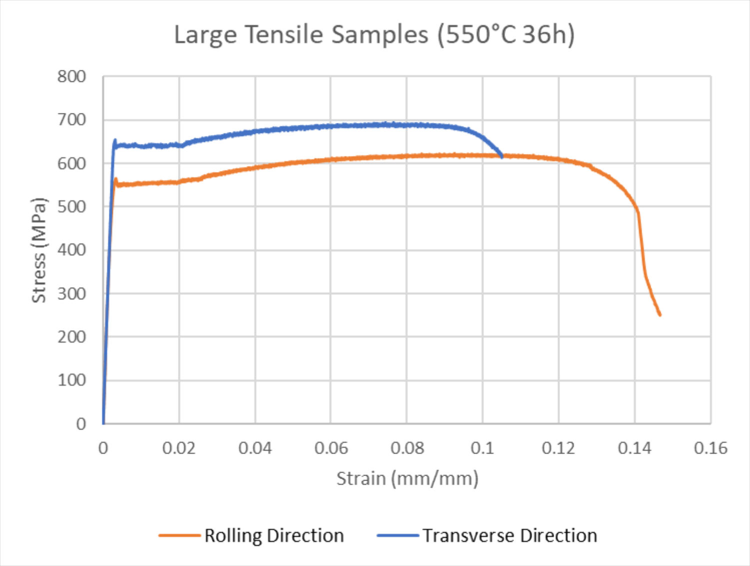

Figure 3.2.1.1.A: Stress-Strain Curves for Large Tensile Tests in the Rolling and Transverse Directions for 0.2%Ti V20 Steel With a 36 Hour Soak at 550°C

From these curves, we can determine the yield strength, tensile strength, and percent elongation at fracture, which is summarized in Table 3.2.1.1.A.

Table 3.2.1.1.A: Mechanical Properties of the Large Tensile Samples

	YS 0.2% (MPa)	**UTS (MPa)**	**% El. (50mm Gauge)**
Rolling Direction	551	623	14.1
Transverse Direction	640	694	10.5

This level of anisotropy is higher than ideal, and does make the ductility low in the transverse direction.

3.2.2 – Microstructural Characterization

The microstructure of the steel was verified using optical microscopy, SEM, TEM, EBSD, EDS, and APT.

3.2.2.1 – Optical Microscopy

Optical micrographs were taken at mid-thickness for both the 0.2%Ti and 0.4%Ti samples. The heat treatments observed were those with 24 hour soak times at temperatures of 550°C, 575°C, 600°C, 650°C, and 700°C, as well as the cold rolled state. Representative micrographs at 200x and 500x magnifications for the various heat treatments are shown over the next several pages.

Figure 3.2.2.1.A: 550°C Heat Treatment at 200x Magnification for 0.2%Ti Steel

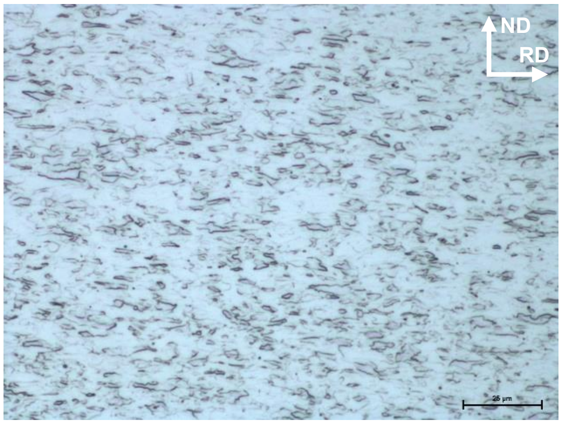

Figure 3.2.2.1.B: 550°C Heat Treatment at 500x Magnification for 0.2%Ti Steel

Figure 3.2.2.1.C: 550°C Heat Treatment at 200x Magnification for 0.4%Ti Steel

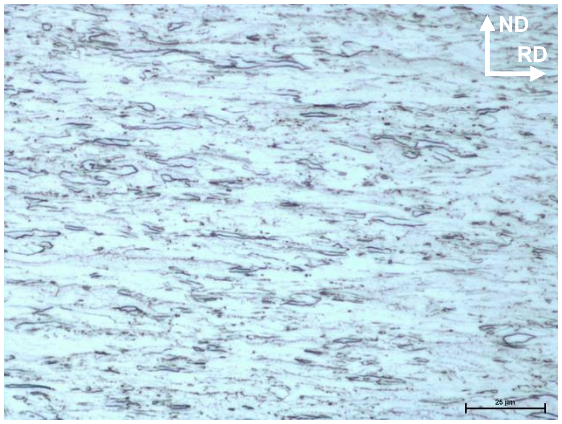

Figure 3.2.2.1.D: 550°C Heat Treatment at 500x Magnification for 0.4%Ti Steel

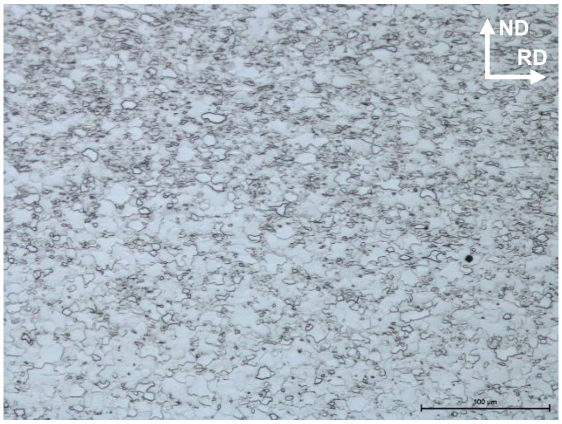

Figure 3.2.2.1.E: 575°C Heat Treatment at 200x Magnification for 0.2%Ti Steel

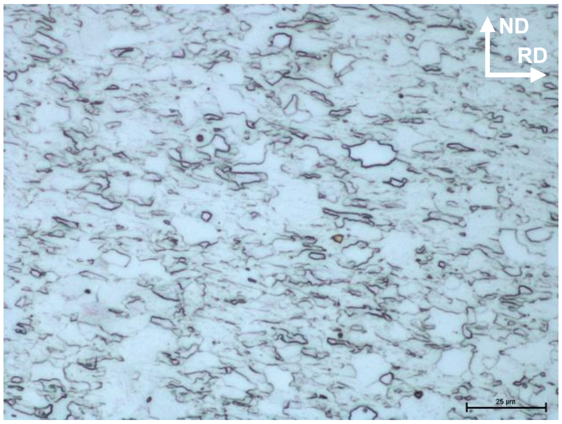

Figure 3.2.2.1.F: 575°C Heat Treatment at 500x Magnification for 0.2%Ti Steel

Figure 3.2.2.1.G: 575°C Heat Treatment at 200x Magnification for 0.4%Ti Steel

Figure 3.2.2.1.H: 575°C Heat Treatment at 500x Magnification for 0.4%Ti Steel

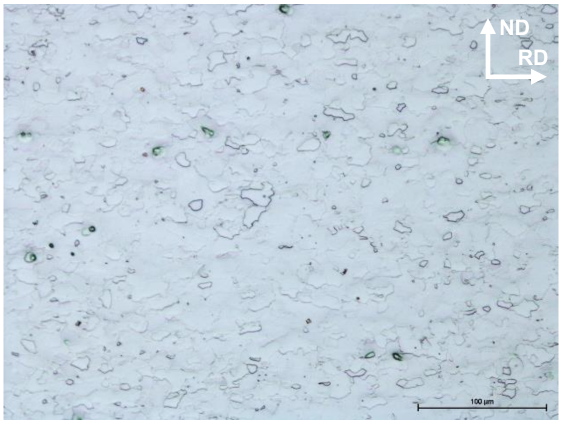

Figure 3.2.2.1.I: 600°C Heat Treatment at 200x Magnification for 0.2%Ti Steel

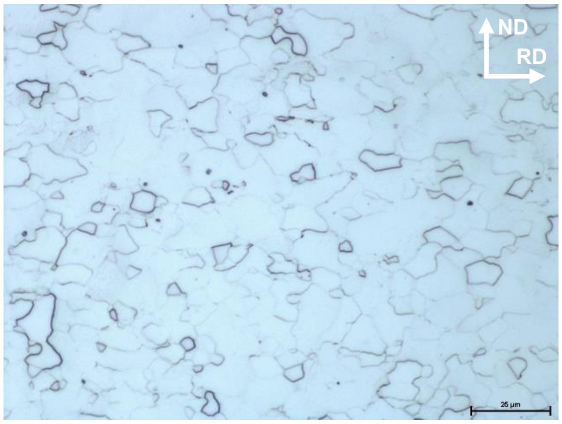

Figure 3.2.2.1.J: 600°C Heat Treatment at 500x Magnification for 0.2%Ti Steel

Figure 3.2.2.1.K: 600°C Heat Treatment at 200x Magnification for 0.4%Ti Steel

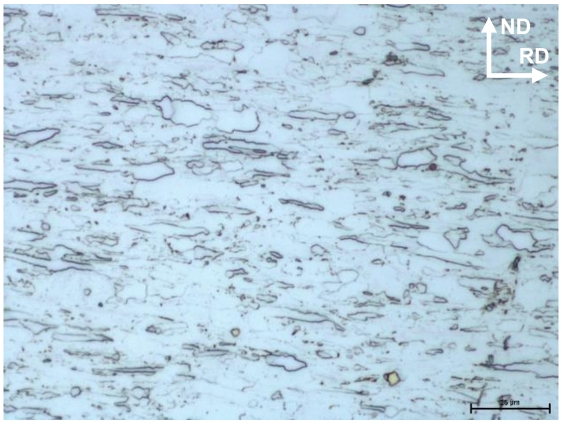

Figure 3.2.2.1.L: 600°C Heat Treatment at 500x Magnification for 0.4%Ti Steel

One can note how the higher concentration of titanium slows recrystallization, as the grains are less elongated in the 0.2%Ti steel as compared to the 0.4%Ti steel for the 575°C heat treatment. This is also seen in their mechanical properties, with the 0.4%Ti steel being stronger at this given heat treatment. This is further proved with misorientation maps calculated from EBSD data in section 3.2.2.4 as well as the Kochs-Mecking plots in section 3.3.3.1. Much like the 575°C heat treatment, the difference in microstructure between the 0.2%Ti and 0.4%Ti steels for the 600°C heat treatment is quite apparent, with the 0.4%Ti steel showing elongated grains from rolling, whereas the 0.2%Ti steel appears fully equiaxed. This too aligns with the results from the stress-strain curves and is confirmed by EBSD.

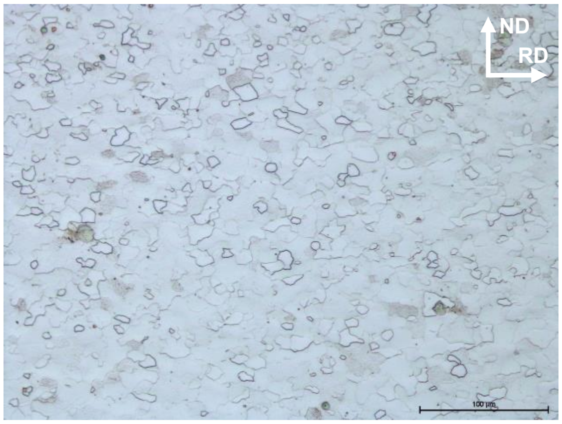

Figure 3.2.2.1.M: 650°C Heat Treatment at 200x Magnification for 0.2%Ti Steel

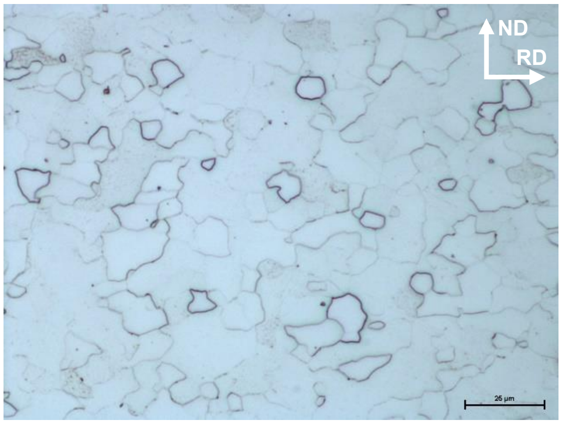

Figure 3.2.2.1.N: 650°C Heat Treatment at 500x Magnification for 0.2%Ti Steel

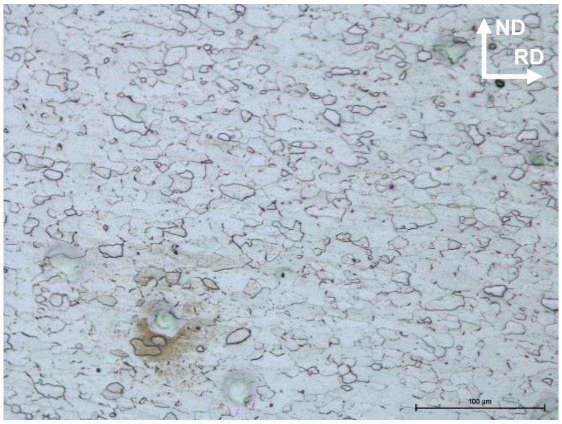

Figure 3.2.2.1.O: 650°C Heat Treatment at 200x Magnification for 0.4%Ti Steel

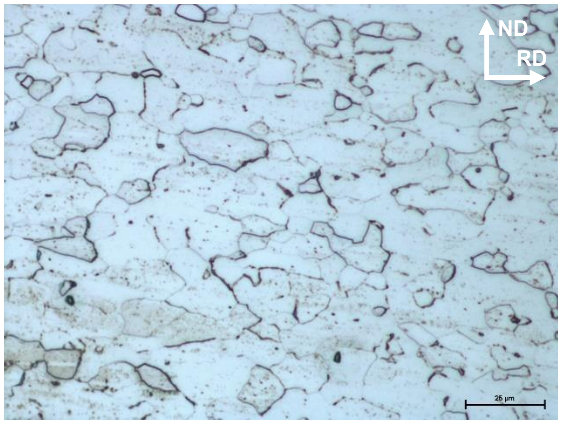

Figure 3.2.2.1.P: 650°C Heat Treatment at 500x Magnification for 0.4%Ti Steel

At temperatures of 650°C and above, both the 0.2%Ti and 0.4%Ti steel are fully recrystallized, and their microstructure does not change much even at 700°C.

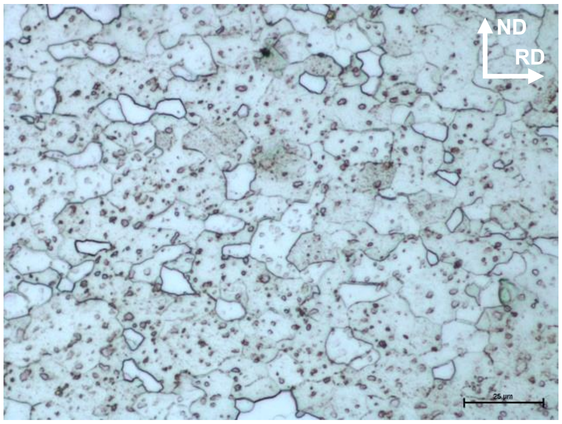

Figure 3.2.2.1.Q: 700°C Heat Treatment at 500x Magnification for 0.2%Ti Steel

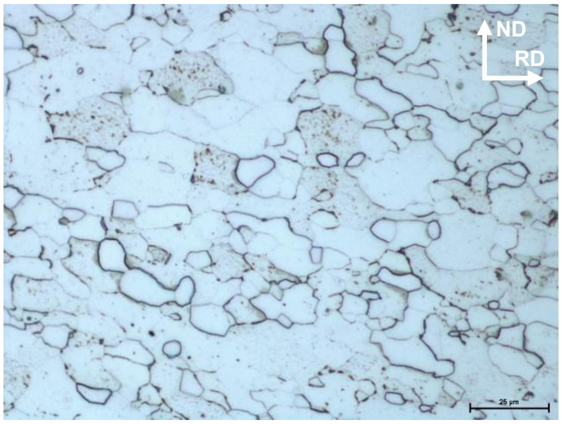

Figure 3.2.2.1.R: 700°C Heat Treatment at 500x Magnification for 0.4%Ti Steel

The dots on the 0.2%Ti steel are artifacts from etching and not true features.

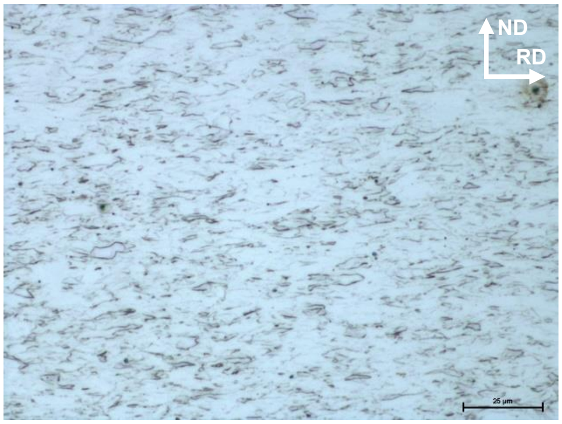

Figure 3.2.2.1.S: As Cold Rolled at 500x Magnification for 0.2%Ti Steel

Figure 3.2.2.1.T: As Cold Rolled at 500x Magnification for 0.4%Ti Steel

The microstructure of the cold rolled state is very similar in appearance to the microstructure at 550°C. This is good confirmation that recrystallization has not yet begun at these temperatures.

Both ImageJ and manual measurements were used for grain size measurement. Grains smaller than 5 μm^2 and larger than 500 μm^2 were excluded. The grain sizes are summarized in Table 3.2.2.1.A. Grains measured manually are marked with an asterisk and fully recrystallized microstructures are in blue.

Table 3.2.2.1.A: Summary of V20 Grain Sizes

Heat Treatment and Chemistry	Median Grain Size (μm^2)	Average Grain Size (μm^2)
550°C 0.2%Ti	8.3	11.2
575°C 0.2%Ti	9.7	14.8
600°C 0.2%Ti *	60.2	227
650°C 0.2%Ti	63.6	216
550°C 0.4%Ti	8.9	11.8
575°C 0.4%Ti	10.4	15.4
600°C 0.4%Ti	9.3	15.2
650°C 0.4%Ti*	58.8	257

As can be seen from this table, the median grain is smaller than the average grain size as a few very large grains skew the average. Furthermore, grain size remains relatively constant until recrystallization, at which point the grains grow significantly.

3.2.2.2 – SEM Characterization

An SEM was used to get higher magnification images of the steel to look at grains closer up to better observe the grains shape and size as well as to see any finer structures. Nonetheless, as the grains were visible in the optical microscope and the precipitates too fine to see in the SEM (see section 3.2.2.3, TEM Characterization), the primary use of the was to perform EBSD (section 3.2.2.4). At 2500x magnification the grains and grain boundaries are clearly visible. Images taken at 5000x magnification are included in Appendix D.

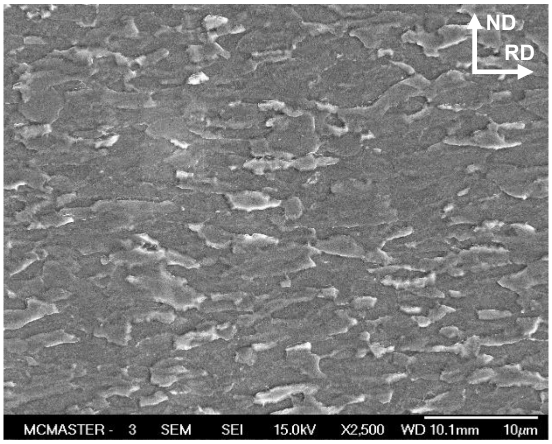

Figure 3.2.2.2.A: 0.2%Ti Steel Annealed at 550°C at 2500x in SEM

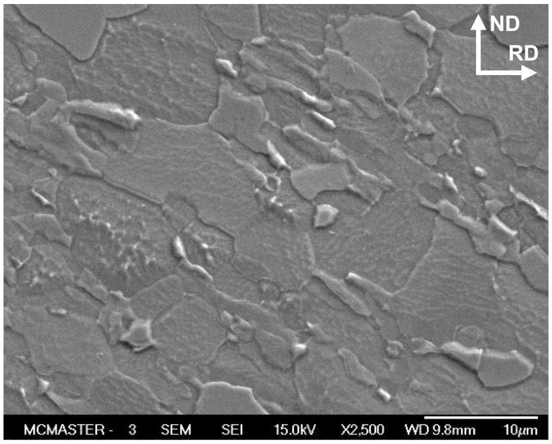

Figure 3.2.2.2.B: 0.2%Ti Steel Annealed at 575°C at 2500x in SEM

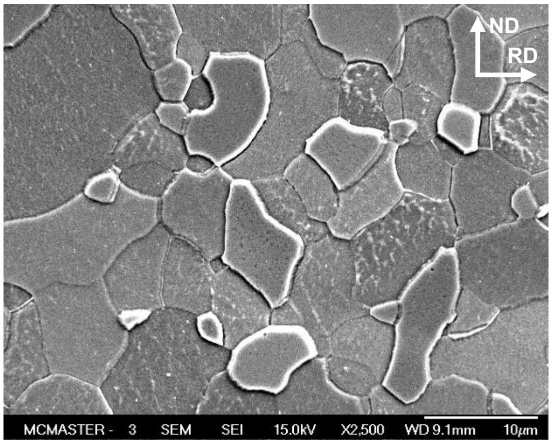

Figure 3.2.2.2.C: 0.2%Ti Steel Annealed at 600°C at 2500x in SEM

Another important factor to note is how much more the grains are deformed in the 0.4%Ti steel as shown by their elongated shape in the SEM images. This is confirmed by misorientation maps in EBSD (section 3.2.2.4).

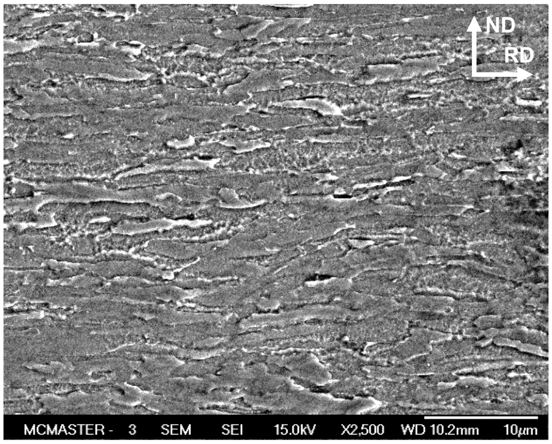

Figure 3.2.2.2.D: 0.4%Ti Steel Annealed at 550°C at 2500x in SEM

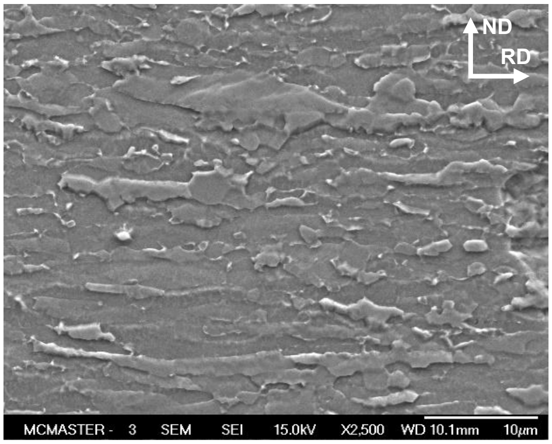

Figure 3.2.2.2.E: 0.4%Ti Steel Annealed at 575°C at 2500x in SEM

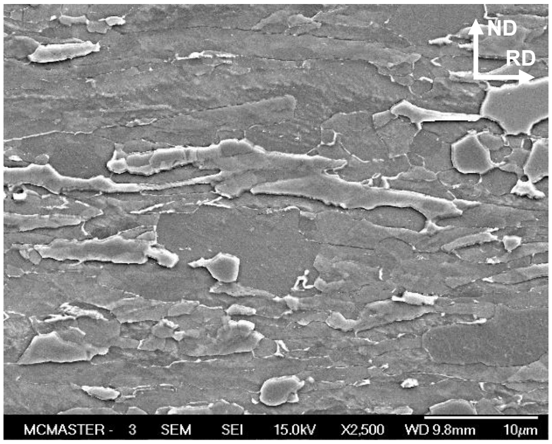

Figure 3.2.2.2.F: 0.4%Ti Steel Annealed at 600°C at 2500x in SEM

3.2.2.3 – TEM Characterization

The Talos 200X was used in STEM mode to look directly at the dislocations within the steel. STEM EDS was used to see if titanium segregates at grain boundaries or along dislocations, and to confirm the presence of microalloyed precipitates. Both bright field and dark field (HAADF) were performed at a variety of magnifications. The dark field images are included in this section and the bright field images are included in

Appendix E. No dislocations appear to be missed in the dark field as compared to the bright field images. The two steels studied were both of the 0.2%Ti composition, but one was annealed at 550°C and the other was annealed at 600°C, both for a 24 hour soak time.

In the 550°C steel, lots of dislocations can be seen within the grains. These dislocations are from the cold rolling of the steel and have not yet been removed due to the lower temperature of the anneal. In these dark field images, the dislocations appear as white lines. Representative pictures at different magnifications are shown.

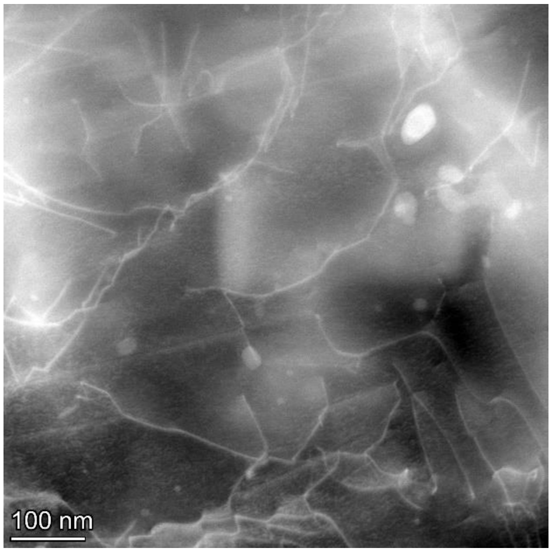

Figure 3.2.2.3.A: 0.2%Ti Steel Annealed at 550°C at 135kx in HAADF STEM

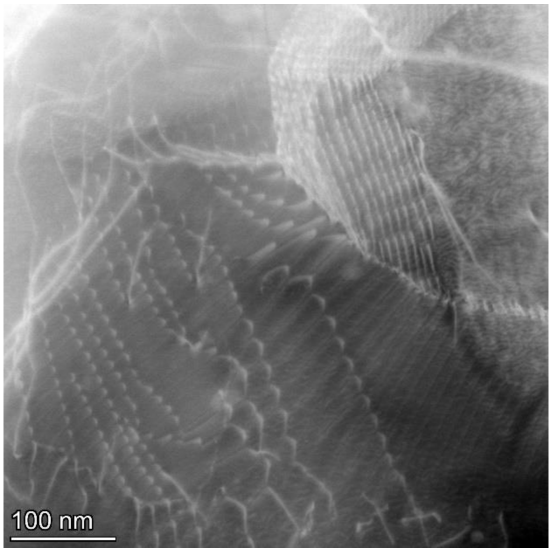

Figure 3.2.2.3.B: 0.2%Ti Steel Annealed at 550°C at 190kx in HAADF STEM

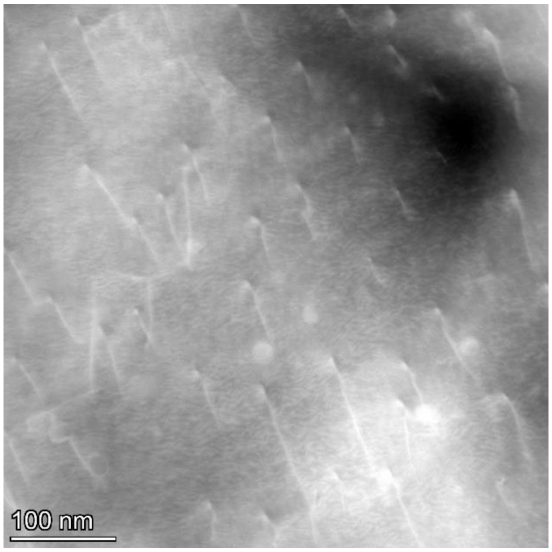

Figure 3.2.2.3.C: 0.2%Ti Steel Annealed at 550°C at 190kx in HAADF STEM Image 2

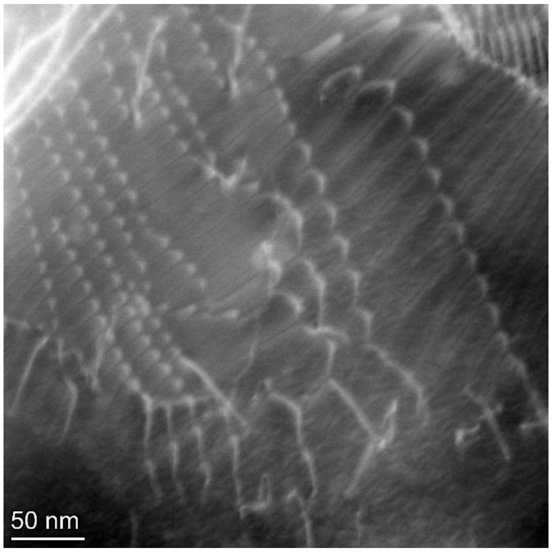

Figure 3.2.2.3.D: 0.2%Ti Steel Annealed at 550°C at 270kx in HAADF STEM

In Figures 3.2.2.3.B and 3.2.2.3.D, dislocations appear to align and bow. This could be dislocations moving around precipitates too small to see in the TEM, or could also be due to their alignment reducing their total surface energy. Nonetheless, this shows that the dislocations are at least slightly mobile in the steel.

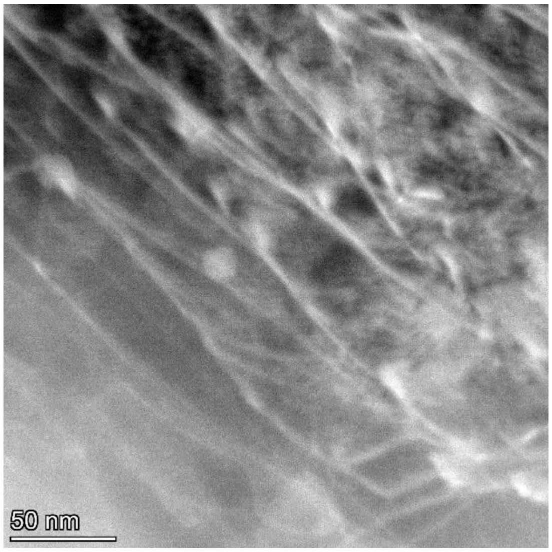

Figure 3.2.2.3.E: 0.2%Ti Steel Annealed at 550°C at 380kx in HAADF STEM

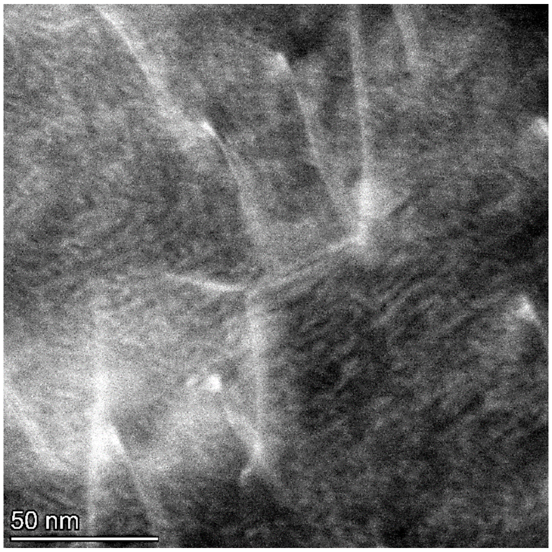

Figure 3.2.2.3.F: 0.2%Ti Steel Annealed at 550°C at 540kx in HAADF STEM

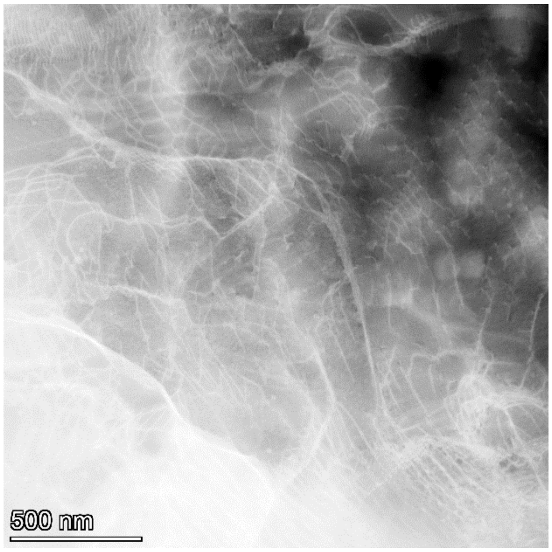

Figure 3.2.2.3.G: 0.2%Ti Steel Annealed at 550°C at 48000x in HAADF STEM

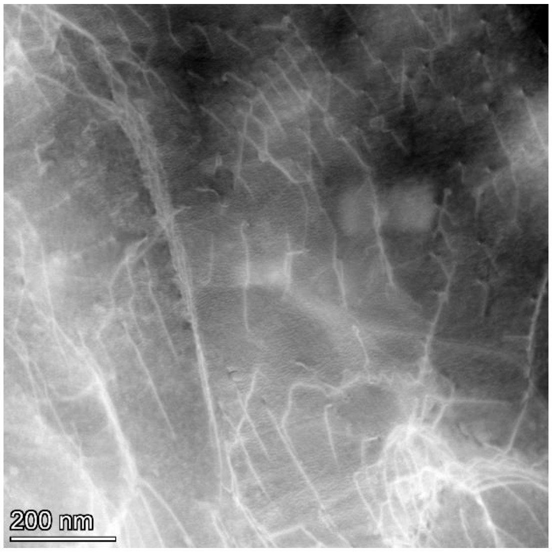

Figure 3.2.2.3.H: 0.2%Ti Steel Annealed at 550°C at 95000x in HAADF STEM

Similar images were collected on the steel heat treated at 600°C. The dark field images are included in this section; the bright field images are in Appendix E. Notably, the amount of dislocations is significantly reduced as expected due to recrystallization occurring at this temperature for this composition. Interestingly, the quantity of precipitates present increased dramatically increased as compared to the quantity in the 550°C steel, with an average diameter of 32nm.

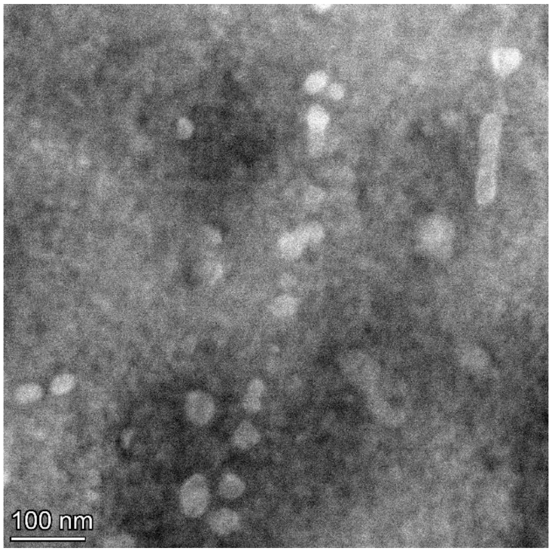

Figure 3.2.2.3.I: 0.2%Ti Steel Annealed at 600°C at 135kx in HAADF STEM

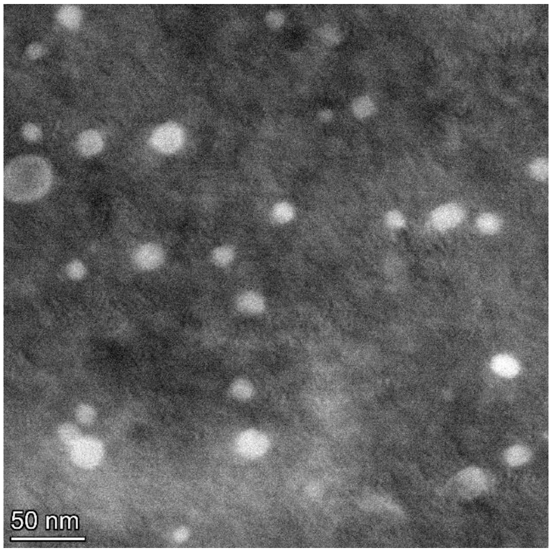

Figure 3.2.2.3.J: 0.2%Ti Steel Annealed at 600°C at 270kx in HAADF STEM

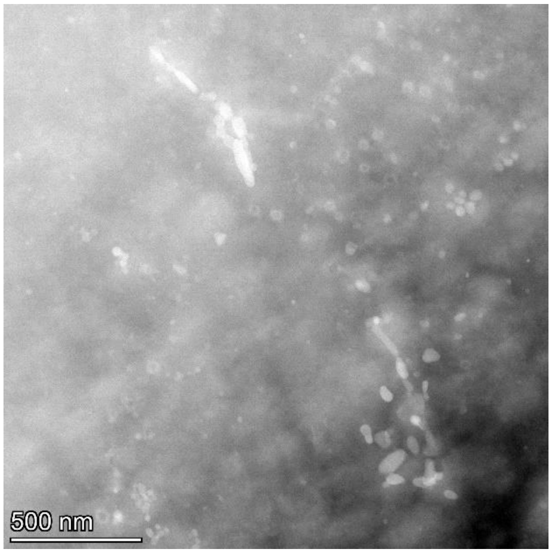

Figure 3.2.2.3.K: 0.2%Ti Steel Annealed at 600°C at 48000x in HAADF STEM

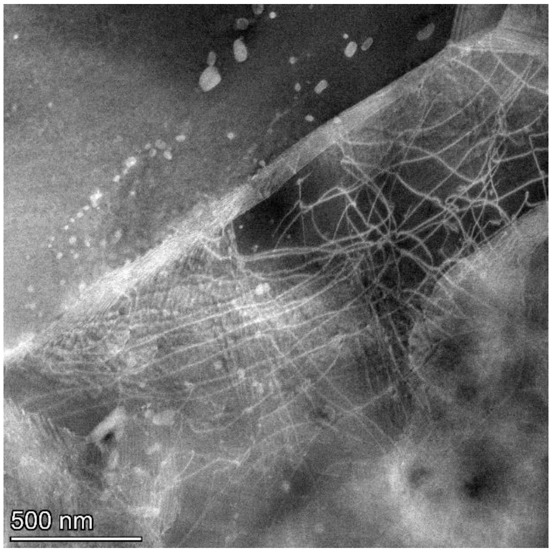

Figure 3.2.2.3.L: 0.2%Ti Steel Annealed at 600°C at 48000x With Dislocations in HAADF STEM

Even scanning a large area with low magnification, few dislocations remained. Only in some images were they visible, in others dislocations were completely absent. As dislocations do not cross grain boundaries (Figure 3.2.2.3.L), those that do remain show that some grains recrystallize before others.

EDS was then performed along a grain boundary and along dislocations to see if Ti or any other element segregates there. As seen in the EDS maps, the concentration of elements along grain boundaries and dislocations is not measurably different from the background; there does not appear to be any Ti segregation along neither grain boundaries nor dislocations. However, as the EDS lower detection limit is around 2%, the concentration of Ti may simply be too low to detect even if segregation occurs.

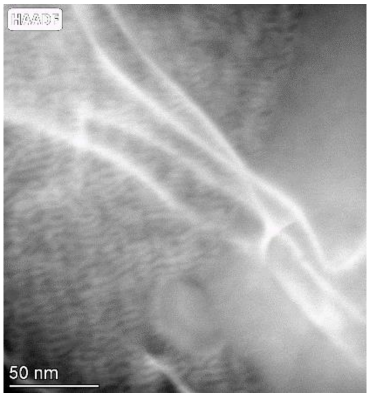

Figure 3.2.2.3.M: 0.2%Ti Steel Annealed at 550°C at 270kx, EDS Base for Dislocations

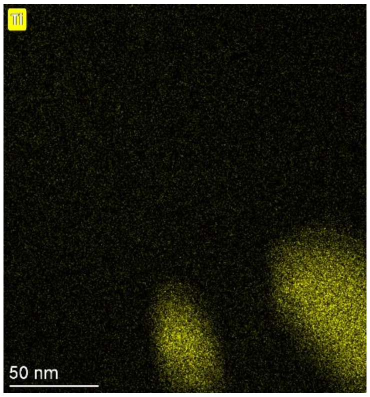

Figure 3.2.2.3.N: 0.2%Ti Steel Annealed at 550°C at 270kx, EDS Ti Map

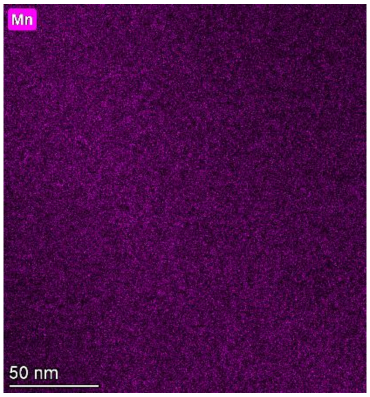

Figure 3.2.2.3.O: 0.2%Ti Steel Annealed at 550°C at 270kx, EDS Mn Map

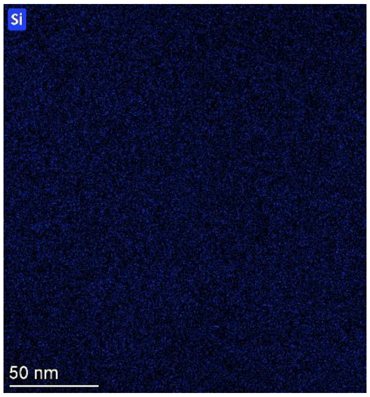

Figure 3.2.2.3.P: 0.2%Ti Steel Annealed at 550°C at 270kx, EDS Si Map

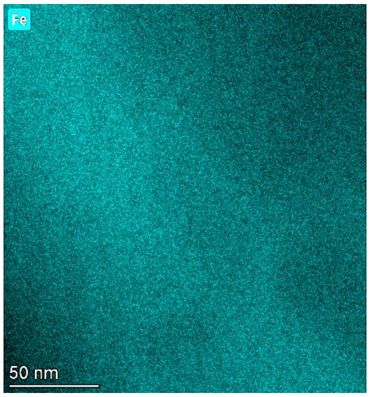

Figure 3.2.2.3.Q: 0.2%Ti Steel Annealed at 550°C at 270kx, EDS Fe Map

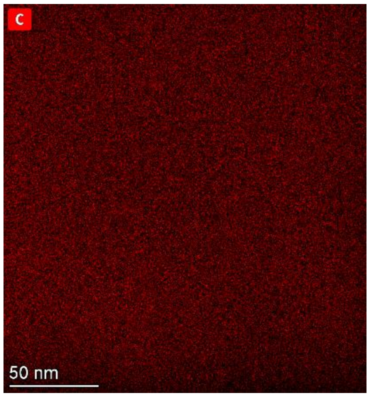

Figure 3.2.2.3.R: 0.2%Ti Steel Annealed at 550°C at 270kx, EDS C Map

As shown, no elements appear to segregate along the dislocations. The higher concentration of Ti is not along a dislocation, and rather a result of TiC precipitates. The higher concentration of Ti within the precipitates can be observed in Figure 3.2.2.3.T.

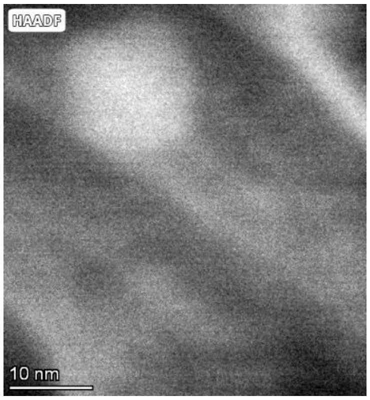

Figure 3.2.2.3.S: 0.2%Ti Steel Annealed at 550°C at 540kx, EDS Base for Precipitates

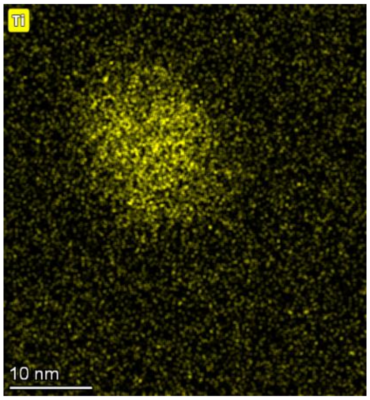

Figure 3.2.2.3.T: 0.2%Ti Steel Annealed at 550°C at 540kx, Ti EDS Map

EDS for all other elements known to be present in the steel was also performed, but no segregation to precipitates could be observed; those other maps are in Appendix F.

Likewise, EDS was performed along a grain boundary to observe if any segregation is present, and none was observed as shown in Figure 3.2.2.3.U.

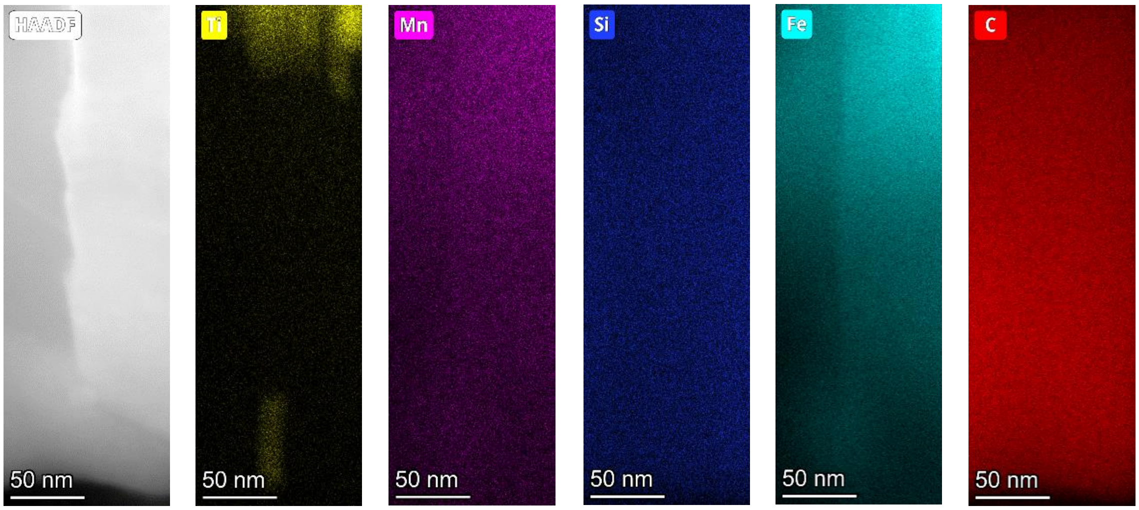

Figure 3.2.2.3.U: 0.2%Ti Steel Annealed at 550°C at 270kx,
a) EDS Base for Grain Boundaries
b) Ti EDS Map
c) Mn EDS Map
d) Si EDS Map
e) Fe EDS Map
f) C EDS Map

To corroborate the results of the lack of Ti segregation at dislocations and grain boundaries, electron energy loss spectroscopy was used as it is more precise and has a lower detection limit that traditional TEM EDS. TEM EELS was performed on the 0.2%Ti 550°C 24 hours annealed steel.

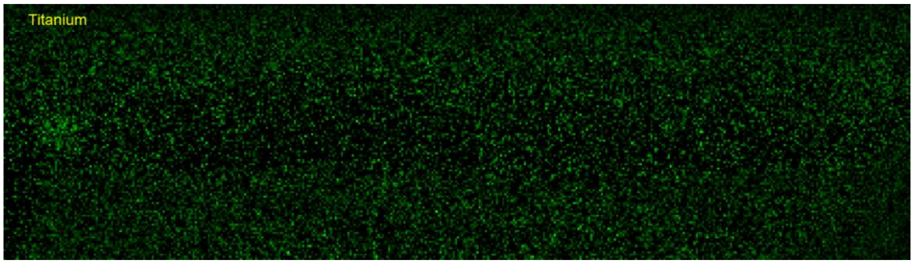

Figure 3.2.2.3.V: 0.2%Ti 550°C 24h EELS Ti Map

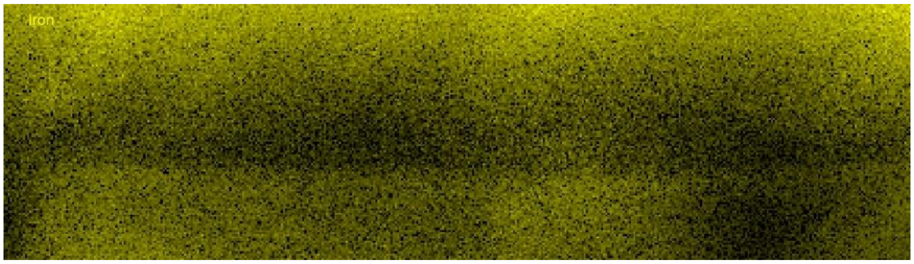

Figure 3.2.2.3.W: 0.2%Ti 550°C 24h EELS Fe Map

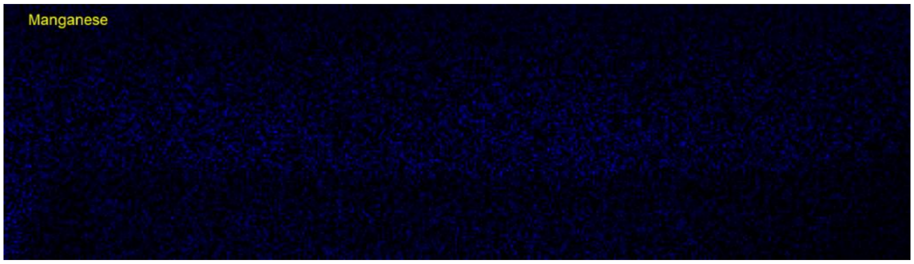

Figure 3.2.2.3.X: 0.2%Ti 550°C 24h EELS Mn Map

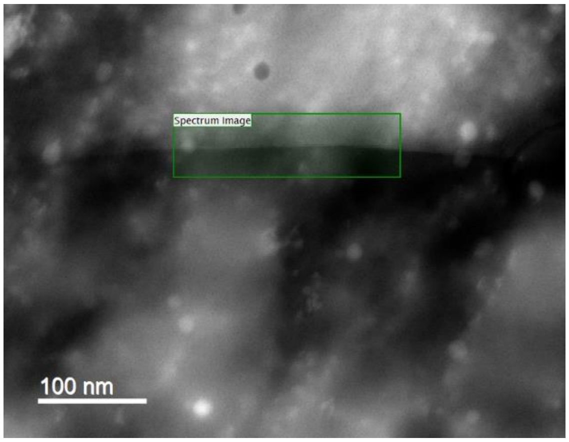

Figure 3.2.2.3.Y: Base Image for EELS Analysis

The maps on page 85 show a lack of titanium segregation at the grain boundary. This is confirmed with the raw EELS curves, which show no peak at the Ti L-edge.

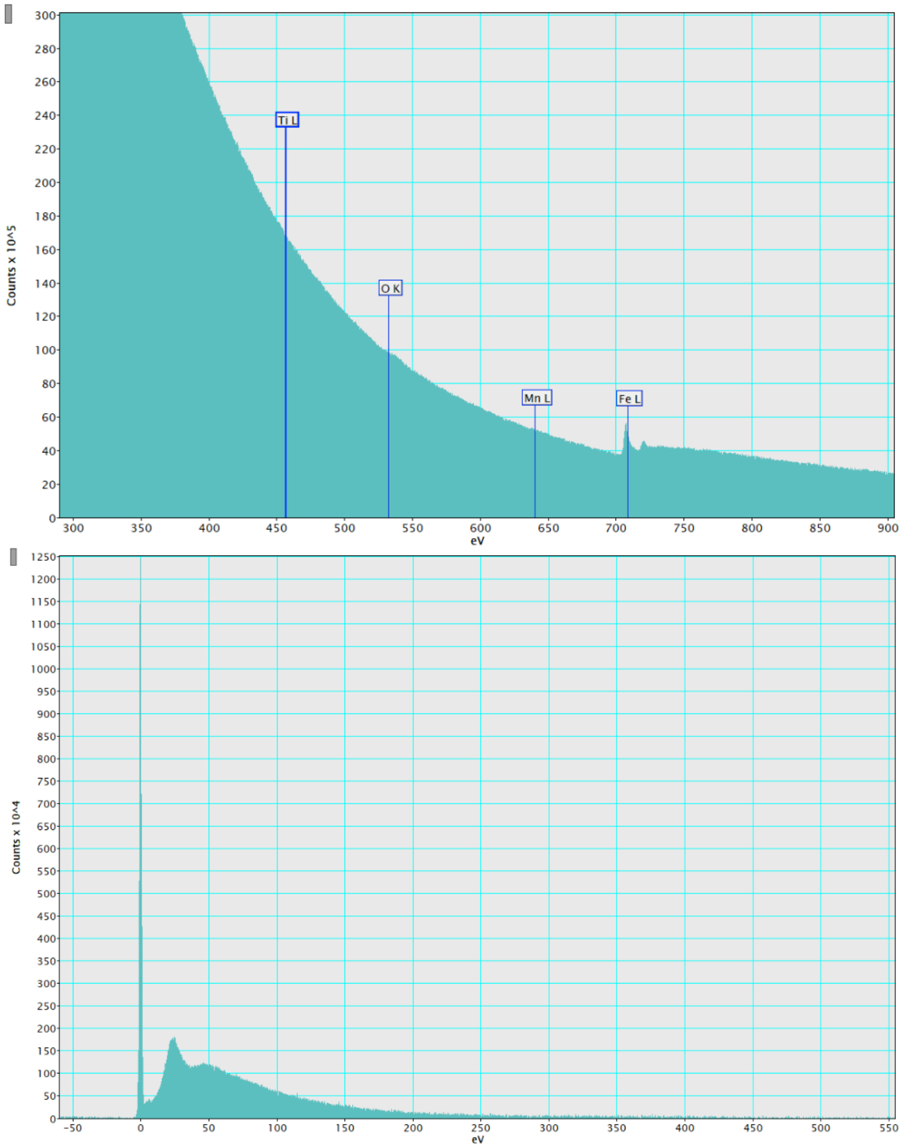

Figure 3.2.2.3.Z: EELS Spectrum,
a) Low Loss Region
b) High Loss Region

While EELS is has a lower detection limit that EDS, it is limited to concentrations above 1% for the microscope used. The steel tested has only 0.2%Ti, so even if the Ti concentration were 5 times higher, it could be missed in EELS. Additionally, as can be seen through the relatively high peak of the low-loss region, the sample was thicker than ideal, and this would further obscure the chemical information. As such, the existence of Ti segregation is still inconclusive.

3.2.2.4 – SEM EBSD Characterization

EBSD characterization was conducted for two main reasons. Firstly, EBSD was used to quantify the extent of recrystallization. To achieve this, kernel average misorientation maps are used to determine the amount of deformation within the grains, as recrystallized grains have minimal deformation, but recovered grains have substantial deformation. The existence of recovered grains means that dislocation strengthening is a dominant strengthening mechanism within the steel. Secondly, EBSD was conducted to look at texture within the steels. This is shown with IPF maps and pole figures.

EBSD was performed on four unique samples, the 550°C 0.2%Ti steel, the 575°C 0.2%Ti steel, the 575°C 0.4%Ti steel, and the 600°C 0.2%Ti steel. An area of 100μm×80μm was examined using a step size of 0.25μm.

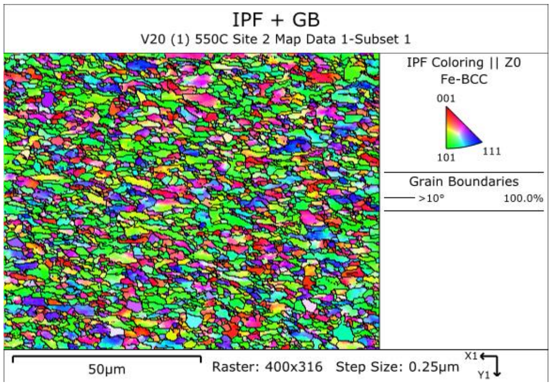

Figure 3.2.2.4.A: IPF EDS Map for 550°C 0.2%Ti Steel

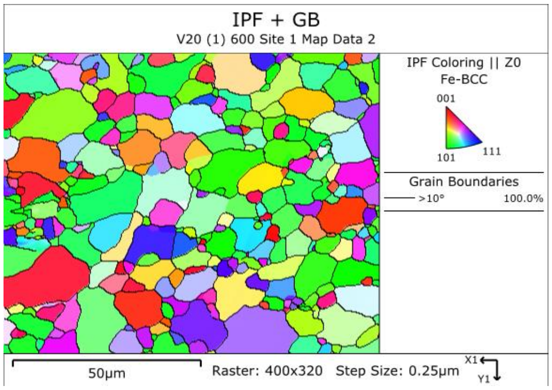

Figure 3.2.2.4.B: IPF EDS Map for 600°C 0.2%Ti Steel

As shown in the optical micrographs, the grain size increases significantly and the elongated grains become more circular at higher temperatures. Performing ImageJ on these IPF maps confirms the average grain sizes found in section 3.2.2.1, with an average grain size of 28μm^2 also found for the 600°C 0.2%Ti steel.

At 575°C for the 0.2%Ti steel, recrystallization begins to occur as shown by some large grains, but many grains remain small and elongated. At the same temperature, the 575°C 0.4%Ti steel shows minimal or no recrystallization. This is corroborated by the misorientation (KAM) maps.

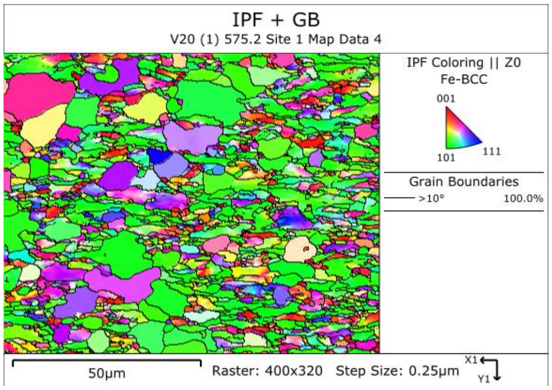

Figure 3.2.2.4.C: IPF EDS Map for 575°C 0.2%Ti Steel

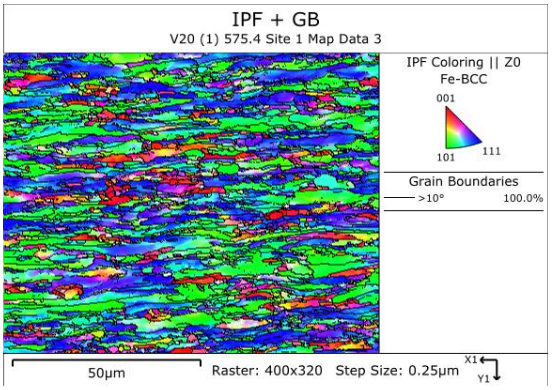

Figure 3.2.2.4.D: IPF EDS Map for 575°C 0.4%Ti Steel

In the misorientation (KAM) maps, blue represents fully recrystallized grains, whereas green, yellow, and red represent grains with deformation, which are therefore recovered grains.

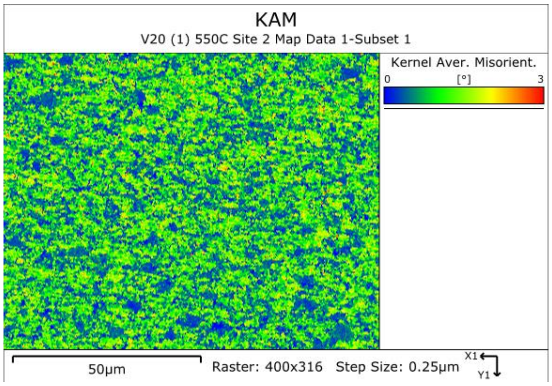

Figure 3.2.2.4.E: Misorientation Map for 550°C 0.2%Ti Steel

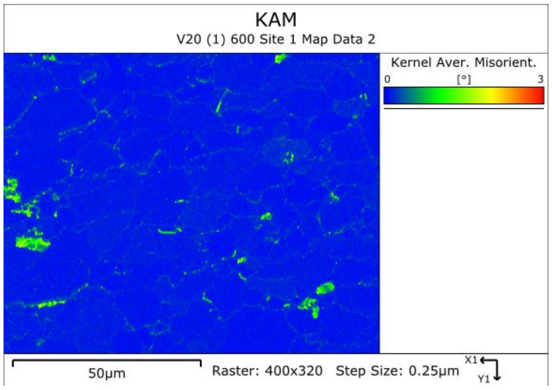

Figure 3.2.2.4.F: Misorientation Map for 600°C 0.2%Ti Steel

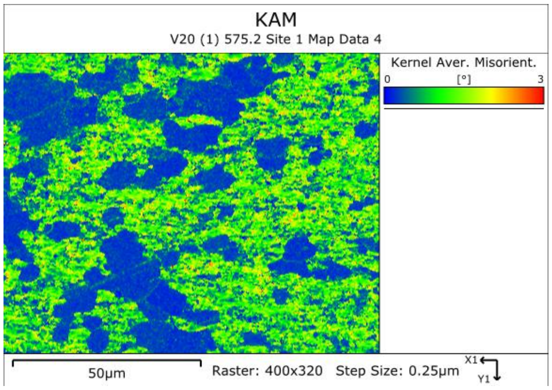

Figure 3.2.2.4.G: Misorientation Map for 575°C 0.2%Ti Steel

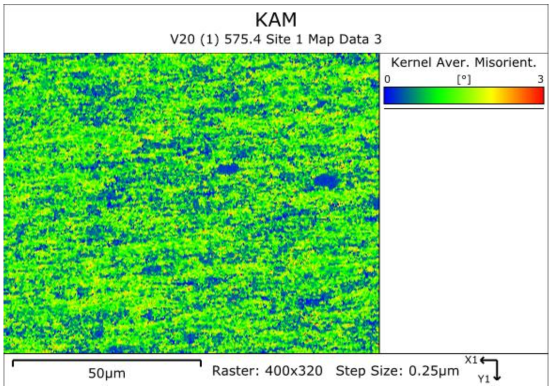

Figure 3.2.2.4.H: Misorientation Map for 575°C 0.4%Ti Steel

From these misorientation maps, the extent of recrystallization becomes very apparent. At 550°C the field is almost completely green, at 575°C there are some blue areas and some green areas, whereas at 600°C, the entire field is blue. This confirms that recrystallization for the 0.2%Ti steel occurs between 550°C and 600°C, with partial recrystallization occurring at 575°C.

Furthermore, the misorientation maps confirm that titanium retards recrystallization in steel, as at 575°C the 0.4%Ti steel is still in the recovered microstructure as shown by the primarily green map.

This EBSD data was further processed to create pole figures, as the IPF maps appear to show some clear texture and pole figures can provide confirmation. These pole figures are included below.

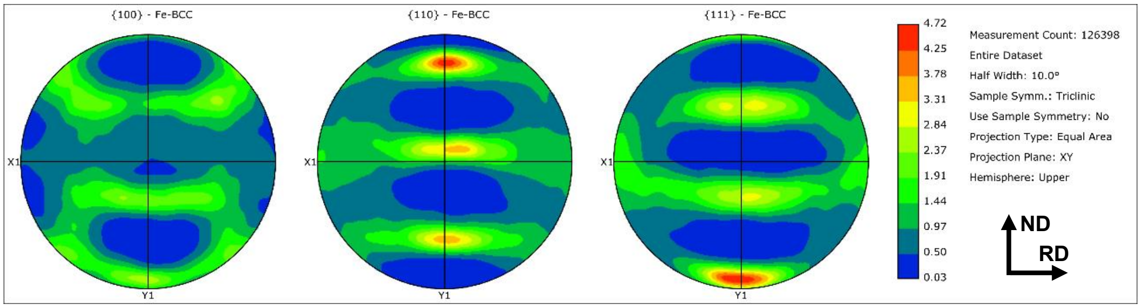

Figure 3.2.2.4.I: 550°C 0.2%Ti Steel Pole Figures

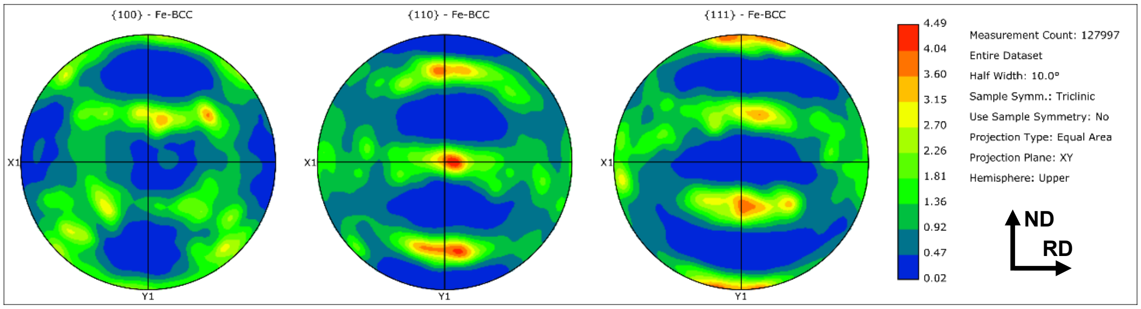

Figure 3.2.2.4.J: 575°C 0.2%Ti Steel Pole Figures

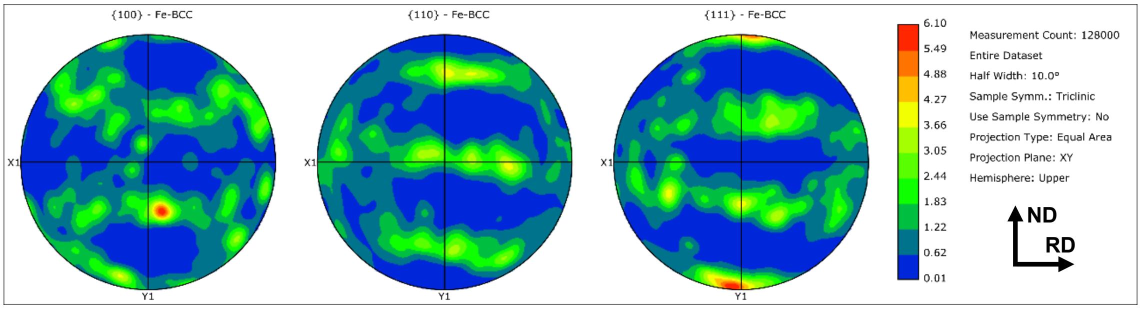

Figure 3.2.2.4.K: 600°C 0.2%Ti Steel Pole Figures

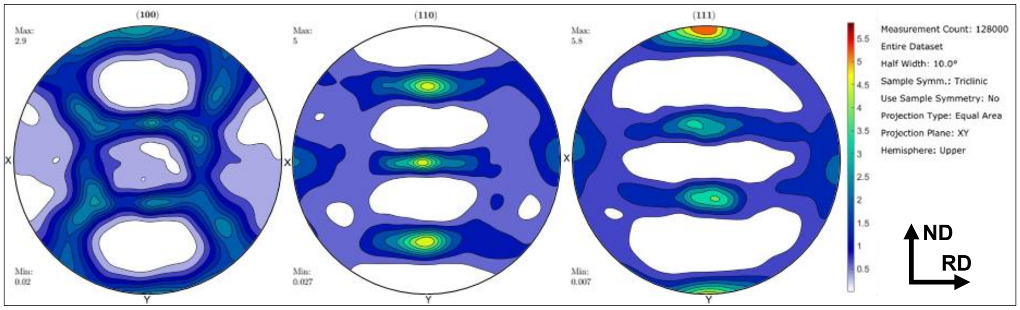

Figure 3.2.2.4.L: 575°C 0.4%Ti Steel Pole Figures

These pole figures show drawing/rolling texture in all the steels [55]. Note the 0.4%Ti pole figure was measured at the same time, but rendered with different software.

3.2.2.5 – APT Characterization

Given that neither TEM EDS nor TEM EELS showed Ti segregation, atom probe tomography was employed. APT has near atomic precision and is therefore sensitive enough to determine conclusively if there is any Ti segregation [56]. To increase the likelihood of imaging Ti segregation, the 0.4%Ti 550°C sample was used. To confirm the presence of substructures within the APT sample, the liftouts were first imaged in a TEM.

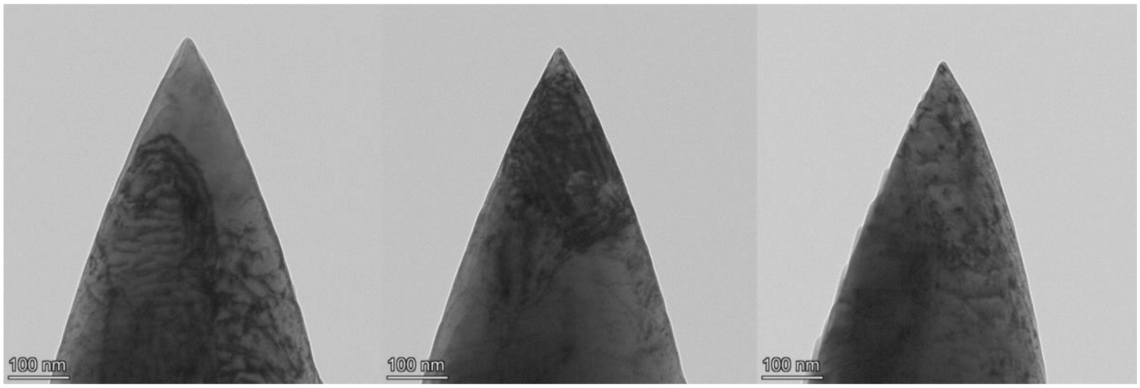

Figure 3.2.2.5.A: TEM Images of APT Tip #1 at 15° Rotations

As can be seen from the TEM image, there is an abundance of dislocations within the tip. However, these dislocations are not visible in the APT as seen in Figure 3.2.2.5.B.

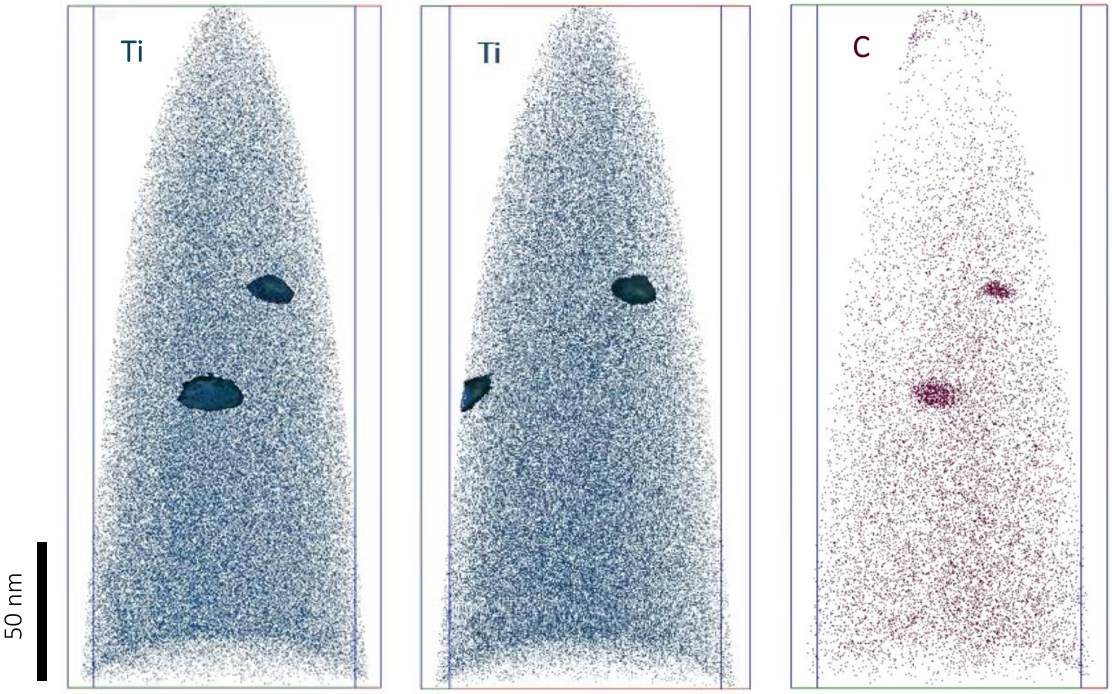

Figure 3.2.2.5.B: APT Tip #1 Showing TiC Precipitates,
a) Ti Map with 0.5% Ti Isosurface
b) Ti Map with 0.5% Ti Isosurface, Rotated 90°
c) C Map

The lack of visibly decorated boundaries in the APT, combined with the correlative technique of using the TEM conclusively confirms that titanium does not segregate to dislocations in this steel.

However, titanium did segregate to grain boundaries, as shown in the second APT tip. The presence of this grain boundary was confirmed using TEM and the fact that Mn segregated to it as well. This is known to be a grain boundary and not a dislocation because it does not feature parallel lines at different rotations, rather just one line. More images of the APT tip and TEM images thereof are included in Appendix G.

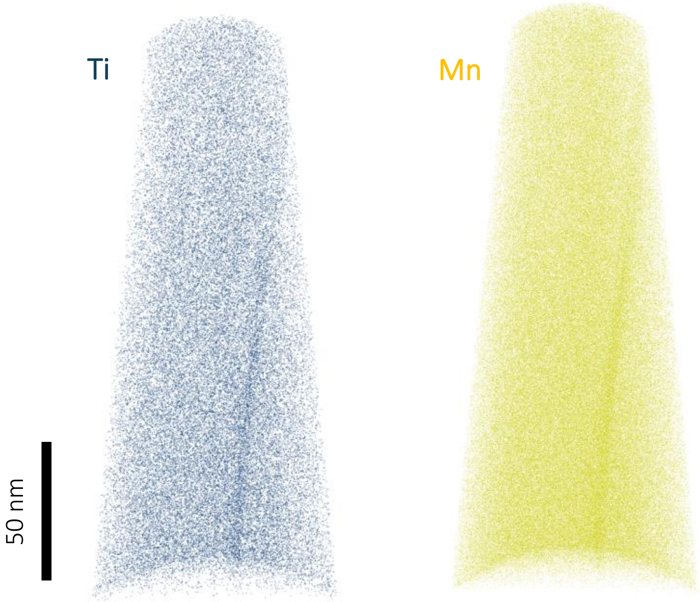

Figure 3.2.2.5.C: APT Tip #2 Showing Ti and Mn Segregation at Grain Boundary

3.3 – Discussion

This section aims to explain the sources of strength within the steel as well as explain its microstructure and properties based off the research conducted in this thesis, previously conducted research from literature, and empirical mathematical models.

3.3.1 – ThermoCalc Simulations

ThermoCalc 2022a was used to perform thermodynamics simulations. The *TCFE12: Steels/Fe-Alloys v12.0* package was used for the thermodynamics simulations. The composition of the steel was input into ThermoCalc as shown in Table 3.0.1.A, excluding sulfur and oxygen as they are present only in trace amounts and do not contribute to the formation of carbonitrides or other precipitates. The phases of graphite and Fe2SiTi were also excluded from the simulation.

3.3.1.1 – Thermodynamics Simulations

The volume fractions of the phases were modeled using a one axis equilibrium plot graphing volume fraction as a function of temperature. These plots are shown with two different axes.

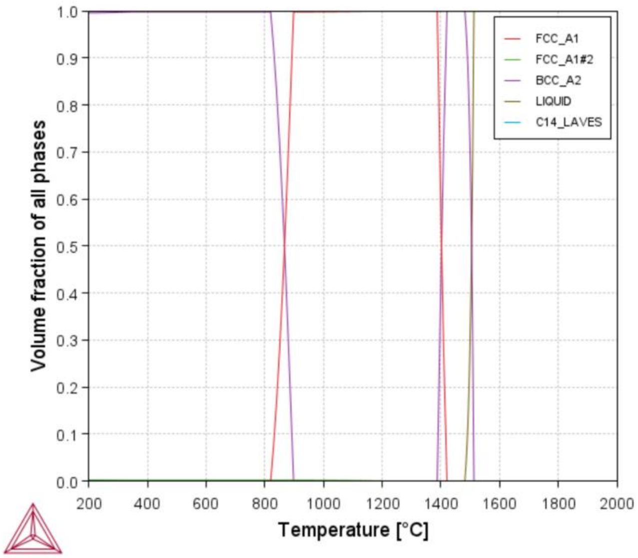

Figure 3.3.1.1.A: Volume Fraction of Phases

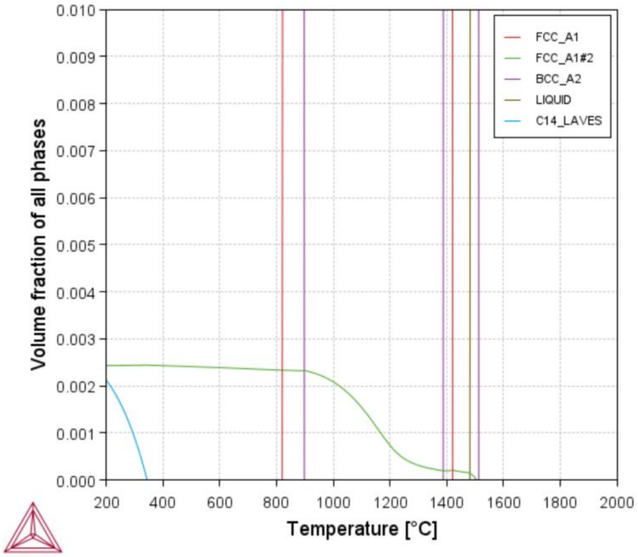

Figure 3.3.1.1.B: Volume Fraction of Phases Zoomed In

At a temperature of 500°C (below which the diffusion is too slow to form more precipitates) the phases present are FCC_A1 and FCC_A1#2. These represent ferrite and titanium carbonitride, respectively.

3.3.2 – Recovery and Recrystallization

The key aspect of the microstructure of the V20 steels is that the microstructure remains in the recovered state, even after annealing. The key requirement for this to occur is that the recovery temperature must be below the recrystallization temperature. In this case, the annealing step below the recrystallization temperature maintains a significant amount of strength, while regaining sufficient ductility.

Ductility is gained during recovery through the annihilation of some, but not all, dislocations [37]. However, if the grains are allowed to recrystallize, they become significantly larger and are essentially free of all dislocations, which greatly reduces their strength [37].

There are four main regions of materials properties in regard to microalloyed steel and annealing time/temperature. First, there is the cold-rolled state, which has high strength but an extreme lack of ductility. This was seen in the mechanical properties of the cold-rolled V20 steel. Afterwards, the recovery-annealed state, where there is a jump in ductility coupled with a decrease in yield strength as compared to the cold-rolled state, as seen in the steels annealed at 525°C to 550°C. The third phase is the partially recrystallized phase, where properties change rapidly with changes in annealing time and temperature, as seen with the marked differences in properties between 550°C and 600°C for the 0.2%Ti steel (or between 575°C and 650°C for the 0.4%Ti steel). Lastly, there is the fully recrystallized state, where properties remain nearly constant once complete recrystallization has occurred. This is demonstrated by the nearly identical properties of the fully recrystallized steels, regardless of annealing temperature between 600°C and 700°C (or 650°C to 700°C for the 0.4%Ti steel), as well as by the similarity of their mechanical properties to the hot rolled state.

Graphs for properties of batch-annealed microalloyed steel with varying annealing parameters is shown in Figure 3.3.2.A and Figure 3.3.2.B, which confirm the mechanical behaviour seen in the V20 steel [57]. Note that "M" is a parameter that combines annealing time and temperature, with higher values corresponding to higher annealing temperatures and longer annealing times [57].

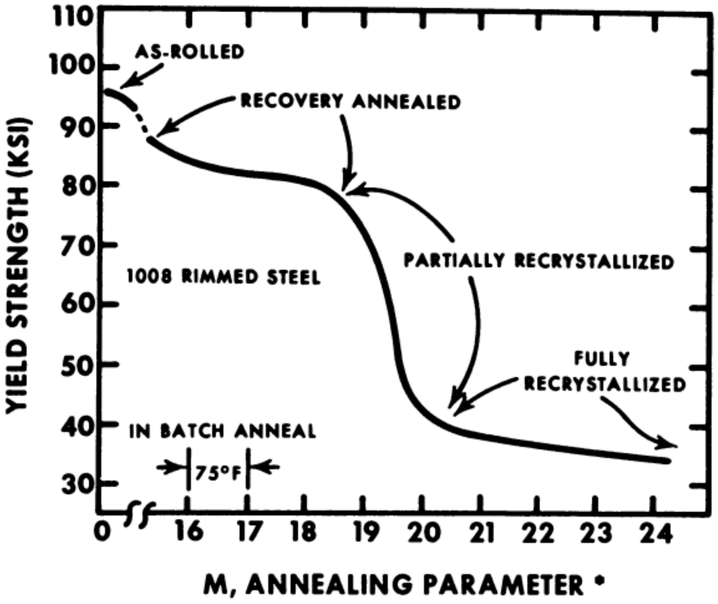

Figure 3.3.2.A: Yield Strength vs. "M" Annealing Parameter [57]

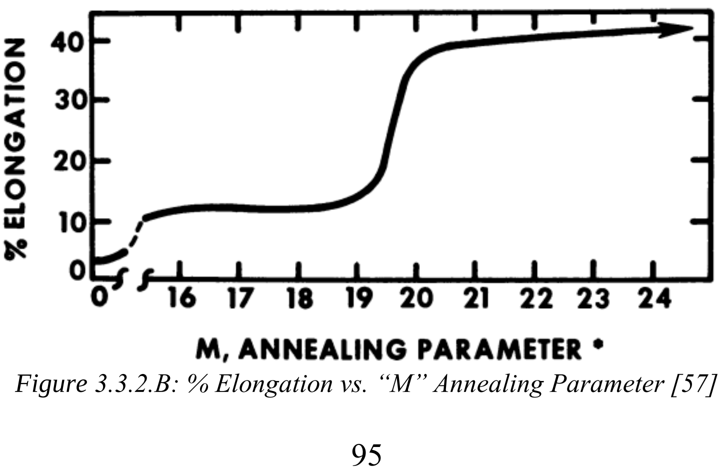

Figure 3.3.2.B: % Elongation vs. "M" Annealing Parameter [57]

Of key importance is the increase in elongation from the cold-rolled state to the recovered state (Figure 3.3.2.B, bottom-left corner). This allows for the steel to be acceptably ductile while still maintaining significant strength. In Ti containing HSLA steels, this change between the cold-rolled and recovered state happens at a relatively low temperature; the recovery temperature is low [57]. This is crucial as for the steel to maintain sufficient strength, this recovery temperature must be below the recrystallization temperature.

3.3.3 – Sources of Strength

The strength of this steel comes from the intrinsic strength of iron, the solid solution strengthening from the Mn and Si, the precipitate strengthening from the microalloy carbonitrides, grain boundary strengthening, and primarily from the dislocations induced during cold working that are maintained during the recovery annealing. The calculation will be performed for the 0.2%Ti steel at 600°C as this steel is expected to be fully recrystallized and thus the contribution of strength from the recovery annealing can be isolated. Furthermore, extensive microscopy has been performed at this temperature allowing for more accurate calculations.

The contribution to strengthening from the intrinsic strength of pure iron is given as 50MPa [11]. The contribution to strengthening from solid solution strengthening comes from the dissolved Mn and Si, which is given by their weight percentage in the steel as they are not involved in the creation of precipitates, so their weight percentage in the alloy is the same as their dissolved weight percentage in the steel. The solid solution strengthening coefficients for Mn and Si are 31 and 81, respectively [2]. With 1.85% Mn and 0.50% Si, this results in a contribution to strengthening of 1.76×31 + 0.89×81 = 127MPa.

The precipitate strengthening is calculated using equation 1.5a with values of 0.0024 at 600°C for volume fraction and an average particle diameter of 32nm (as found in section 3.2.2.3), which results in an increase of strength of 44MPa. As expected, this is quite small as there is a low amount of carbon and nitrogen in the steel to reduce the formation of carbonitrides, to ensure that titanium remains in the matrix so that it can slow recrystallization.

Lastly, there is grain boundary strengthening. Using a k_y of 550MPam$^{1/2}$ and an average grain length of 15.2μm (as found in section 3.2.2.1) results in an additional 142MPa of strength.

The combined total for these forms of strengthening results in an estimated yield strength of 363MPa. This is statistically identical to the measured 364MPa of the 0.2%Ti 600°C heat treatment, which proves the validity of these calculations.

For the steels heat treated at lower temperatures, much of the additional strength is through dislocation strengthening in the recovered microstructures (the other large contribution is through grain boundary strengthening). These microstructures maintain much of the dislocations induced during cold rolling as they are recovery-annealed and not recrystallized. In fact, the strength of the recovered microstructures of the 0.2%Ti steel varied from 671MPa to 635MPa, which is an increase in strength of between 235-310MPa.

3.3.3.1 – Work Hardening and True Stress and Strain

Work hardening occurs as dislocations are formed during plastic deformation, which increases the strength of the material. Simultaneously, necking occurs, which reduces the cross-sectional area of the material thus locally increasing pressure. Evaluating true stress and true strain allows for another understanding of the mechanical properties of the material, especially its work hardening rate. Work hardening is expected to be more pronounced in steels heat treated at higher temperatures, and this is well documented in other HSLA steels too [58]. This section confirms this correlation.

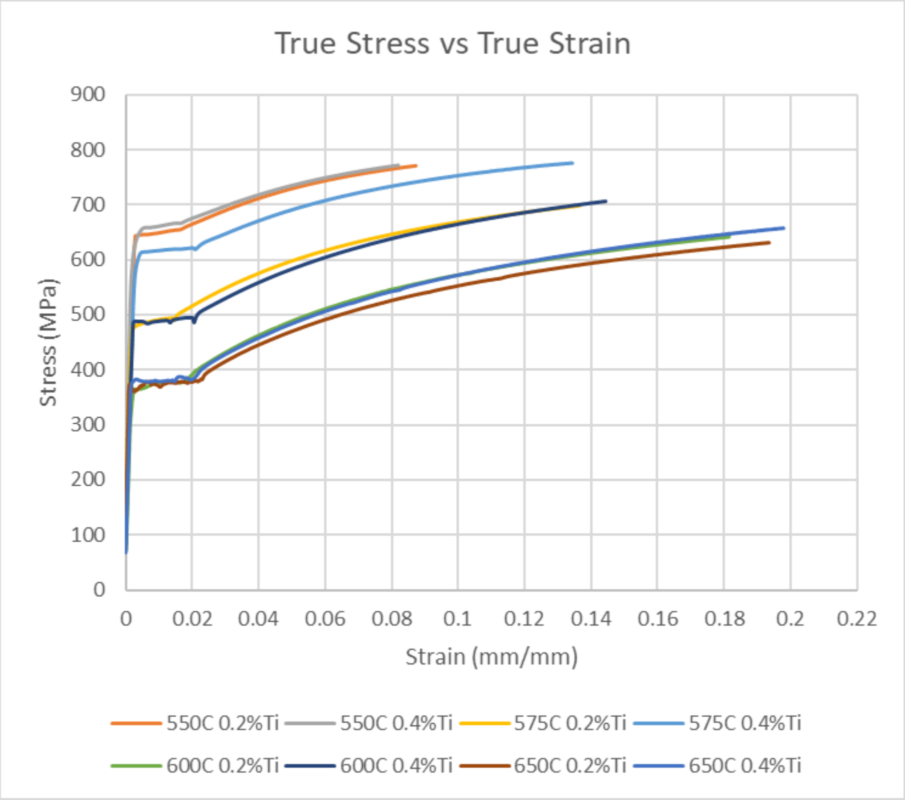

Figure 3.3.3.1.A: True Stress-Strain Curves of Selected Steels to Point of Necking

The true stress-strain curves in Figure 3.3.3.1.A show the degree of work hardening within the different steels. Note that this graph was created using logarithmic relationships between true stress and strain and their engineering counterparts, and so they end at the point of necking where the relationship becomes invalid, and not at the point of failure. From these graphs, a log-log plot can be created to estimate the work-hardening rate of the steel. The slope of the lines on the log-log plot represent this value [25]. Visually, one can see that there is more of work-hardening (steeper lines) in the weaker steels heat treated at higher temperatures. This makes sense as their beginning dislocation density is less, so they can increase the dislocation density relatively faster during deformation endured while undergoing tensile testing.

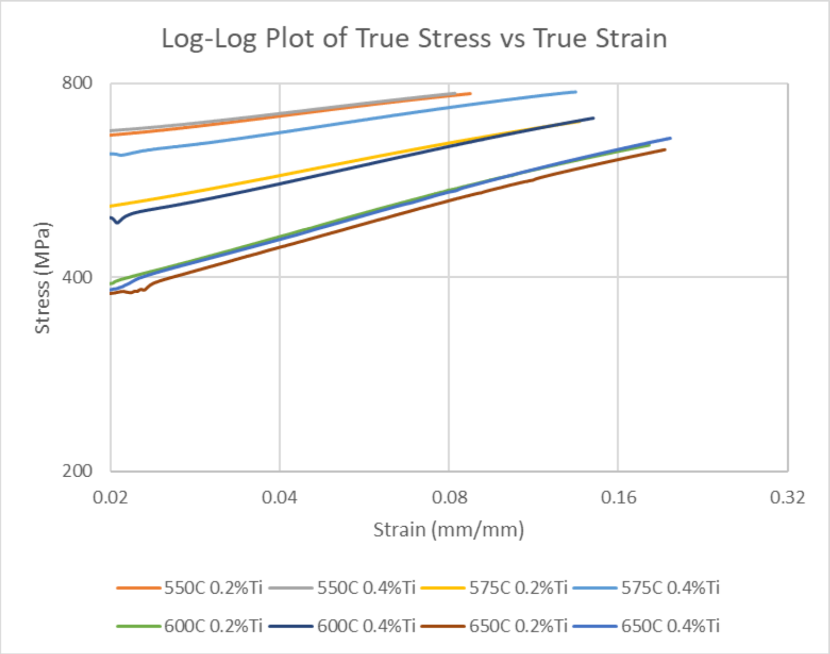

Figure 3.3.3.1.B: Log-Log Plot of Linear Region of True Stress-Strain Curves of Selected Steels

Taking the derivative of the slopes yields Kocks-Mecking plots, which further corroborates these findings. These graphs are included on the next page.

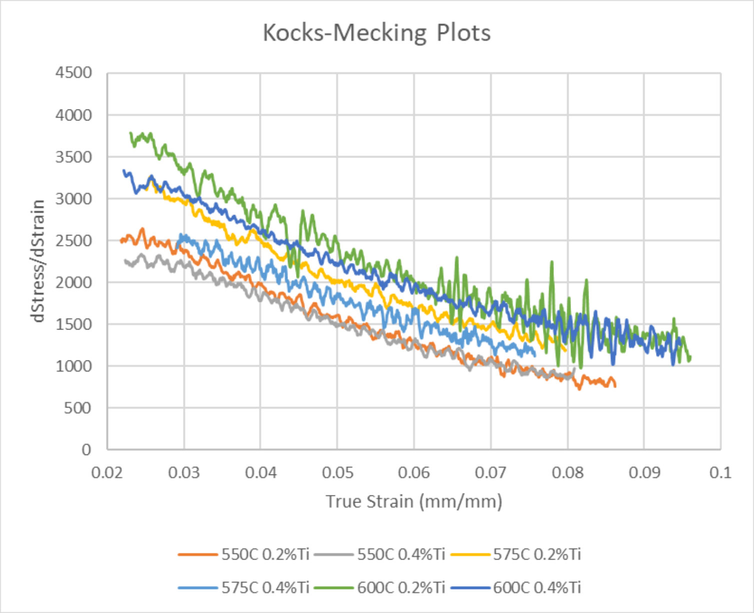

Figure 3.3.3.1.C: Linear Region of Kocks-Mecking Plots of Selected Steels

From the Kocks-Mecking plots, the steels heat treated at higher temperatures are higher on the graph, also confirming their higher rates of work hardening [59].

Including the true stress-strain curves for the large tensile tests shows much the same data. Furthermore, showing this graph with their true stress and strain at fracture shows just how much necking occurred near the fracture surface; the thickness of the sample at the neck after fracture is around half the original thickness.

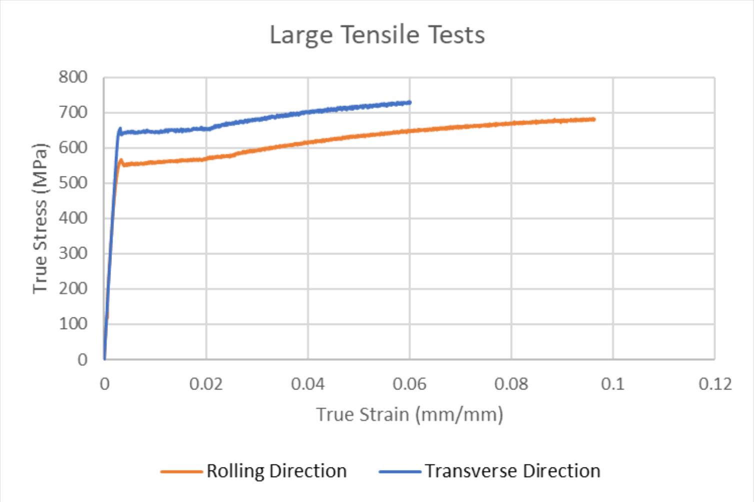

Figure 3.3.3.1.D: True Stress-Strain Curves of Large Tensile Tests to Point of Necking

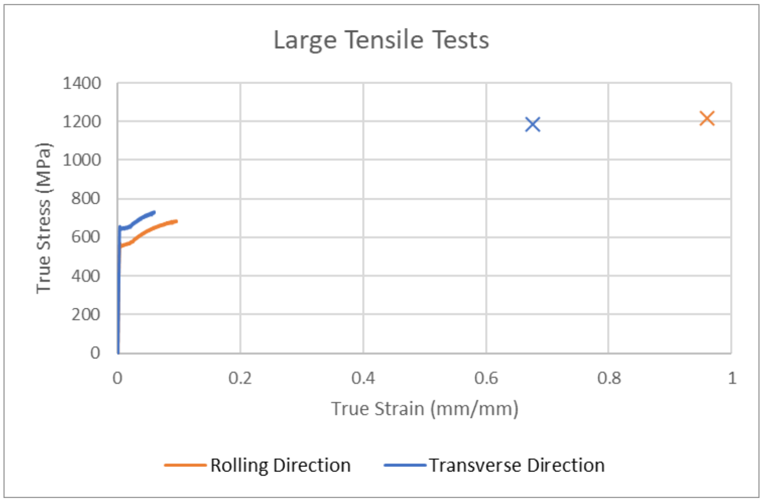

Figure 3.3.3.1.E: True Stress-Strain Curves of Large Tensile Tests Including Points at Fracture

The benefit of the V20 steel showing very large amounts of post-uniform elongation is the possible applications in forming operations, such as in hole expansion.

3.3.3.2 – Dislocation Interactions and Segregation

Further analysis of the dislocation density can be done by using the relationship that flow stress is proportional to the square root of dislocation density [60]. The increase in flow stress at the 550°C 24 hour soak as compared to the fully recrystallized or as hot-rolled sample is roughly 270MPa as shown in section. Using an α of 0.1-0.2 and assuming edge dislocations for the burger vector distance, that gives a range of dislocation densities of 5×10^{14} to $2\times10^{15}/m^2$. This is quite high and further proves the importance of these dislocations within the steel. The role of titanium within the steel is different to that of niobium and other solute elements. Niobium segregates to dislocations, but titanium does not [61]. An APT map is included on the next page showing the niobium-decorated dislocation in a 0.53% Nb containing ferritic steel, which is a feature not found in the APT samples looked at for the V20 steel [61].

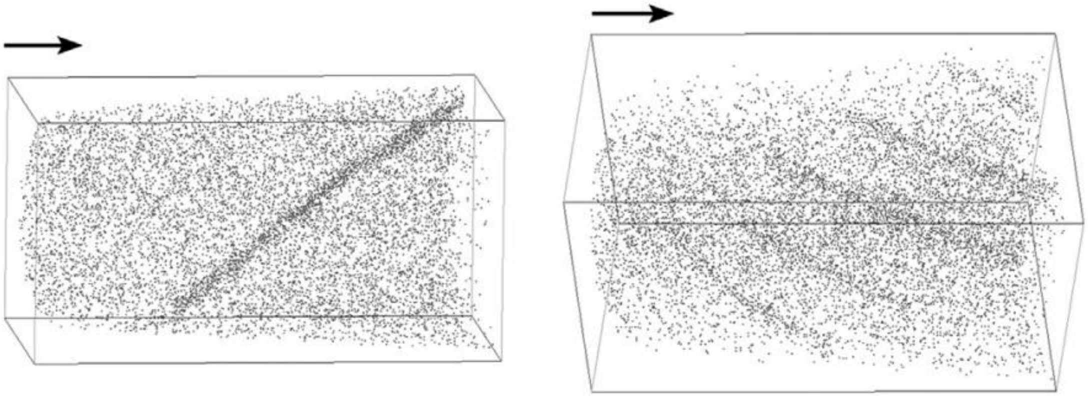

Figure 3.3.3.2.A: Nb Decorating a Dislocation in an APT Map of a Nb Containing Steel [61]

3.3.4 – Uniqueness of Titanium in Strengthening

Titanium is relatively unique as a solute element as it is able to slow the onset of recrystallization without needing to form precipitates nor dislocate to segregations, as shown in the experiments conducted on the V20 steel.

This property of not segregating to dislocations may confer some benefits to the V20 steel over other recovery-annealed steels. For example, Ti containing recovery-annealed have better ductility than their equivalent steels with boron [62]. As boron causes Ti segregation to dislocations, recovery in those steels is slower, which makes recovery overlap with recrystallization such that ductility cannot be gained without a large sacrifice in strength [61], [62].

Furthermore, titanium slows the recrystallization in steel without the need of Zener pinning. This is seen as the 0.4%Ti steel has a later onset of recrystallization than the 0.2%Ti steel, despite having the same volume fraction of precipitates as carbon is the limiting element in the creating of TiC precipitates in the V20 steel. Consequently, one can create strong low-carbon steels, which has certain advantages and applications, such as being more weldable than higher carbon steels.

3.3.5 – Mechanism of Delaying of Recrystallization

Given that no Ti segregation to dislocations was found, one cannot say with complete certainty why titanium delays the onset and progression of recrystallization. Nonetheless, there are some explanations.

One explanation, put forward by Professor J. David Embury, is that titanium segregates to the intersections of dislocations [63]. This would still pin dislocation networks, but not decorate the dislocation itself. As these intersections are small and infrequent, they could be missed in the APT.

Another explanation is through that of solute drag at the grain boundaries. As shown in the APT, titanium does segregate to the grain boundaries. Furthermore, titanium has a higher binding energy than most other metals in ferrite, at around 27kJ/mol [64]. This value is roughly double that of manganese and silicon [64]. Solute drag is linearly proportional to concentration, but exponentially proportional to binding energy [27]. As such, elements with higher binding energies could play an outsized role in drag on the grain boundaries due to this exponential factor.

3.3.6 – Commercial Application

The impetus for this thesis was set out by requests from the automobile industry. They requested a microalloyed steel with the following targets: yield strength greater than 500MPa, ultimate tensile strength of 560-700MPa, and % elongation at fracture of 16%.

As can be seen in the Table 3.3.6.A, these targets were met, and in fact exceeded, by the V20 steel, specifically the 0.2%Ti 36h at 550°C heat treatment. The ± represents a 90% confidence interval. Note that these results are for the subsize tests.

Table 3.3.6.A: Comparison of V20 Properties to Industry Targets

Property	**Target**	**V20 0.2%Ti 36h 550°C**
Yield Strength (MPa)	500<	606 ± 22
Tensile Strength (MPa)	560<	680 ± 41
Elongation at Fracture (%)	16<	19.4 ± 1.6

3.3.6.1 – Feasibility of Production

Batch annealed steels face some issues in regard to their production. Principally, the precision of a batch annealing furnace is quite limited, to roughly within 20°C of the target temperature. Furthermore, the hot and cold spots of the roll heat up and cool down differently; they undergo slightly different heat treatments due to the nature of heat transfer through large objects. As such, to be commercially viable, any batch annealed steel must have a large processing window in terms of both time and temperature. The V20 steel achieved this. The difference in strength between the 550°C 36h heat treatment and 525°C 36h heat treatment is only 60MPa, and the difference in strength between the 550°C 24h heat treatment and 550°C 24h heat treatment is only 33MPa. Given an annealing time of an additional 12 hours, or a change in annealing temperature of 25°C, these variations are quite minimal. As such, this steel not only meets the targets set out, but also the secondary requirement of being commercially feasible to produce.

CONCLUSIONS

The research conducted in this thesis set out to develop a new microalloyed (HSLA) steel under the constraint of the slow thermal processing parameters found within a batch annealing furnace. The first steel, V10, does show some promise in this application with a yield strength of 605MPa and an elongation at fracture of 15.4% for a 50mm gauge length under optimal processing parameters.

However, the truly exciting development is in the recovery-annealed V20 steel. This steel has a very similar yield strength to the V10 steel of 606MPa, but with an increased elongation at fracture of 19.4% for a 25.4mm gauge length under its optimal processing parameters. Furthermore, this steel is cheaper to produce due to the lack of costly vanadium and molybdenum, all while being lenient of varying annealing times.

The key to this steel is that the uniqueness with which titanium slows recrystallization. By not segregating to dislocations like Nb, and not relying on Zener pinning through precipitates, the mechanism of action of titanium on slowing recrystallization is entirely novel. As well, this steel allows for some recovery to occur to regain ductility without beginning recrystallization such that strength is also maintained.

More experiments should be performed to better understand and exploit this phenomenon. Nonetheless, the knowledge that this is a new mechanism is alone an achievement, and should spur more research into this area. Science is never complete; there is always more to learn. However, from an engineering perspective, this steel has been fully quantified as its composition, processing, and production steps are described in detail, and microstructure extensively investigated.

Due to the economical cost of production, relative robustness, and excellent mechanical properties, this class of Ti containing recovery-annealed steels shows great promise in the future. One can expect to see more of these types of Ti containing steels in the future as the HSLA steel market expands and the demand for stronger and more cost-effective steels becomes even greater.

REFERENCES

[1] Steels for aircraft structures. (2012). Introduction to Aerospace Materials, 232–250. doi:10.1533/9780857095152.232

[2] T. Gladman, The Physical Metallurgy of Microalloyed Steels, London: The Institute of Materials, 1997

[3] R. Krupitzer, R. Miner, P. Arend, F. Reis, J. Slane, J. Abraham, S. Matas. (1977). Progress in HSLA Steels in Automotive Applications. SAE Transactions, 86, 708–717. http://www.jstor.org/stable/44644110

[4] J. Paules. (1991). Developments in HSLA steel products. JOM, 43(1), 41–44. doi:10.1007/bf03220117

[5] Straights Research. (2020). Microalloyed Steel Market. https://straitsresearch.com/report/microalloyed-steel-market

[6] H. Zurob. (2003) Effects of Precipitation, Recovery and Recrystallization on the Microstructural Evolution of Microalloyed Austenite. http://hdl.handle.net/11375/7532

[7] Total Materia. (2011). Application of Microalloyed HSLA Steel: Part One. https://www.totalmateria.com/page.aspx?ID=CheckArticle&site=kts&LN=TR&NM=347#:~:text=Microalloy%20(MA)%20or%20High%20Strength,of%20total%20world%20steel%20production.

[8] W. Callister & D. Rethwisch. Materials Science and Engineering An Introduction, New York: John Wiley & Sons, Inc., 2014

[9] T. Courtney. Mechanical Behaviour of Materials, Waveland Press, 2000

[10] K. Kashyap, A. Bhat, P. Koppad, K. Puneeth. (2012). On Peierls Nabarro stress in Iron. Computational Materials Science, 56, 172–173. doi:10.1016/j.commatsci.2011.12.033

[11] E. Lukon, K. Abiko, M. Lambrecht, B Rehmer. (2015). Tensile Properties of Commercially Pure, High-Purity and Ultra-High-Purity Iron: Results of an International Round-Robin, NIST Technical Note 1879. http://dx.doi.org/10.6028/NIST.TN.1879

[12] T. Gladman. (1999). Precipitation hardening in metals. Materials Science and Technology, 15(1), 30–36. doi:10.1179/026708399773002782

[13] F. Liu, A. Cocks, E. Tarleton. (2021). Dislocation dynamics modelling of the creep behaviour of particle-strengthened materials. Proceedings. Mathematical, physical,

and engineering sciences vol. 477,2250 (2021): 20210083. doi:10.1098/rspa.2021.0083

[14] D. Hull, D. Bacon. Introduction to Dislocations, Butterworth-Heinemann, 2011

[15] A. DeArdo, M. Hua, K. Cho, C. Garcia. (2009). On strength of microalloyed steels: an interpretive review. Materials Science and Technology, 25(9), 1074–1082. doi:10.1179/174328409x455233

[16] D. Gawne, G. Lewis. (1985). Strengthening mechanisms in high-strength microalloyed steels. Materials Science and Technology, 1(3), 183–191. doi:10.1179/mst.1985.1.3.183

[17] W. Poole, X. Wang, D. Lloyd, J. Embury. (2005). The shearable–non-shearable transition in Al–Mg–Si–Cu precipitation hardening alloys: implications on the distribution of slip, work hardening and fracture. Philosophical Magazine, 85(26-27), 3113–3135. doi:10.1080/14786430500154935

[18] E. Hutten (2019) The Development of High Strength Hot Rolled Steel for Automotive Applications, http://hdl.handle.net/11375/24349

[19] TCS Steel and Fe-alloys Database (TCFE12). (2021). Thermo-Calc Software

[20] K. Xu, B. Thomas, R. O’malley, (2010). Equilibrium Model of Precipitation in Microalloyed Steels. Metallurgical and Materials Transactions A, 42(2), 524–539. doi:10.1007/s11661-010-0428-7

[21] W. Soboyejo. Mechanical Properties of Engineered Materials, Marcel Dekker, 2003

[22] N. Filonenko, O. Babachenko, G. Kononenko. (2020). Investigation of Carbon, Manganese and Silicon Solubility in α-Iron of Fe-Mn-Si-C Alloys. 2020 IEEE 10th International Conference Nanomaterials: Applications & Properties (NAP), pp. 01NSSA01-1-01NSSA01-4, doi:10.1109/NAP51477.2020.9309708.

[23] S. Takaki. (2010). Review on the Hall-Petch Relation in Ferritic Steel. Materials Science Forum, 654-656, 11–16. doi:10.4028/www.scientific.net/msf.654-656.11

[24] M. Yoshino, C. Kami. (2016). Influence of Grain Size on Work-Hardening Behavior in 12Cr Stainless Steel. Materials Science Forum, 879, 2228–2233. doi:10.4028/www.scientific.net/msf.879.2228

[25] W. Hosford, R. Caddel, Metal Forming: Mechanics and Metallurgy, Cambridge University Press, 2011

[26] Y. Han, J. Shi, L. Xu, W. Cao, H. Dong. (2012). Effect of hot rolling temperature on grain size and precipitation hardening in a Ti-microalloyed low-carbon martensitic steel. Materials Science and Engineering: A, 553, 192–199. doi:10.1016/j.msea.2012.06.015

[27] J. Cahn. (1962). The impurity-drag effect in grain boundary motion. Acta Metallurgica, 10(9), 789–798. doi:10.1016/0001-6160(62)90092-5

[28] M. Suehiro, Z. Liu, J. Ågren. (1998). A mathematical model for the solute drag effect on recrystallization. Metallurgical and Materials Transactions A, 29(13), 1029–1034. doi:10.1007/s11661-998-1012-2

[29] T. Oikawa, J. Zhang, M. Enomoto, Y. Adachi. (2013). Influence of Carbide Particles on the Grain Growth of Ferrite in an Fe–0.1C–0.09V Alloy. ISIJ International, 53(7), 1245–1252. doi:10.2355/isijinternational.53.1245

[30] S. Ringer, W. Li, K. Easterling. (1989). On the interaction and pinning of grain boundaries by cubic shaped precipitate particles. Acta Metallurgica, 37(3), 831–841. doi:10.1016/0001-6160(89)90010-2

[31] J. Moon, C. Lee. (2012). Pinning efficiency of austenite grain boundary by a cubic shaped TiN particle in hot rolled HSLA steel. Materials Characterization, 73, 31–36. doi:10.1016/j.matchar.2012.07.003

[32] T. Chakrabarti, S. Manna. (2018). Zener pinning through coherent precipitate: A phase-field study. Computational Materials Science, 154, 84–90. doi:10.1016/j.commatsci.2018.07.041

[33] N. Wang, Y. Ji, Y. Wang, Y. Wen, L. Chen. (2017). Two modes of grain boundary pinning by coherent precipitates. Acta Materialia, 135, 226–232. doi:10.1016/j.actamat.2017.06.031

[34] N. Li, et al. (2020). Processing maps for hot working of HSLA pipeline steel. Materials Research Express. doi:10.1088/2053-1591/ab6768

[35] R. Hossain, F. Pahlevani, M. Quadir, V. Sahajwalla. (2016). Stability of retained austenite in high carbon steel under compressive stress: an investigation from macro to nano scale. Scientific Reports, 6(1). doi:10.1038/srep34958

[36] Michler, T. (2016). Austenitic Stainless Steels. Reference Module in Materials Science and Materials Engineering. doi:10.1016/b978-0-12-803581-8.02509-1

[37] A. Martínez-de-Guerenu, D. Jorge-Badiola, I. Gutiérrez. (2017). Assessing the recovery and recrystallization kinetics of cold rolled microalloyed steel through coercive field measurements. Materials Science and Engineering: A, 691, 42–50. doi:10.1016/j.msea.2017.03.033

[38] Z. Larouk, H. Bouhalais. (2009). Recrystallization behavior of a low carbon steel wire. Physics Procedia, 2(3), 1223–1229. doi:10.1016/j.phpro.2009.11.085

[39] T. Matsui, T. Ogawa, Y. Adachi. (2019). Relationship between three-dimensional microstructure and Avrami exponent for recrystallization in pure iron. Results in Materials, 100002. doi:10.1016/j.rinma.2019.100002

[40] B. Opitek, et. al. (2021). Analysis of the Crystallization Kinetics and Thermal Stability of the Amorphous Mg72Zn24Ca4 Alloy. Materials, 14(13), 3583. doi:10.3390/ma14133583

[41] R. Ray, B. Hutchinson, C. Ghosh, (2011). “Back-annealing” of cold rolled steels through recovery and/or partial recrystallisation. International Materials Reviews, 56(2), 73–97. doi:10.1179/095066010X12646898728444

[42] S. Sahay, A. Kumar, A. Chatterjee. (2004). Development of integrated model for batch annealing of cold rolled steels. Ironmaking & Steelmaking, 31(2), 144–152. doi:10.1179/030192304225010990

[43] R. Wichienrak, R., S. Puajindanetr. (2019). Factors Affecting the Mechanical Properties Variation after Annealing Of Cold Rolled Steel Sheet. E3S Web of Conferences, 95, 04003. doi:10.1051/e3sconf/20199504003

[44] Internal communication with Stelco, 2023.

[45] T. Bergman, A. Lavine, Fundamentals of Heat and Mass Transfer, Wiley, 2017

[46] N. Saeidi, A. Ekrami. (2009). Comparison of mechanical properties of martensite/ferrite and bainite/ferrite dual phase 4340 steels. Materials Science and Engineering: A, 523(1-2), 125–129. doi:10.1016/j.msea.2009.06.057

[47] R. Davies. (1979). Influence of silicon and phosphorous on the mechanical properties of both ferrite and dual-phase steels. Metallurgical Transactions A, 10(1), 113–118. doi:10.1007/bf02686414

[48] P. Gong, X. Liu, A. Rijkenberg, W. Rainforth. (2018). The effect of molybdenum on interphase precipitation and microstructures in microalloyed steels containing titanium and vanadium. Acta Materialia. doi:10.1016/j.actamat.2018.09.008

[49] F. Perrard, A. Deschamps, A., P. Maugis. (2007). Modelling the precipitation of NbC on dislocations in α-Fe. Acta Materialia, 55(4), 1255–1266. doi:10.1016/j.actamat.2006.10.003

[50] D. Lehmhus, M. Busse, A. Herrmann, K. Kayvantash. Structural Materials and Processes in Transport, Wiley, 2013

[51] K. Kim, I. Moon, K. Kim, K. Kang, B. Park, K. Lee. (2017). Influence of Carbon Equivalent Value on the Weld Bead Bending Properties of High-Strength Low-Alloy Steel Plates. Journal of Materials Science & Technology, 33(4), 321–329. doi:10.1016/j.jmst.2016.07.009

[52] G. Paltanea, V. Manescu, R. Stefanoiu, I. Nemoianu, H. Gavrila. (2020). Correlation between Magnetic Properties and Chemical Composition of Non-Oriented Electrical Steels Cut through Different Technologies. Materials, 13(6), 1455. doi:10.3390/ma13061455

[53] P. Ghosh, R. Ray. (2017). Deep drawable steels. Automotive Steels, 113–143. doi:10.1016/b978-0-08-100638-2.00005-5

[54] ISO 10113:2020, Metallic materials – Sheet and Strip – Determination of Plastic Strain Ratio. (2020). https://www.iso.org/obp/ui/en/#iso:std:iso:10113:ed-3:v2:en

[55] F. Humphreys, M Hatherly. Recrystallization and Related Annealing Phenomena, Elsevier, 2004

[56] C. English, J. Hyde, G. Odette, G. Lucas, L. Tan. (2019). Research Tools: Microstructure, Mechanical Properties, and Computational Thermodynamics. Structural Alloys for Nuclear Energy Applications, 103–161. doi:10.1016/b978-0-12-397046-6.00004-6

[57] P. Lake, J. Greenwalt. (1977). Partially Annealed High Strength Cold Rolled Steels. SAE Transactions, 86(1), 718-729. https://www.jstor.org/stable/44644111

[58] P. Winter, R. Woodward. (1986). Effect of tempering temperature on the work-hardening rate of five HSLA steels. Metallurgical Transactions A, 17(2), 307–313. doi:10.1007/bf02643906

[59] N. Tsuchida. (2001). Application of the Kocks–Mecking model to tensile deformation of an austenitic 25Cr–19Ni steel. Acta Materialia, 49(15), 3029–3038. doi:10.1016/s1359-6454(01)00197-5

[60] D. Bailey, W. Flanagan. (1967). The relationship between dislocation density and flow stress in materials deforming by a peierls-nabarro mechanism. Philosophical Magazine, 15(133), 43–49. doi:10.1080/14786436708230350

[61] J. Takahashi, K. Kawakami, J. Hamada, K. Kimura. (2016). Direct observation of niobium segregation to dislocations in steel. Acta Materialia, 107, 415–422. doi:10.1016/j.actamat.2016.01.070

[62] Internal data from Stelco, 2023

[63] Communication with Professor J. David Embury, 2023

[64] M. Militzer, J. Hoyt, N. Provatas, J. Rottler, C. Sinclair, H. Zurob. (2014). Multiscale Modeling of Phase Transformations in Steels. JOM, 66(5), 740–746. doi:10.1007/s11837-014-0919-x

APPENDIX

Appendix A – V10 High-Magnification TEM Images

These figures are additional TEM images taken of the V10 steel at 240kx magnification.

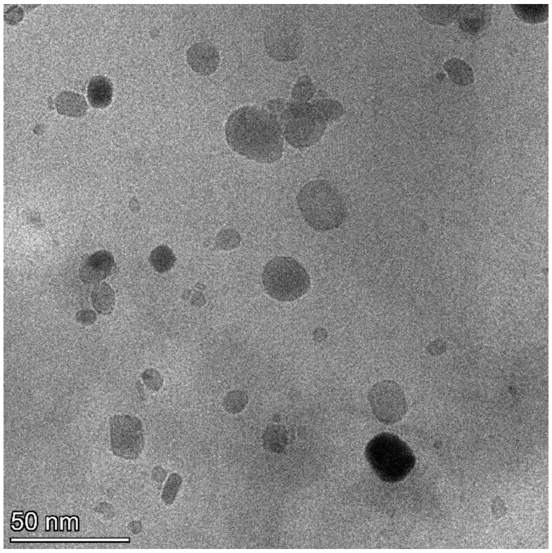

Figure A1: V10 Steel, 650°C at 240kx in TEM

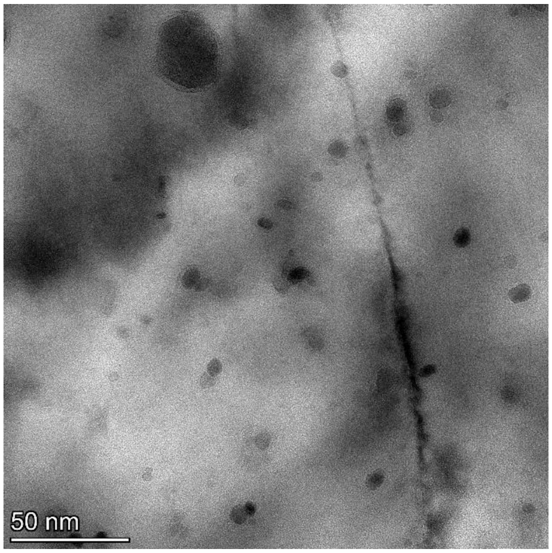

Figure A2: V10 Steel, 650°C at 240kx in TEM

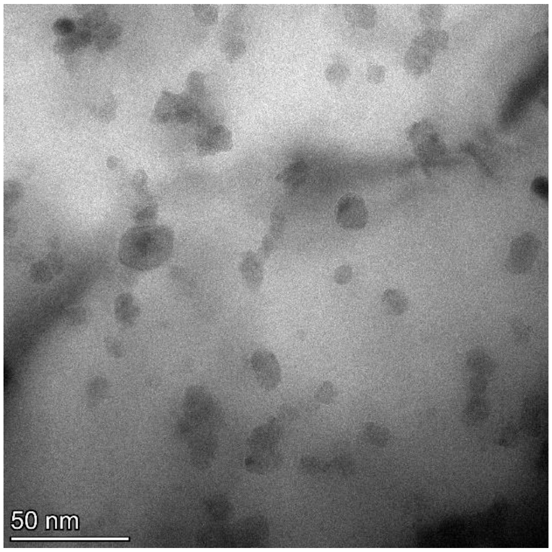

Figure A3: V10 Steel, 700°C at 240kx in TEM

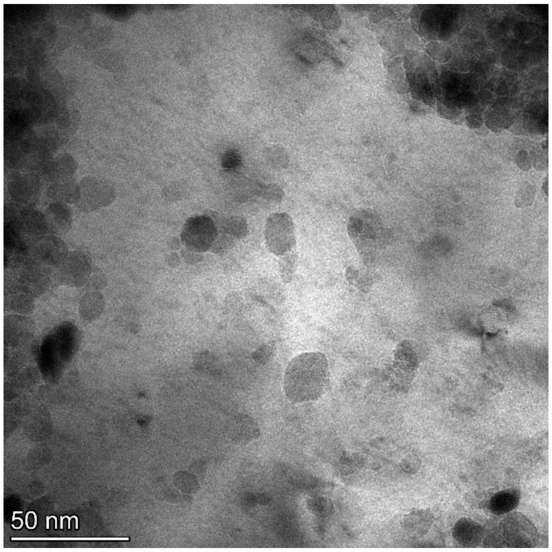

Figure A4: V10 Steel, 700°C at 240kx in TEM

Appendix B – V10 TEM EDS Maps

These are additional TEM EDS maps of a precipitate in the V10 steel. All these images were taken at 380kx magnification.

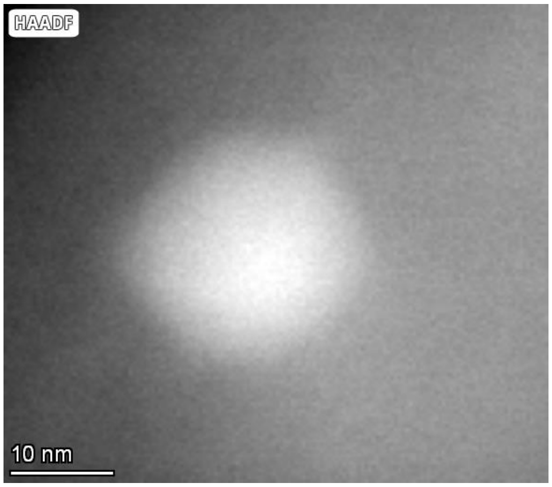

Figure A5: V10 EDS Base Map, 380kx Magnification

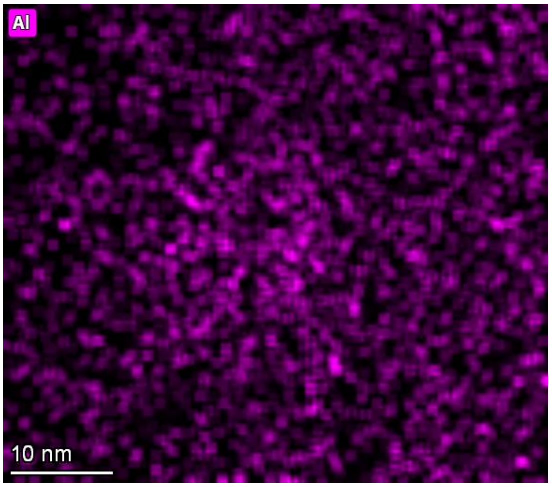

Figure A6: V10 EDS Al Map

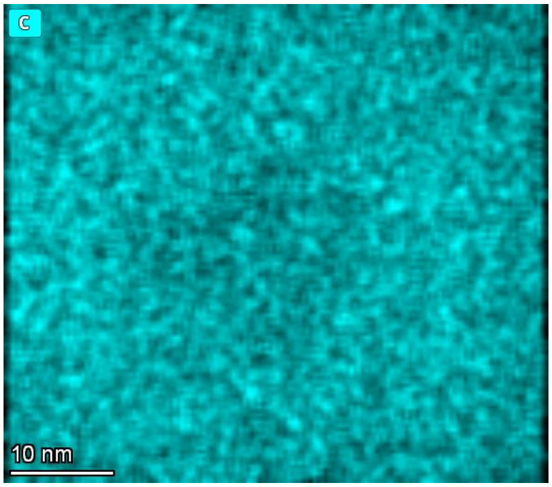

Figure A7: V10 EDS C Map

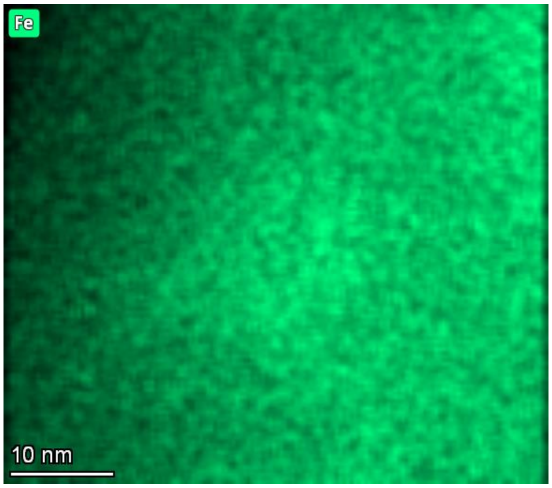

Figure A8: V10 EDS Fe Map

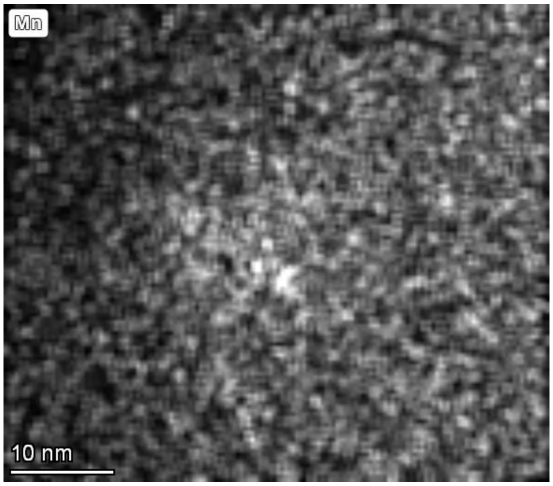

Figure A9: V10 EDS Mn Map

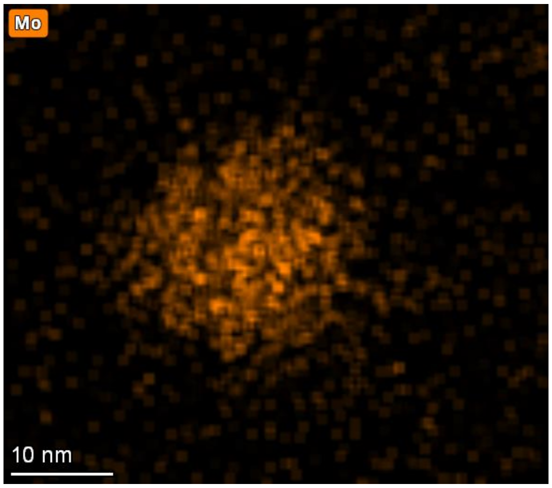

Figure A10: V10 EDS Mo Map

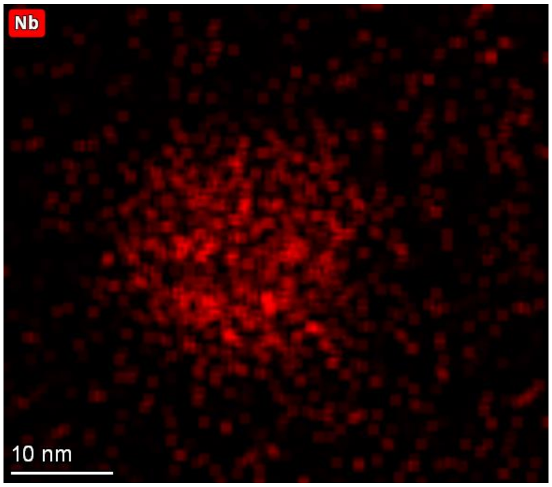

Figure A11: V10 EDS Nb Map

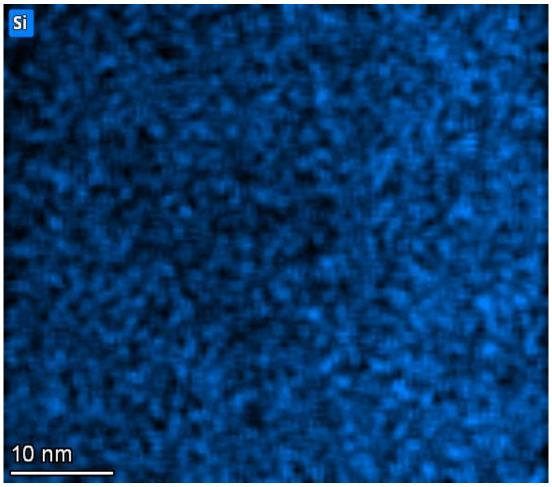

Figure A12: V10 EDS Si Map

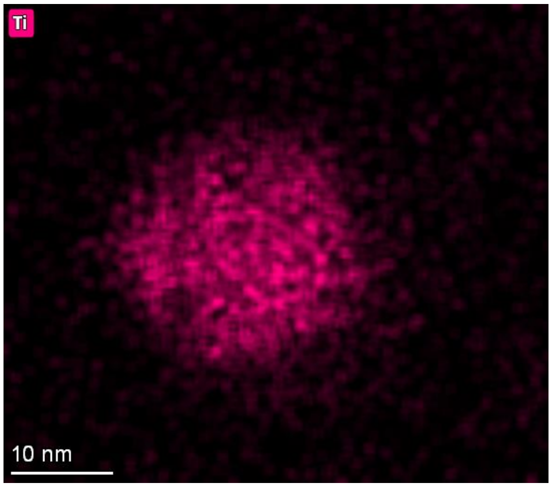

Figure A13: V10 EDS Ti Map

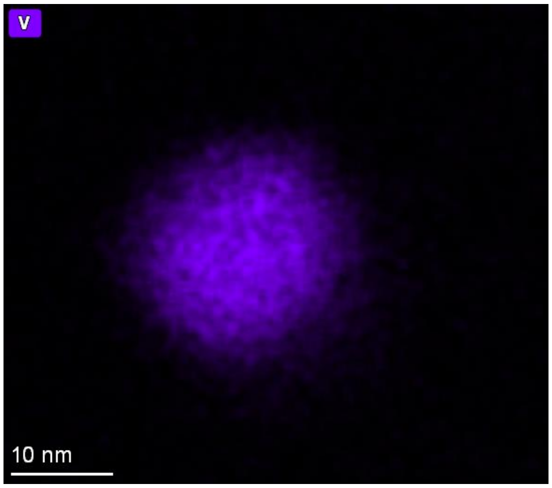

Figure A14: V10 EDS V Map

Appendix C – Fe_2SiTi Experiment

Figure A15 shows the hardness tests for various heat treatments for a steel with 1.0%Si and 0.2%Ti. According to Thermo-Calc, a phase of Fe2SiTi should form at temperatures around 400°C. However, as can be seen by the triangles (cold rolled then annealed), regardless of the length of heat treatment at 400°C, the hardness remained the same, so the precipitates do not form under reasonable timescales.

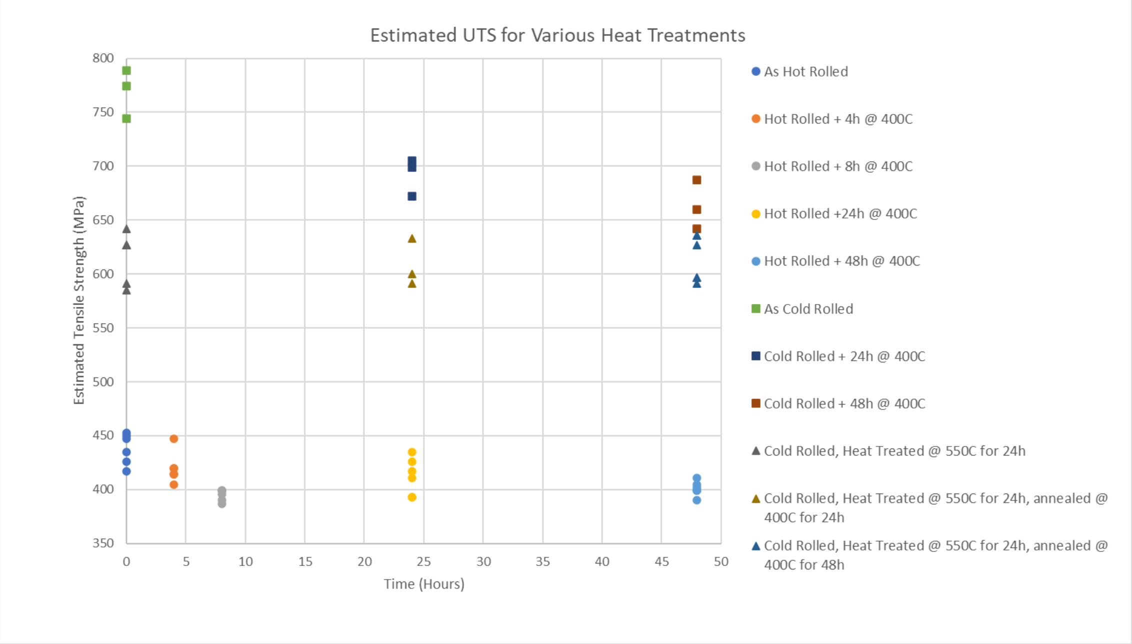

Figure A15: Estimated UTS of Various Heat Treatments of a Steel High in Si and Ti

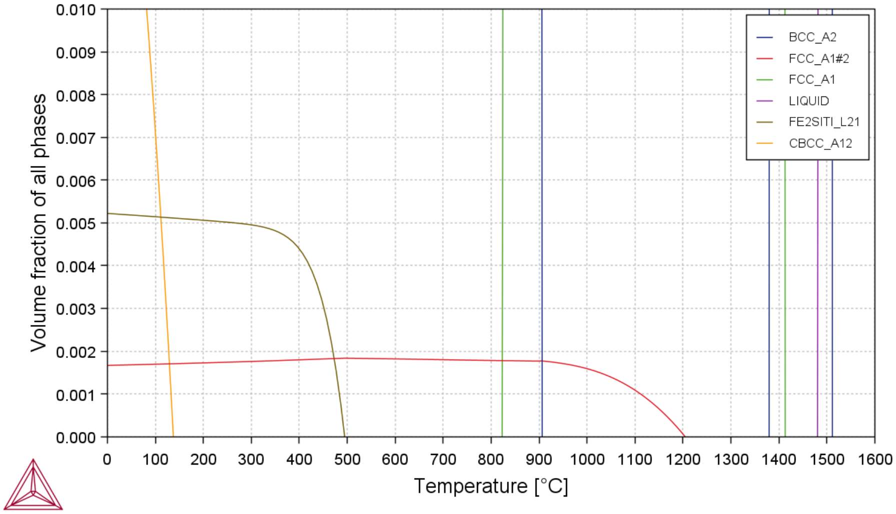

Figure A16: Thermo-Calc Simulation for the High Si+Ti Steel

Appendix D – V20 5000x Magnification SEM Images

SEM was performed on the V20 steel. The images at 2000x magnification were shown in the body of the thesis, these are the images taken at 5000x magnification.

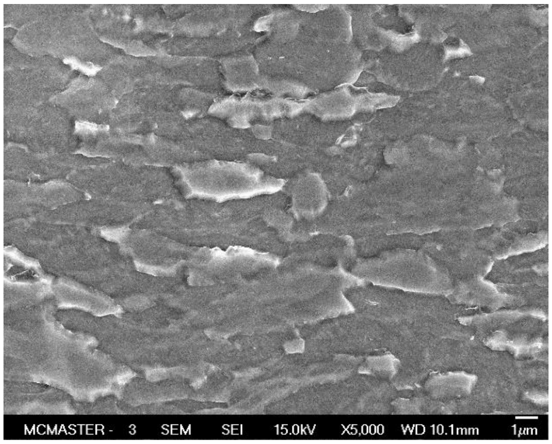

Figure A17: 0.2%Ti Steel Annealed at 550°C at 5000x in SEM

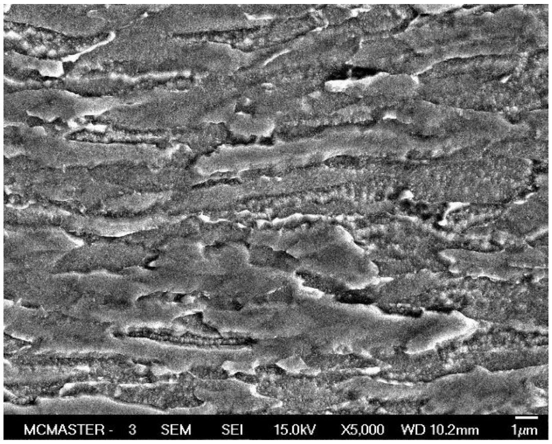

Figure A18: 0.4%Ti Steel Annealed at 550°C at 5000x in SEM

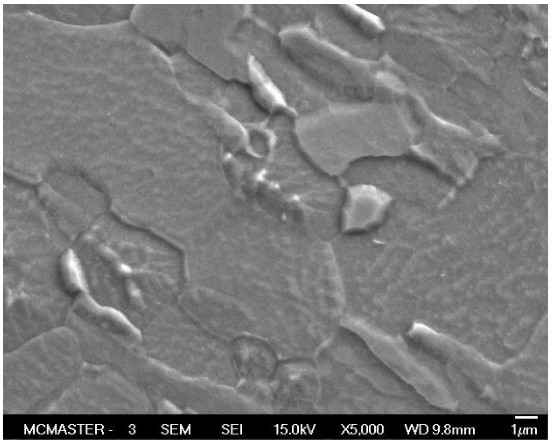

Figure A19: 0.2%Ti Steel Annealed at 575°C at 5000x in SEM

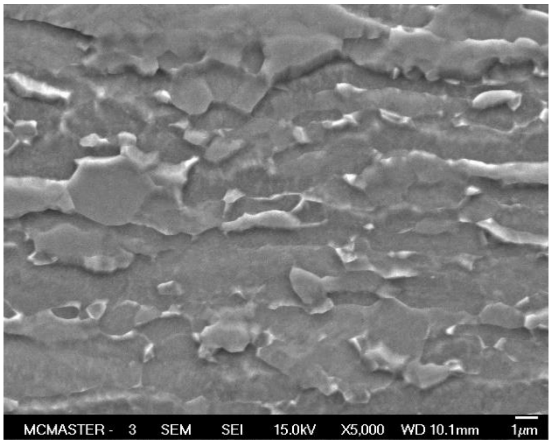

Figure A20: 0.4%Ti Steel Annealed at 575°C at 5000x in SEM

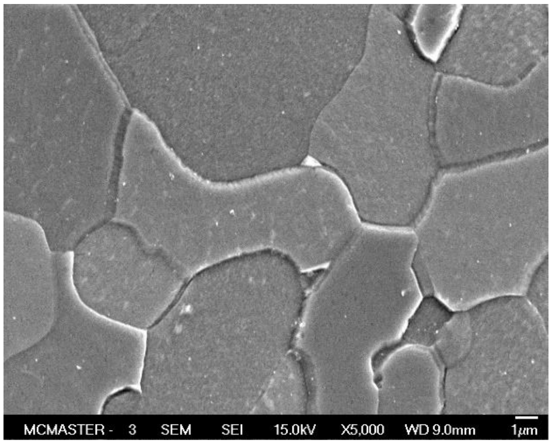

Figure A21: 0.2%Ti Steel Annealed at 600°C at 5000x in SEM

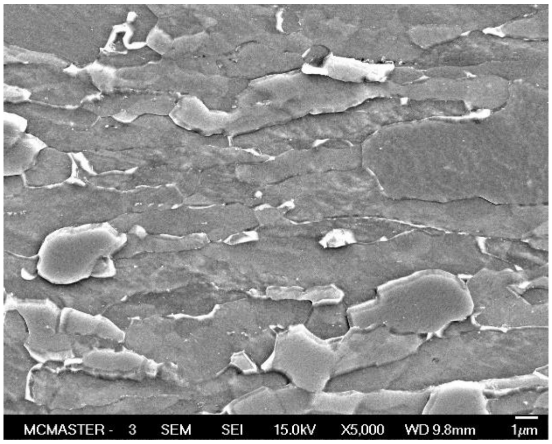

Figure A22: 0.4%Ti Steel Annealed at 600°C at 5000x in SEM

Appendix E – V20 TEM Bright Field Images

In bright field (BF) images, the dislocations appear as dark lines and the precipitates appear as dark spots.

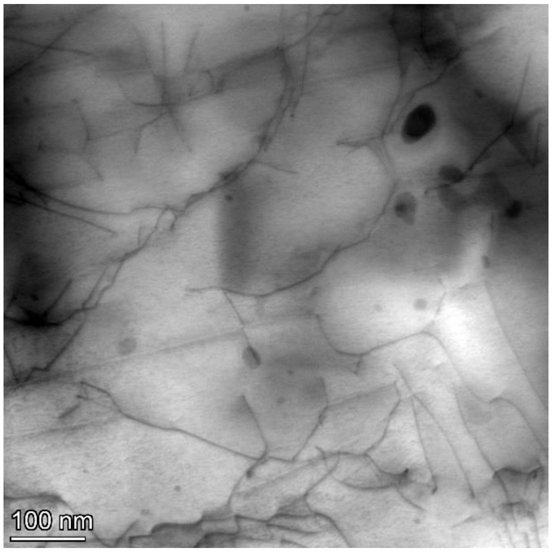

Figure A23: 0.2%Ti Steel Annealed at 550°C at 135kx in BF STEM

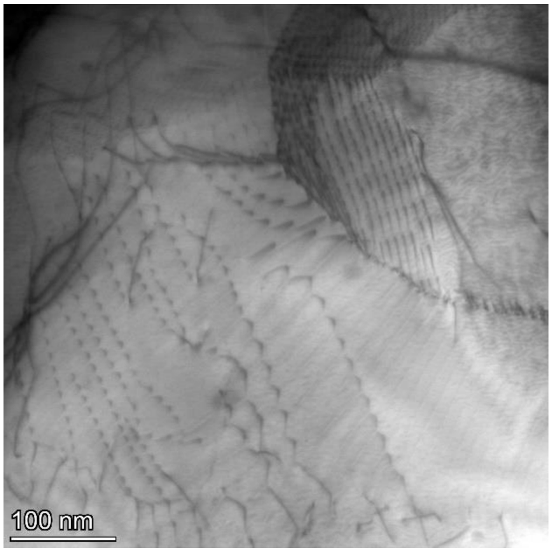

Figure A24: 0.2%Ti Steel Annealed at 550°C at 190kx in BF STEM

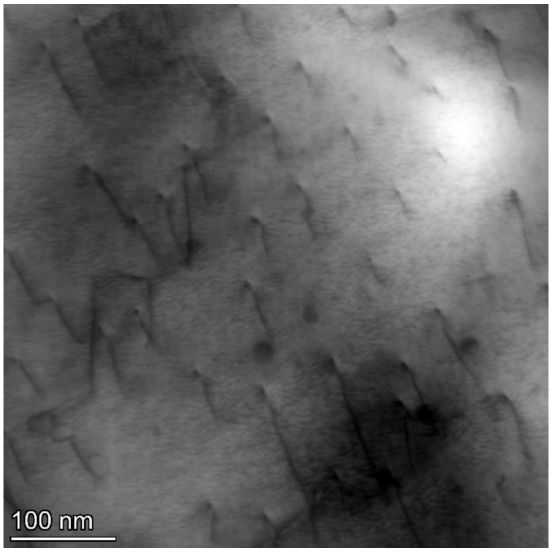

Figure A25: 0.2%Ti Steel Annealed at 550°C at 190kx in BF STEM Image 2

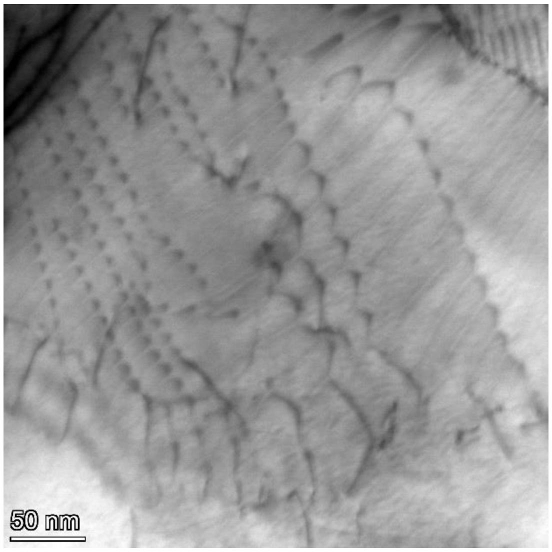

Figure A26: 0.2%Ti Steel Annealed at 550°C at 270kx in BF STEM

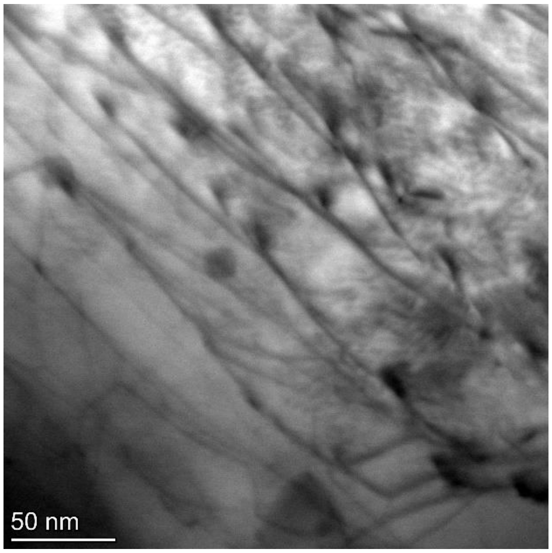

Figure A27: 0.2%Ti Steel Annealed at 550°C at 380kx in BF STEM

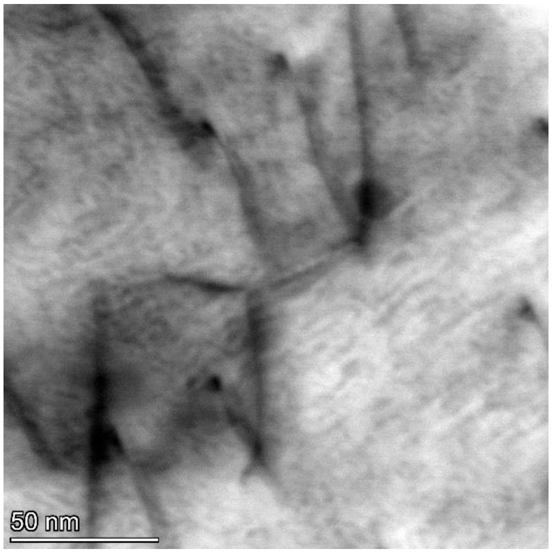

Figure A28: 0.2%Ti Steel Annealed at 550°C at 540kx in BF STEM

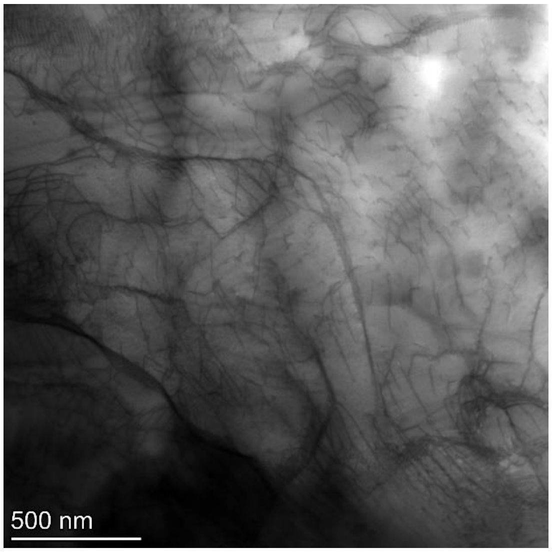

Figure A29: 0.2%Ti Steel Annealed at 550°C at 48000x in BF STEM

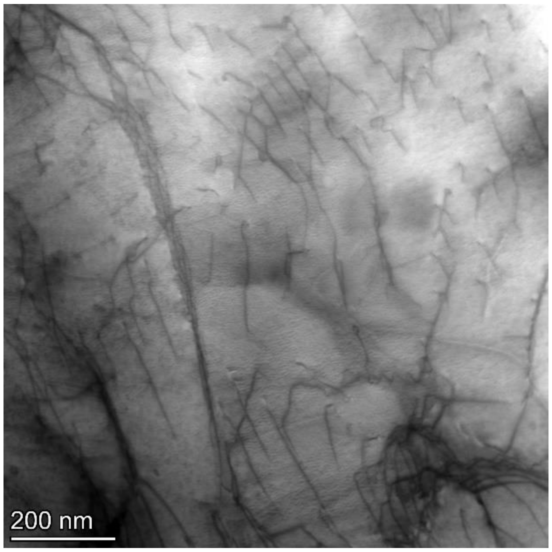

Figure A30: 0.2%Ti Steel Annealed at 550°C at 95000x in BF STEM

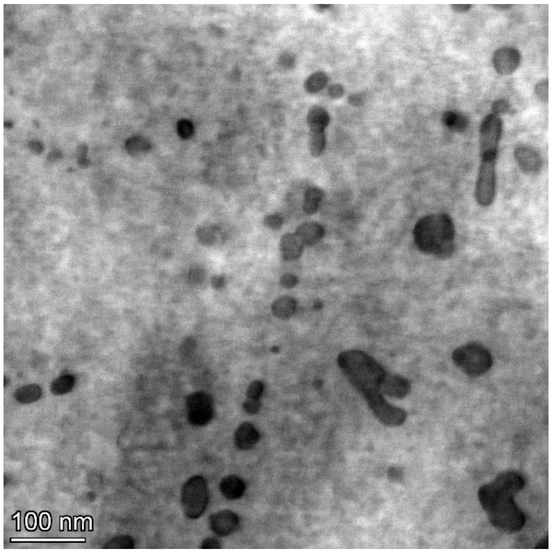

Figure A31: 0.2%Ti Steel Annealed at 600°C at 135kx in BF STEM

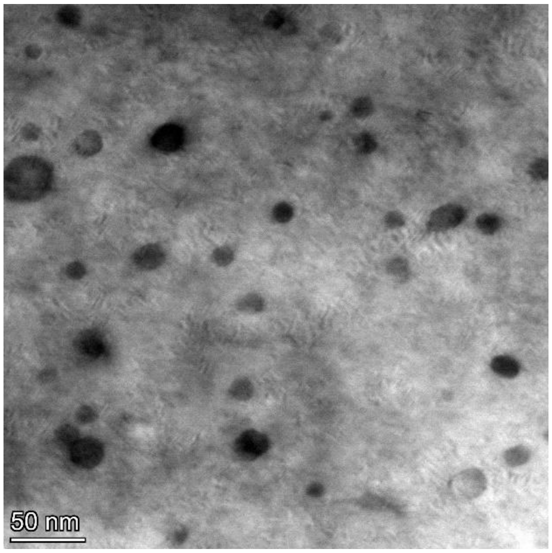

Figure A32: 0.2%Ti Steel Annealed at 600°C at 270kx in BF STEM

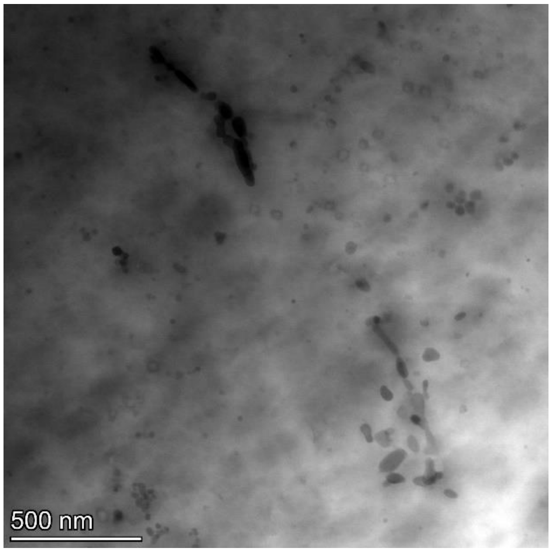

Figure A33: 0.2%Ti Steel Annealed at 600°C at 48000x in BF STEM

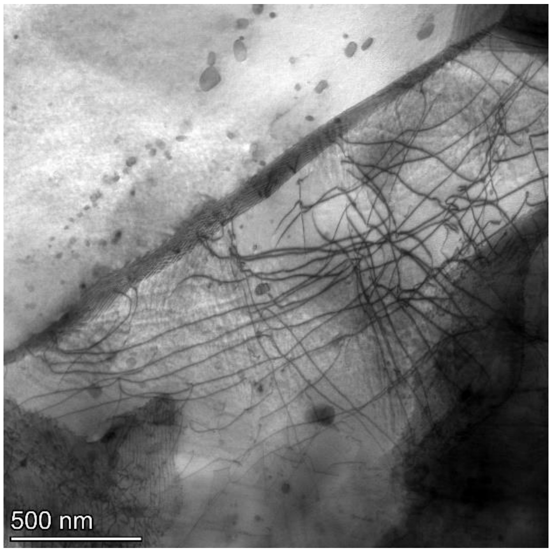

Figure A34: 0.2%Ti Steel Annealed at 600°C at 48000x in BF STEM With Dislocations

Appendix F – V20 EDS Additional Precipitate Maps

These maps show that the metallic portion of the precipitates in the V20 are made exclusively of titanium, as was expected based on the steel's composition.

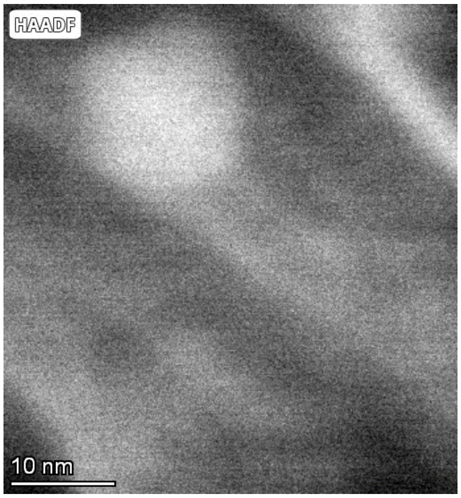

Figure A35: 0.2%Ti Steel Annealed at 550°C at 540kx, Ti EDS Base Map (Same as Figure 3.2.2.3.S)

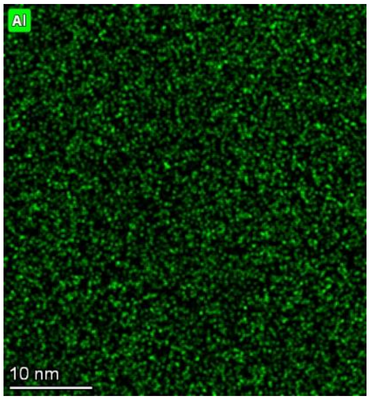

Figure A36: 0.2%Ti Steel Annealed at 550°C at 540kx, Al EDS Map

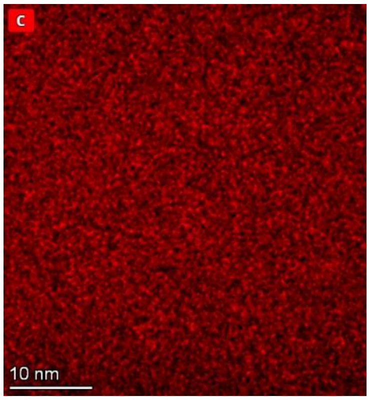

Figure A37: 0.2%Ti Steel Annealed at 550°C at 540kx, C EDS Map

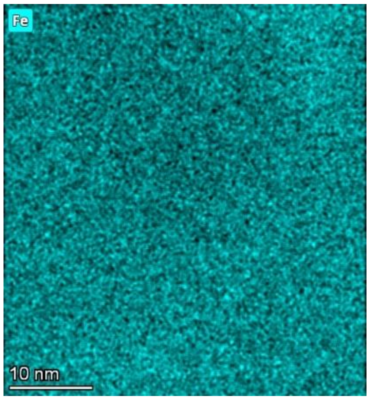

Figure A38: 0.2%Ti Steel Annealed at 550°C at 540kx, Fe EDS Map

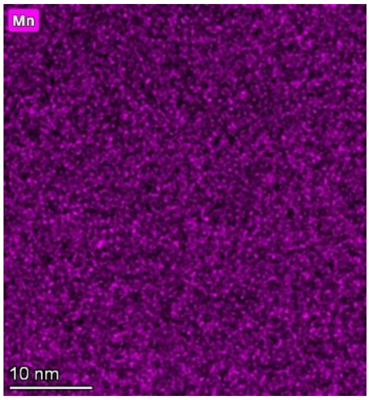

Figure A39: 0.2%Ti Steel Annealed at 550°C at 540kx, Mn EDS Map

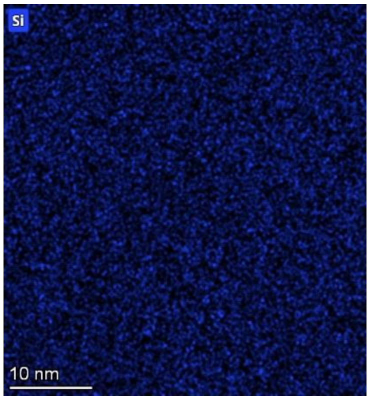

Figure A40: 0.2%Ti Steel Annealed at 550°C at 540kx, Si EDS Map

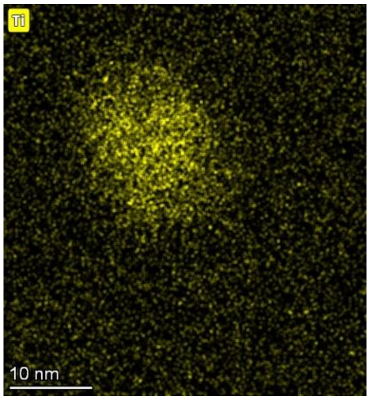

Figure A41: 0.2%Ti Steel Annealed at 550°C at 540kx, Ti EDS Map

Appendix G – V20 Additional APT Images

These images are from the second APT tip with the grain boundary, whose presence can be seen in Figure 42A.

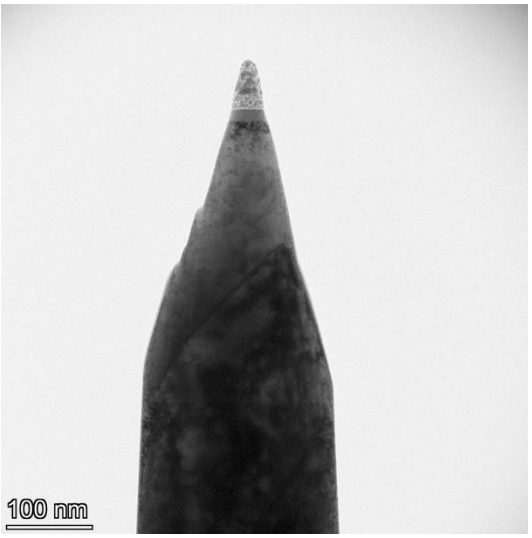

Figure A42: Second APT Tip in TEM

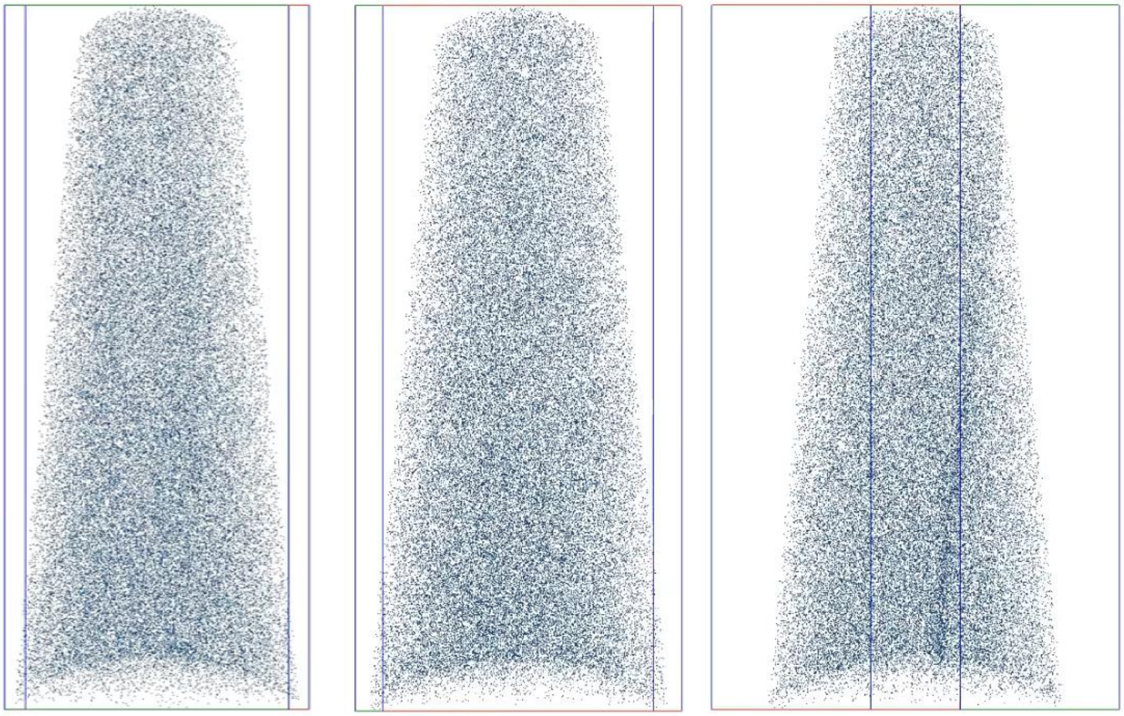

Figure A43: Second APT Tip Ti Map at
a) 0° of Rotation
b) 90° of Rotation
c) 130° of Rotation